Title

Finite element and integral equation formulations for high -performance micromagnetic and electromagnetic solvers

Author

Chang, Ruinan

Publication Date

2014

UNIVERSITY OF CALIFORNIA, SAN DIEGO

Finite element and integral equation formulations for high-performance micromagnetic and electromagnetic solvers

A dissertation submitted in partial satisfaction of the
requirements for the degree
Doctor of Philosophy

in

Electrical Engineering (Electronic Circuits & Systems)

by

Ruinan Chang

Committee in charge:

Professor Vitaliy Lomakin, Chair
Professor Raymond A. de Callafon
Professor Yeshaiahu Fainman
Professor Eric E. Fullerton
Professor Bo Li
Professor Kevin B. Quest

2014

The dissertation of Ruinan Chang is approved, and it is acceptable in quality and form for publication on microfilm and electronically:

Chair

University of California, San Diego

2014

DEDICATION

To my family.

TABLE OF CONTENTS

LIST OF FIGURES

LIST OF TABLES

ACKNOWLEDGEMENTS

This dissertation could not have been possible without the countless guidance and support from my adviser Professor Vitaliy Lomakin. Over the past five years, I have been fortunate enough to study under his guidance. Ever since the first day I landed in U.S., he has given me continued selfless help, support and encouragement. Though him, I have learned and mastered many advanced techniques in finite elements and integral equations, the physics of magnetic recording and applied electromagnetics. More importantly, I have got from him how to face difficult problem with fortitude, dexterity, and persistence. His kindness to students, his keen interests in science and engineering, his broad spectrum of knowledge have impressed me so much. He is not only an academic adviser, but also a mentor and friend of life. The years spent in the Computational Electromagnetics and Micromagnetics (CEMM) group led by Professor Vitaliy Lomakin will always be the most invaluable and happiest memories in my life, which I will always cherish as the most precious treasure.

I am very grateful to Professor Eric Fullerton. His influences on me are many-sided. As an instructor of magnetics, his lectures were very attractive, and my interest and knowledge in magnetics mushroomed noticeably as a result of his classes. Serving on the committee of preliminary and qualifying examinations, he gave incisive suggestions which would later greatly shaped my understanding of magnetic physics.

Professor Kevin Quest is another scholar who has greatly helped me over the course of my study and research. His classes were concise but contained the most important ingredients of applied electromagnetics. His discussion of nonlinear magnetics ignited my initial interest in the broad area of micromagnetics.

Professor Fainman and Raymond de Callafon and Bo Li have considerably helped me over my examinations. They have also put forwards many critical advices for the dissertation.

I am deeply indebted to Dr. Shaojing Li, for many fruitful collaborations on a number of projects. From him, I have learned not only much knowledge of fast algorithms such as Fast Fourier Transforms (FFTs) but also the altitude towards making excellent research. I am grateful to Ms. Qian Ding. We have discussed lots of problems on antennas, waveguides, filters and so forth. She also taught me how to use some software tools.

Moreover, I would also thank Dr. Derek Van Orden and Dr. Marko Lubarda for their numerous help and discussions. Their extensive knowledge in electromagnetic and micromagnetic physics greatly illuminated me. I enjoy lots of our active and expansive discussions on numeric computations, physics, and I miss the days when they were in CEMM group and we played pingpong together everyday.

I am also grateful to Marco Escobar and Sidi Fu. Mr. Escobar's work significantly increased my understanding ordinary differential equation solvers. Mr. Fu's work greatly improved the speed of many of my numerical programs by providing Graphic Processing Units (GPUs) accelerated fast algorithms.

Dr. Boris Livshitz is another person to whom I owe a lot. Although the overlapped time with him is not long, still I learned many useful techniques from him. I have also been lucky to receive lots of encouragement and advice from him. I would like to thank Marco Menarini, Simon Conture and Majd Koutifan for our fruitful discussions.

Meanwhile, I am deeply grateful to my family, especially my grandma, who is already in her 80s. Although they cannot help me academically, their encouragement and support are an indispensable part of life.

Chapter 2, in part, is based on four journal articles: (1) R. Chang, S. Li, M. V. Lubarda, B. Livshitz, V. Lomakin, "FastMag: Fast micromagnetic solver for large-scale simulations," Journal of Applied Physics 109, 07D358 (2011). (2) M. V. Lubarda, S. Li, R. Chang, M. A. Escobar, E. E. Fullerton, V. Lomakin, "Domain wall motion in magnetically frustrated nanorings," Physical Review B. vol. 85, 214428, 2012. (3) R. Chang, S. Li, M. A. Escobar, M. V. Lubarda, and V. Lomakin, "Accurate evaluation of exchange fields in finite element micromagnetic solvers," Journal Appl. Phys., vol. 111, p.07D129, 2012. (4) M. A. Escobar, M. V. Lubarda, S. Li, R. Chang, B. Livshitz, and V. Lomakin, "Micromagnetic analysis of write head dynamics using FastMag," IEEE Trans. Magn., vol. 48, no. 5, May 2012.

Chapter 5, in part, is based on the journal article: R. Chang, V. Lomakin, “Quadrilateral Barycentric Basis Functions for Surface Integral Equations,” IEEE Trans. Antennas Propag., vol. 61, no. 12, Dec. 2013.

Chapter 6, in part, is based on the journal article: S. Li, R. Chang, A. Boag, V. Lomakin, “Fast electromagnetic integral equation solvers on graphics processing units,” IEEE Antennas Propag. Mag., vol. 54, no. 5, Oct.2012.

LIST OF ABBREVATIONS

ABC	Absorbing Boundary Condition
BF	Basis Function
CPU	Central Processing Unit
DBF	Dual Basis Function
EFIE	Electric Field Integral Equation
FDM	Fintie Difference Method
FDTD	Finite Difference Time Domain
FEM	Finite Element Method
FFT	Fast Fourier Transform
GPU	Graphical Processing Unit
GLBF	Global Loop Basis Function
JVP	Jacobian Vector Product
IE	Integral Equation
LLBF	Local Loop Basis Function
MFIE	Magnetic Field Integral Equation
ODE	Ordinary Differential Equation
PDE	Partial Differential Equation
RWG	Rao Wilton Glisson
QBF	Quadrilateral Basis Function
s-BF	scalar Basis Function
SBF	Star Basis Function
v-BF	vector Basis Function
LLGE	Landau Lifshitz Gilbert Equation
SIE	Surface Integral Equation

VITA

2007	B. S. in Electronic Engineering, Tsinghua University
2009	M. S. in Microelectronics, Tsinghua University
2014	Ph. D. in Electrical Engineering, University of California, San Diego

PUBLICATIONS

R. Chang, V. Lomakin, “Quadrilateral Barycentric Basis Functions for Surface Integral Equations,” *IEEE Trans. Antennas Propag.*, vol. 61, no. 12, Dec. 2013.

M. V. Lubarda, S. Li, R. Chang, M. A. Escobar, E. E. Fullerton, V. Lomakin, “Domain wall motion in magnetically frustrated nanorings,” *Physical Review B.* vol. 85, 214428, 2012.

R. Chang, S. Li, M. V. Lubarda, B. Livshitz, and V. Lomakin,“FastMag: Fast micromagnetic simulator for complex magnetic structures,” *Journal Appl. Phys.*, vol. 109, p.07D358, 2011.

R. Chang, S. Li, M. A. Escobar, M. V. Lubarda, and V. Lomakin,“Accurate evaluation of exchange fields in finite element micromagnetic solvers,” *Journal Appl. Phys.*, vol. 111, p.07D129, 2012.

S. Li, R. Chang, A. Boag, V. Lomakin,“Fast electromagnetic integral equation solvers on graphics processing units,” *IEEE Antennas Propag. Mag.*, vol. 54, no. 5, Oct.2012.

M. A. Escobar, M. V. Lubarda, S. Li, R. Chang, B. Livshitz, and V. Lomakin, “Micromagnetic analysis of write head dynamics using FastMag,” *IEEE Trans. Magn.*, vol. 48, no. 5, May 2012.

ABSTRACT OF THE DISSERTATION

Finite element and integral equation formulations for high-performance micromagnetic and electromagnetic solvers

by

Ruinan Chang

Doctor of Philosophy in Electrical Engineering (Electronic Circuits & Systems)

University of California, San Diego, 2014

Professor Vitaliy Lomakin, Chair

The ability to have a good understanding of and to manipulate electromagnetic fields has been increasingly important for many hardware technologies. There is a strong need for advanced numeric algorithms that yield fast and accuracy-controllable solvers for electromagnetic and micromagnetic simulations.

The first part of the dissertation presents methods constituting the core of the high-performance simulator FastMag. FastMag derives its high speed from three aspects. First, it leverages the state-of-the-art graphics processing unit computational architectures, which can be hundreds of times faster than a single central processing unit. Moreover, efficient and and accurate implementations of numeric quadrature was invoked. Thirdly, we provide an analytic method for Jacobian-

vector products. Some advanced features are provided in FastMag. Quadratic basis functions are used to provide better accuracy. Hexahedral elements were also implemented because they are more accurate, consume less memory.

The second part of the dissertation is devoted to electromagnetic scattering problems. We developed new algorithms that significantly improved the traditional methods. First of all, potential volume integral equations were implemented, where the potential quantities (vector and scalar potential). Another important contribution of this disertation is quadrilateral barycentric basis functions (QBBFs). The QBBFs can serve as a fundamental block for primary basis functions (PBFs) and dual basis functions (DBFs). The PBFs and DBFs, when applied in combination into traditional electric and magnetic field integral equations (EFIE and MFIE), give rise to accurate and robust results. Moreover, the DBFs make the famous Calderón preconditioner multiplicative.

Chapter 1

Introduction

In this chapter, we review the background of the research, the state-of-the-art of the areas of micromagnetic and electromagnetic modeling.

1.1 Computational micromagnetics and electromagnetics

Many of the physical phenomena are governed by fundamental laws in the form of ordinary differential equations (ODEs) or partial differential equations (PDEs) [1, 2, 3]. In particular, the areas of micromagnetism and electromagnetism are fully characterized by PDEs. In Micromagnetics, the main equations are modifications of the Landau-Lifshitz-Gilbert equation (LLGE), which describe non-linear magnetization dynamics in magnetic materials [1]. In Electromagnetics, the phenomena of radiation, propagation, and scattering are described by various modifications of Maxwell's equations [2]. A plethora of modern technologies such as telecommunications, data storages, microelectromechanical systems, are built upon our understanding and applications of these equations.

Solutions of the equations are of great importance to the development of modern technologies. However, solving the ODEs and PDEs to analyze highly complex physical and engineering systems often is an involved process. Traditionally, mathematicians and physicists sought closed form analytic solutions to ODEs and PDEs, which, however, are limited to simple initial and boundary conditions and geometric structures. In the engineering world such as magnetic recording systems, microwave and optical circuits [4, 5, 6, 7], the geometries can be so complex that pure analytic methods can barely be successfully used. Therefore, a more general method that yields controllably accurate solutions is ubiquitously needed.

To overcome the restrictions of the analytic methods, many numerical methods have been invented and are run on digital computers. The computer-aided solutions are applicable to a wide range of configurations.

1.2 Numerical methods for micromagnetics and electromagnetics

This section reviews three of the most widely used frameworks for computational micromagnetics and electromagnetics. The advantages and limitations of each method are discussed.

1.2.1 Finite difference time domain method

The idea of using finite differences (FDs) to approximate derivatives has a long history. The finite difference time domain (FDTD) was for solving Maxwell's equations was proposed in 1966 [8, 9, 10]. It utilizes a regular grid of rectangular cuboids where the differential operators are numerically approximated by centeral differences. The fields are updated at every discrete time step. The size of a spatial cell (brick) is $\Delta x \times \Delta y \times \Delta z$. The time step size is Δt is dictated by the spatial discretization, through the Courant-Friedrichs-Lewy stability criterion [11]:

$$\sqrt{\frac{1}{\Delta x^2}+\frac{1}{\Delta y^2}+\frac{1}{\Delta z^2}} \leq \frac{1}{c\Delta t}, \tag{1.1}$$

where c is the speed of light. FDTD is matrix-free, therefore it does not require complex data structures or algorithms [12]. FDTD is easy to implement and parallelize. As a widely used time domain method, the FDTD yields an animation like simulation result and can be applied to nonlinear problems [13]. FDTD has great successes in simulating antennas, microwave circuits, light scattering from many plasmonic objects, periodic structures with multiple incident angles [14, 15, 16]. Moreover, the FDTD-like methods has also been investigated extensively in micromagnetics, fluid dynamics and other fields of study.

While having achieved a significant success [17], the applications of FDTD are hindered by a few factors. First, it is difficult to model complexly shaped structures with many fine geometrical features, because the regular cubic grids are intrinsically inefficient to approximate curved structures. Second, it needs absorbing boundary conditions (ABCs) [18] or perfect matched layers (PMLs) [19] to truncate the computational domains since the electromagnetic field permeates the whole space. The ABCs or PMLs are artificial and they may compromise accuracy and increase complexity. Third, it is difficult to handle low frequency problems efficiently using FDTD. It is observed from Eq. (1.1) that FDTD would require that Δt be proportional to Δx, resulting in very small step size (compared to a period) and a very large number of steps. Although the advantages of FDTD are pronounced, its limitations make it not efficient for a set of problems [20].

1.2.2 Brief review of finite element methods

FEM is a general framework for solving PDEs over arbitrarily-shaped domains [21]. Both FDTD and FEM are based on differential equations, but FEMs are more suited for arbitrarily shaped objects. The flexibility of FEM roots in its ability to use many types of geometric "elements" to approximate a geometric structure. In comparison, the FDTD employs only bricks. Therefore, FEM is a super set of FDTD.

The basic idea of FEM emerged in 1940s [22] while the realistic applications became possible after the advent of digital computers in 1950s [23, 24]. Various FEM formulations for many areas of computational physics have been developed and successfully used. For example, researchers proposed hexahedrons, prims, pyramids and even curved elements other than simple elements such as triangles and tetrahedrons. Moreover, scalar basis functions (s-BFs) were extended from lower order to higher order to achieve high accuracy by multiplying some polynomials to increase the smoothness [25, 26, 27]. Each s-BF is tied to a node, so the s-BF is sometimes termed node element. Many physical quantities are vectors in nature, s-BFs are insufficient and result in very large errors [21]. A major innovation, unveiled in 1980s, was the vector basis functions (v-BFs) proposed by Nédélec [28]. The v-BF is assigned to an edge, therefore, it is often referred to as edge element. The 1990s witnessed a wide range applications of v-BFs in various problems including electromagnetics. Since then the v-BFs have become the mainstream in the FEM community [29, 30].

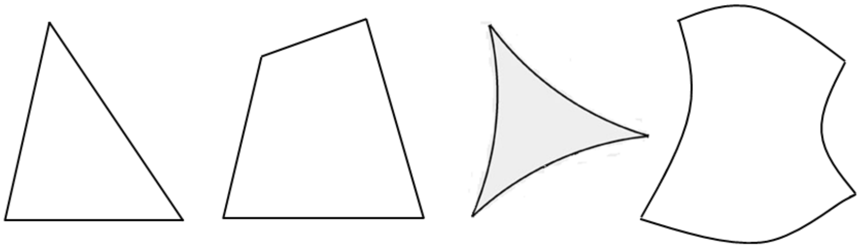

Figure 1.1: Common elements for two dimensional meshes. From left to right, they are triangle, quadrilateral, curvilinear triangle and quadrilateral.

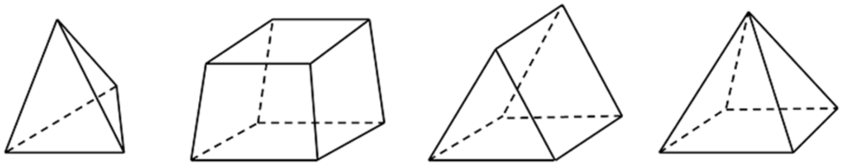

Figure 1.2: Common elements for three dimensional meshes. From left to right, they are tetrahedron, hexahedron, prism and pyramid.

The curvilinear elements are capable of high fidelity geometric modeling of general structures [31, 32]. Such elements are more difficult to implement. The implementations in this disertation are based on straight 2D or 3D element shapes, but the general ideas can be extended to curvilinear elements without major modifications.

Different than the FDTD, FEM requires matrix inversion operations for most problems [21, 33]. The matrices in FEM are sparse and often ill-conditioned.

How to accelerate the speed of matrix inversions has been the major topic of FEM. The FEM has also been used to micromagnetics since 1990s. While the FEM has achieved a noticeable success in solving Maxwell and Landau-Lifshitz-Gilbet (LLG) equations, there are still a number of limitations. For example, in micromagnetics traditionally the demagnetization field was obtained by solving the Poisson equation with artificial boundary conditions (ABCs). The ABCs introduce extra errors in the magnetic potentials. Moreover, this method requires a robust preconditioner, which may be memory and computational time costly.

1.2.3 History of integral equation methods for electromagnetic simulations

Integral equations(IEs) are an alternative approach to solving various computational physics problems [34, 35]. Typically, a linear PDE with proper boundary conditions gives rise to a Green's function, which represents an impulse response of the physical system, e.g. it is the field radiated by a point current in electromagnetic systems. It is the kernel of an integral equation that is mathematically equivalent to the original PDE. The Green's functions can take into account the boundary conditions of the equations. For instance, an array of antennas or photonic structures can be modeled by periodic Green's functions [36]. Moreover, an object immersed in a layered media can be analyzed by the layered Green's function [37, 38]. The mathematical equivalence between the integral- and differential equations, however, does not translate into a computational equivalence. Numerical solution of IEs relies on a mesh similar to that in FEM. Similar to FEM, IEs also require a structure be discretized into simple geometric elements such as triangles, quadrilaterals, tetrahedrons, hexahedrons. The unknown quantities such as electric and magnetic currents are expanded as a summation of known v-BFs weighted by some coefficients. In the solution process, there are many types of integrals, very few of which can be computed analytically, so numeric quadratures are used.

The IEs have attracted a long interest among the mathematics, physics and engineering communities for their unique features. The mathematical foundations of integral equations for microwave engineering were established in the beginning of 1940s. The earliest numerical solutions on computers seems to appear in 1960s. Different from the FEM, IEs give rise to a full matrix in discretization. It would cost $\mathcal{O}(N^2)$ memory space in the traditional method (Here N is the size of the matrix) [39], which is very high for large scale computational systems. The large scale applications were not possible until 1980s when the first "fast" algorithm "Fast Multipole Method" was invented [40]. Later many other fast algorighms have been proposed such as precorrected Fast Fourier Transform (pFFT), non-uniform grid interpolation method (NGIM), and hierarchical matrices [41, 42, 43]. The fast algorithms do not explicitly generate the matrix, rather, they can calculate the matrix vector products in $\mathcal{O}(N \ln N)$ or even $\mathcal{O}(N)$ time.

In the context of electromagnetics [44], IE methods have been a particular attraction because of three reasons. (1) IEs directly utilize the Green's functions which describe the propagation properties of waves, and do not need ABCs, they can avoid dispersion error and have better accuracy over differential equation-based methods. (2) The IEs yield a smaller number of unknowns because the ambient free space does not need to be discretized, and only the "source" regions are meshed. (3) The condition number of the matrices from IEs can be smaller than that from FEMs, and give rise to a faster convergence and hence a smaller complexity.

1.3 Linear equations in numerical methods

One of the major challenges for both FEM and IEs is how to solve a linear equation of the form:

$$\mathbb{A}\boldsymbol{x} = \boldsymbol{b}, \tag{1.2}$$

where $\mathbb{A}$ is an $N \times N$ matrix, $\boldsymbol{x}$ and $\boldsymbol{b}$ are column vectors of length N. Eq. (1.2) is a very classical problem in mathematics. Gaussian elimination is a direct method, it has a complexity of $\mathcal{O}(N^3)$, making it very slow when N is large. Additional direct methods, e.g. lower-uppper (LU) decomposition or singular value decomposition (SVD) all have similar complexity restrictions.

An alternative is to use the iterative methods [45, 46, 47, 48]. Such iterative methods represent an optimization process. Starting from an initial guess $\boldsymbol{x}_0$, the iterative method reduces the norm of the error $|\mathbb{A}\tilde{\boldsymbol{x}} - \boldsymbol{b}|$ to a small value ϵ in finite steps. Here $\tilde{\boldsymbol{x}}$ is an approximate solution to $\boldsymbol{x}$. Each optimization requires at least one evaluation of matrix vector product (MVP): $\boldsymbol{z} = \mathbb{A}\boldsymbol{y}$, where $\boldsymbol{y}$ is a column vector provided by the optimizer, and $\boldsymbol{z}$ is the MVP. The cost of an MVP, t_{MVP} is proportional to the number of nonzero elements in $\mathbb{A}$. If it is a sparse matrix, as the case in FEM, the cost is $\mathcal{O}(N)$. On the other hand, in IEs, the cost is usually $\mathcal{O}(N^2)$ by definition. Fortunately, many of the“fast” algorithms can reduce the cost from $\mathcal{O}(N^2)$ to $\mathcal{O}(N\log(N))$ or even $\mathcal{O}(N)$ [49, 50, 51]. The total time is $t_{total} = t_{MVP}N_{iter}$, where N_{iter} is the number of iterations. The time t_{MVP} is almost optimal in the sense that the cost is linear or quasilinear. However, N_{iter} is difficult to predict and control, it is related to the condition number of $\mathbb{A}$:

$$\mathrm{cond}(\mathbb{A}) = \sqrt{\frac{\sigma_{\max}(\mathbb{A}^\dagger\mathbb{A})}{\sigma_{\min}(\mathbb{A}^\dagger\mathbb{A})}}, \tag{1.3}$$

where $\mathbb{A}^\dagger$ is the transpose conjugate of $\mathbb{A}$, $\sigma_{\max}(\mathbb{A}^\dagger\mathbb{A})$ and $\sigma_{\min}(\mathbb{A}^\dagger\mathbb{A})$ are the largest and smallest eigenvalues of $\mathbb{A}^\dagger\mathbb{A}$. The larger the condition number, the more difficult the problem is. A common practice to make Eq. (1.2) more tractable is to use a precondtioner matrix $\mathbb{P}$ of size $N \times N$:

$$\mathbb{P} \cdot \mathbb{A}\boldsymbol{x} = \mathbb{P} \cdot \boldsymbol{b}. \tag{1.4}$$

The preconditioner is constructed such that $\mathrm{cond}(\mathbb{P} \cdot \mathbb{A}) \ll \mathrm{cond}(\mathbb{A})$. Ideally, $\mathbb{P}$ is close to the inverse of $\mathbb{A}$. The choice of $\mathbb{P}$ is an art and a science.

1.4 Numerical errors

Errors of numerical differentiation can be significant in FEM and IEs. The most commonly used differential operators are: $\frac{\partial}{\partial x}, \frac{\partial}{\partial y}, \frac{\partial}{\partial z}, \frac{\partial}{\partial t}, \frac{\partial^2}{\partial t^2}$, $\nabla = \hat{\mathbf{x}}\frac{\partial}{\partial x} + \hat{\mathbf{y}}\frac{\partial}{\partial y} + \hat{\mathbf{z}}\frac{\partial}{\partial z}$, $\nabla^2 = \frac{\partial^2}{\partial x^2} + \frac{\partial^2}{\partial y^2} + \frac{\partial^2}{\partial z^2}$. These operators give rise to errors in numerical methods. The errors from the differential operators are very sensitive to the mesh size, mesh quality and elemental shapes. In general, reducing the mesh size yields better accuracy, but it is not always true. Moreover, in FEM, the quality of a triangular or quadrilateral mesh is important. One should avoid small angles in these elements to reduce error. Moreover, in FEM, it is generally believed that hexahedrons can be better than tetrahedrons in terms of accuracy.

Another major source of error exists extensively in all kinds of numerical integrals. FEMs and IEs produce a large amount of integrals, most of which do not have a closed analytic solution, although there are exceptions. These integrals can be one-, two- or three dimensional. The higher the dimension, the more difficult to evaluate. Some higher dimensional integrals are reducible to one dimensional by integral formulas. Some typical integrals are: $\int_{x_1}^{x_2} e^{-\sqrt{-1}\sqrt{x^2+a^2}}dx$, $\int_0^1 dx \int_0^1 dy \frac{e^{\sqrt{-1}\sqrt{(x-c)^2+(dy-e)^2}}}{\sqrt{(x-a)^2+(by-c)^2}}$, $\int_0^1 dx \int_0^1 dy \int_0^1 dz \frac{1}{\sqrt{(x-a)^2+(by-c)^2+(dz-e)^2}}$, here a, b, c, d, e are constants. The one dimensional integrals can be evaluated by Gaussian quadrature. In the recent years, the double exponential quadrature draws intensive attention [52]. The basis idea of these quadrature methods is the approximation: $\int_0^1 f(x)dx \approx \sum_{n=1}^{n=N_Q} w_n f(x_n)$, where N_Q is the number of quadrature points, w_n is the weight, x_n is the abscissa. The quadrature rules [53, 54] cannot work well if the integrands have singularties[1].

1.5 Outline and contributions of this work

The dissertation is divided into six chapters. Chapter 1 introduces background and motivation of the research. Chapter 2 is a detailed discussion of the tetrahedral element based implementation in Micromagetics and gives implementation details of the FastMag micromagnetic solver. Chapter 3 presents Jacobian matrix free implementation of the Jacobian matrix vector products required in implicit micromagnetic solvers. Chapter 4 is dedicated to discretization of surface integral equations for Electromagnetics, including new quadrilateral-based basis and testing functions. Chapter 5 applies the basis functions in a variety of problems. Chapter 6 presents formulations of volume integral equations and their applications.

---

[1] A singularity in a function is a point where the value of the function blows up and tends to infinity.

Chapter 2

FastMag: a fast and accurate micromagnetic solver

Micromagnetic solvers for the LLGE have a significant predictive power and are important for the ability to analyze and design magnetic systems [55, 56]. Micromagnetic simulations of large-scale and complex structures, however, may be very time consuming or impossible and their acceleration methods are of high importance. Currently available micromagnetic solvers are based on the finite-difference method (FDM) or finite-element method (FEM) [57, 58, 59, 60]. FDMs can be efficient for problems of regular shape discretized uniformly, but they are less suited for general problems with complex geometrical and material compositions. FEMs provide flexible tools for micromagnetic simulations of complex general structures, but their efficient implementations for large-scale structures are yet to be shown.

This chapter starts with a brief introduction to the physics of magnetic materials. Then, it presents details of the implementation of an efficient micromagnetic solver, which is a foundation of the FastMag simulator. FastMag is a fast and accurate micromagnetic solver well-suited for large scale simulations. It solves the Landau-Lifshitz-Gilbert equation (LLGE) and can handle multiscale problems with a high computational efficiency.

2.1 Landau-Lifshitz-Gilbert equation

2.1.1 Energies in magnetic materials

All materials are magnetic to some extent [61, 62]. Most materials respond weakly to an external magnetic field, they are paramagnetic or diamagnetic. Ferromagnetic materials [63, 64], including transition metals Fe, Co, Ni and many of their compounds, can create strong force to be felt. Net spontaneous magnetization can exist in these materials even without the external magnetic field. The spin and orbital momentums of the 3d electrons in the outer shells of the atoms of these elements result in magnetic dipole moments. In micromagnetics the discrete atomistic moments are represented as a continuous magnetization vector:

$$\mathbf{M} = \hat{\mathbf{x}} M_x + \hat{\mathbf{y}} M_y + \hat{\mathbf{z}} M_z. \tag{2.1}$$

$\mathbf{M}$ is measured in amperes per meter in SI units. Let $\hat{\mathbf{m}} = \frac{\mathbf{M}}{|\mathbf{M}|} = \hat{\mathbf{x}} m_x + \hat{\mathbf{y}} m_y + \hat{\mathbf{z}} m_z, m_x^2 + m_y^2 + m_z^2 = 1$. $\hat{\mathbf{m}}$ is a unit vector, denoting the direction of $\mathbf{M}$.

A magnetic domain, denoted as Ω, has associated total energy E_{Total}:

$$E_{\text{Total}} = \iiint_{\Omega} (\epsilon_{\text{a}} + \epsilon_{\text{ani}} + \epsilon_{\text{ex}} + \epsilon_{\text{m}}) dV, \tag{2.2}$$

where the energy density components are:

- $\epsilon_{\text{a}} = -\mu_0 \mathbf{M} \cdot \mathbf{H}_{\text{a}}$, the Zeeman energy, $\mathbf{H}_{\text{a}}$ is the applied or external field. ϵ_a is minimal while $\mathbf{M}$ is parallel to the $\mathbf{H}_{\text{a}}$, and it is maximal when they are antiparallel.

- $\epsilon_{\text{ani}} = -\frac{1}{2} K_U (\hat{\mathbf{m}} \cdot \hat{\mathbf{k}})^2$, the uniaxial anisotropy field, $\hat{\mathbf{k}}$ is a unit vector called easy axis. Here K_U is the magnetocrystalline anistropy energy density. The uniaxial anisotropic energy ϵ_{ani} is small when $\mathbf{M}$ points along the easy axis $\hat{\mathbf{k}}$, and it is large when it is perpendicular to $\hat{\mathbf{k}}$.

- $\epsilon_{\text{ex}} = A|\nabla \hat{\mathbf{m}}|^2 = A[(\nabla m_x)^2 + (\nabla m_y)^2 + (\nabla m_z)^2]$ is the exchange energy, where A is exchange constant. The exchange energy tends to make $\mathbf{M}$ as uniform as possible. The exchange energy is largely responsible for keeping the magnetization in order.

- $\epsilon_{\mathrm{m}} = -\frac{1}{2}\mu_0 \mathbf{M}\cdot\mathbf{H}_{\mathrm{m}}$ is the demagnetization energy. The magnetic flux density $\mathbf{B} = \mu_0(\mathbf{H}_{\mathrm{m}} + \mathbf{M})$. $\mathbf{H}_{\mathrm{m}}$, produced by $\mathbf{M}$, is called dipolar or magnetostatic field. The dipolar energy ϵ_{m} tries to make $\mathbf{M}$ behave randomly to shrink $\mathbf{B}$.

This is the simplest model for energies in magnetic materials. Other terms such as the Ruderman-Kittel-Kasuya-Yosida (RKKY) interactions [65] and the spin transfer torques (STTs) [66], may also appear in the LLGE. The magnetization tries to align in a way such that the total energy is minimized [67]. The competence between the different energies decides the temporal evolution of $\mathbf{M}$.

2.1.2 Effective field

The different energies influence the temporal evolution of $\mathbf{M}$ by exerting an effective field, indicated by $\mathbf{H}_{\mathrm{eff}}$:

$$\mathbf{H}_{\mathrm{eff}} = -\frac{1}{\mu_0}\frac{\delta\epsilon_{Total}}{\delta\mathbf{M}}. \tag{2.3}$$

where $\epsilon_{\mathrm{Total}} = \epsilon_{\mathrm{a}} + \epsilon_{\mathrm{ani}} + \epsilon_{\mathrm{ex}} + \epsilon_{\mathrm{m}}$ is the total energy density, $\mathbf{H}_{\mathrm{eff}}$ has four components:

$$\mathbf{H}_{\mathrm{eff}} \triangleq \mathbf{H}_{\mathrm{a}} + \mathbf{H}_{\mathrm{ani}} + \mathbf{H}_{\mathrm{ex}} + \mathbf{H}_{\mathrm{m}}, \tag{2.4}$$

where $\mathbf{H}_{\mathrm{a}} = -\frac{1}{\mu_0}\frac{\delta\epsilon_a}{\delta\mathbf{M}}$ is the applied field. $\mathbf{H}_{\mathrm{ani}} = -\frac{1}{\mu_0}\frac{\delta\epsilon_{ani}}{\delta\mathbf{M}} \triangleq H_K(\hat{\mathbf{m}}\cdot\hat{\mathbf{k}})\hat{\mathbf{k}}$ is the anistropy field, $\hat{\mathbf{k}}$ is the uniaxial axis, H_K is the strength of the uniaxial anisotropy. $\mathbf{H}_{\mathrm{ex}} = l_{ex}^2\nabla^2\mathbf{M}$ is the exchange field, where l_{ex} is the exchange length. $\mathbf{H}_{\mathrm{m}} = \nabla\nabla\cdot\iiint_\Omega \mathbf{M}(\mathbf{r}')\frac{1}{4\pi|\mathbf{r}-\mathbf{r}'|}d\mathbf{r}'$ is the demagnetization field.

Evaluating $\mathbf{H}_{\mathrm{eff}}$ is a critical part of the numeric LLGE simulator. Since $\mathbf{H}_{\mathrm{a}}$ is given, there is no need to evaluate it. The evaluation of $\mathbf{H}_{\mathrm{ani}}$ is direct, as it is simply an algebraic function. The difficulties are pertinent to the other two field components. $\mathbf{H}_{\mathrm{ex}}$ utilizes a differential operator, and $\mathbf{H}_{\mathrm{m}}$ employs both differential and integral operators. These operators are bottlenecks of accuracy and speed of the simulators.

Here we list a few examples. Two parallel infinitely large planar plates are located at $z = 0$ and $z = d$. If $\mathbf{M} = \hat{\mathbf{z}}M\cos(\theta) + \hat{\mathbf{x}}M\sin(\theta)$, here θ is a constant, the dipolar field between the plates is $\mathbf{H}_{\mathrm{m}} = -\hat{\mathbf{z}}M\cos(\theta)$. Outside the plates the field is zero. Another case is a unit sphere. If the magnetization is $\mathbf{M} = \hat{\mathbf{z}}$, inside

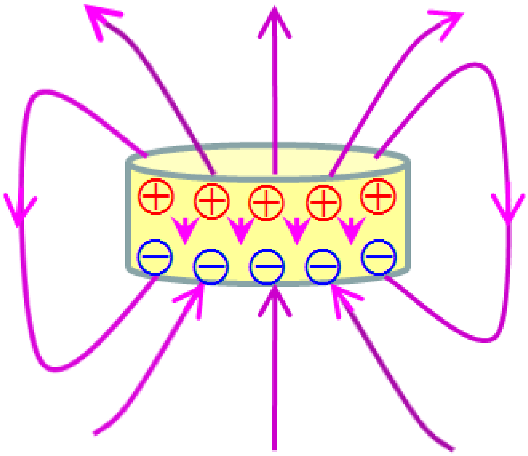

Figure 2.1: Magnetic field generated by a magnetic dipole. The ⊕ symbols denote positive magnetic charge, The ⊖ symbols depict the negative. The arrows show the direction of the magnetic field lines.

the sphere $\mathbf{H}_\mathrm{m} = -\frac{1}{3}\hat{\mathbf{z}}$. If $\mathbf{M} = \hat{\mathbf{x}}x + \hat{\mathbf{y}}y + \hat{\mathbf{z}}z$, one has $\mathbf{H}_\mathrm{m} = -\hat{\mathbf{x}}x - \hat{\mathbf{y}}y - \hat{\mathbf{z}}z$. Clearly we observe that the dipolar field tries to align anti-parallel to the original magnetization vector.

2.1.3 Dynamic equation

The temporal evolution of the magnetization is best described by the LLGE:

$$\frac{\partial \mathbf{M}}{\partial t} = -\left(\gamma \mathbf{M} \times \mu_0 \mathbf{H}_\mathrm{eff} - \alpha \frac{\mathbf{M}}{M_S} \times \frac{\partial \mathbf{M}}{\partial t}\right), \tag{2.5}$$

where M_S is the saturation magnetization. α and M_S are constants that depend on temperature and material compositions. Eq. (2.5) is an implicit form, since $\frac{\partial \mathbf{M}}{\partial t}$ appears on both sides of the equation. It has an explicit form:

$$\frac{\partial \mathbf{M}}{\partial t} = -\frac{\gamma \mu_0}{1+\alpha^2}\left[\mathbf{M} \times \mathbf{H}_\mathrm{eff} + \frac{\alpha}{M_S}\mathbf{M} \times (\mathbf{M} \times \mathbf{H}_\mathrm{eff})\right]. \tag{2.6}$$

Let $\mathbf{T}_1 = \mathbf{M} \times \mathbf{H}_\mathrm{eff}, \mathbf{T}_2 = \mathbf{M} \times (\mathbf{M} \times \mathbf{H}_\mathrm{eff})$. $\mathbf{T}_1$ is a magnetic torque. Since $\mathbf{T}_1 \cdot \mathbf{H}_\mathrm{eff} = 0$, this torque makes $\mathbf{M}$ to rotate about $\mathbf{H}_\mathrm{eff}$. It represents a precessional process. Since $\mathbf{T}_2 = (\mathbf{M} \cdot \mathbf{H}_\mathrm{eff})\mathbf{M} - (\mathbf{M} \cdot \mathbf{M})\mathbf{H}_\mathrm{eff}$, clearly $\mathbf{T}_2$ has a component along

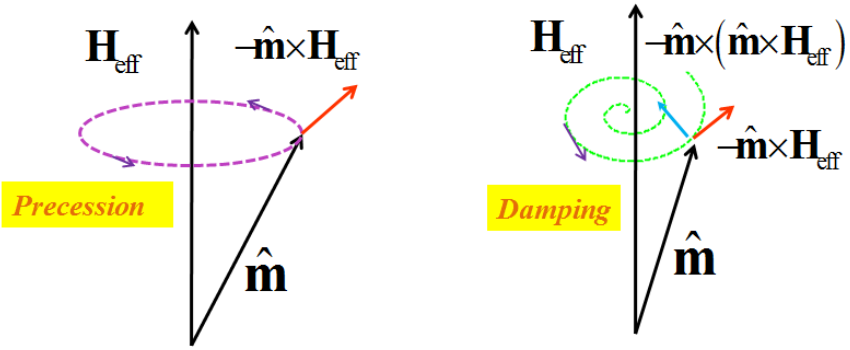

Figure 2.2: Illustration of the precessional and damping terms in the LLGE. The precessional term $\mathbf{T}_1$ makes $\hat{\mathbf{m}}$ rotate about $\mathbf{H}_{\text{eff}}$. On the other hand, the damping torque $\mathbf{T}_2$ makes the $\hat{\mathbf{m}}$ attracted to the axis of $\mathbf{H}_{\text{eff}}$.

the direction of $\mathbf{H}_{\text{eff}}$. Thus it makes the $\mathbf{M}$ to follow the direction of $\mathbf{H}_{\text{eff}}$. It indicates the energy dissipation mechanisms in the magnetic materials.

Eq. (2.6) is an explicit form because $\frac{\partial \mathbf{M}}{\partial t}$ appears only on the left side of the equation. Multiplying $\mathbf{M}\cdot$ on both sides of Eq. (2.6) yields

$$\mathbf{M}\cdot\frac{\partial \mathbf{M}}{\partial t} = 0. \tag{2.7}$$

It indicates that $\frac{\partial}{\partial t}(\mathbf{M}\cdot\mathbf{M}) = 0$. As a result, the magnitude of the magnetization is always a constant in time, i.e. $|\mathbf{M}| = M_S$. Therefore, the LLGE is often more compactly and conveniently written in a normalized form:

$$\frac{\partial \hat{\mathbf{m}}}{\partial t} = -\frac{\gamma}{1+\alpha^2}\left[\hat{\mathbf{m}}\times\mathbf{H}_{\text{eff}} + \alpha\hat{\mathbf{m}}\times(\hat{\mathbf{m}}\times\mathbf{H}_{\text{eff}})\right], \tag{2.8}$$

where $\hat{\mathbf{m}} = \mathbf{M}/M_S$ is a unit vector. Eq. (2.8) is a time domain ODE. Its right-hand side (RHS) depends on the evaluation of $\mathbf{H}_{\text{eff}}$. In numerical solutions, we have a mesh of tetrahedrons or hexahedrons, and the number of vertices is V. $\hat{\mathbf{m}}$ is interpolated by scalar basis functions:

$$\hat{\mathbf{m}}(\mathbf{r}) \approx \sum_{n=1}^{n=V} b_n(\mathbf{r})\hat{\mathbf{m}}_n. \tag{2.9}$$

where b_n is a scalar basis function (BF) associated with the nth vertex. It is interesting to see that, although $\hat{\mathbf{m}}$ is a vector and it seems more reasonable to use the v-BFs, however, the norm-preserving property of $\hat{\mathbf{m}}$ makes it more convenient to use the s-BFs.

2.2 Finite element discretizations

In this part we show how to solve the LLGE by using FEM by using tetrahedral discretization [50, 68, 69, 70, 71]. Tetrahedrons are preferred in FEM due to their excellent flexibility in modeling geometries. As a very graceful and convenient tool, the simplex coordinates are introduced for triangles and tetrahedrons. Triangles model the surface of many complex bodies. The tetrahedrons are used to mesh the volume of a three dimensional structure. While triangles are not used directly in LLGE, they are important in the sense that, the boundary of any tetrahedral mesh, is actually a triangular mesh. In micromagnetics, many phenomena are due to surface interactions such as anti-ferromagnetic coupling, and interlayer exchange coupling.

2.2.1 Simplex coordinates for triangles

A triangle has three vertices **A**, **B**, **C**, their Cartesian coordinates are $\mathbf{r}_1, \mathbf{r}_2, \mathbf{r}_3$, respectively. They must satisfy $|(\mathbf{r}_1 - \mathbf{r}_2) \times (\mathbf{r}_3 - \mathbf{r}_2)| > 0$.

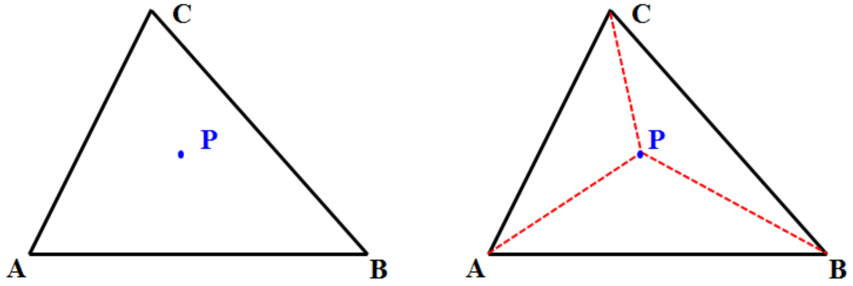

Figure 2.3: A triangle is formed by three vertices **ABC**. **P** is an arbitrary point inside **ABC**, and divides it into three smaller triangular elements. The area of **ABC** is S_0.

It is possible to use the Cartesian frame (x, y, z) to denote a point inside the triangle, or to define functions over it. However, it is very inconvenient since each tetrahedron is different from any other one. The alternative way is to use *simplex coordinates*, which are ξ_1, ξ_2, ξ_3:

$$\xi_1 = \frac{S_A}{S_0}, \xi_2 = \frac{S_B}{S_0}, \xi_3 = \frac{S_C}{S_0}. \tag{2.10}$$

where S_0, S_A, S_B, S_C are the areas of triangles $\mathbf{ABC}, \mathbf{PBC}, \mathbf{PCA}, \mathbf{PAB}$, respectively. Since $S_0 = S_A + S_B + S_C$, it follows immediately the partition of unity:

$$\xi_1 + \xi_2 + \xi_3 = 1. \tag{2.11}$$

Therefore, any triangle is can be regarded as a linear transform from a parameter space $\xi_1, \xi_2 \leq 1, \xi_1 + \xi_2 \leq 1$ (which is actually a right isosceles triangle) to its real space. The parameter space constitutes an isosceles triangle. By using the parameters, the position vector of $\mathbf{P}$ takes a form:

$$\boldsymbol{\rho} = \mathbf{r}_1\xi_1 + \mathbf{r}_2\xi_2 + \mathbf{r}_3\xi_3. \tag{2.12}$$

These simplex coordinates are nonnegative linear functions of $\boldsymbol{\rho}$, where $\boldsymbol{\rho}$ is a point on the triangle. $\xi_1 = 1$ at point **A**. Similarly, $\xi_2 = 1$ at point **B**, $\xi_3 = 1$ at point **C**. We say that ξ_1 is associated with vertex **A**.

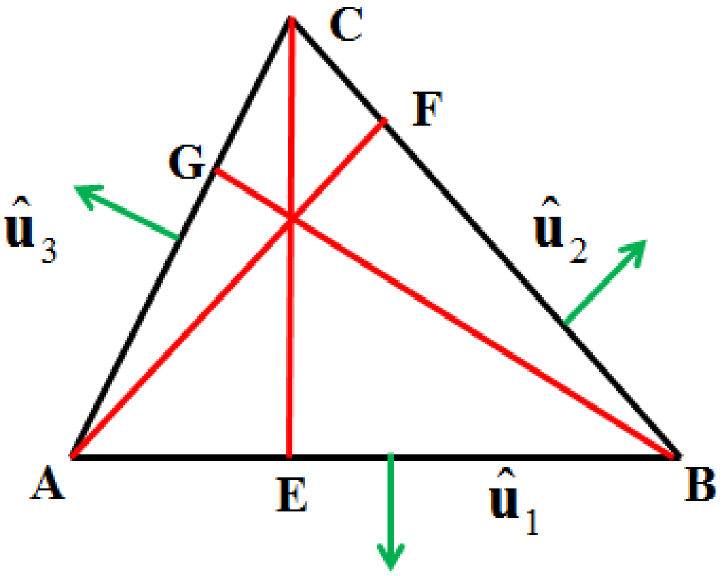

Figure 2.4: A triangle is formed by three vertices **ABC**. The three unit vectors $\hat{\mathbf{u}}_1, \hat{\mathbf{u}}_2, \hat{\mathbf{u}}_3$ satisfy $\hat{\mathbf{u}}_1 \perp \mathbf{AB}, \hat{\mathbf{u}}_2 \perp \mathbf{BC}, \hat{\mathbf{u}}_3 \perp \mathbf{CA}$.

Let $\hat{\mathbf{u}}_1$, $\hat{\mathbf{u}}_2$, $\hat{\mathbf{u}}_3$ be unit vectors pointing outwards to the edges (see the green arrows in the above figure). Moreover, $\mathbf{AB} \perp \mathbf{CE}$, $\mathbf{BC} \perp \mathbf{AF}$, $\mathbf{CA} \perp \mathbf{BG}$. The gradient of the simplex coordinates is:

$$\nabla_S \xi_1 = -\frac{\hat{\mathbf{u}}_2}{|\mathbf{AF}|}, \nabla_S \xi_2 = -\frac{\hat{\mathbf{u}}_3}{|\mathbf{BG}|}, \nabla_S \xi_3 = -\frac{\hat{\mathbf{u}}_1}{|\mathbf{CE}|}. \tag{2.13}$$

In a triangular mesh, a vertex O is surrounded by a number of triangles. Hence, the domain of a simplex coordinate ξ_i also spans the same triangles. Fig. 2.5 shows the magnitude of a simplex coordinate on an assemble of triangles.

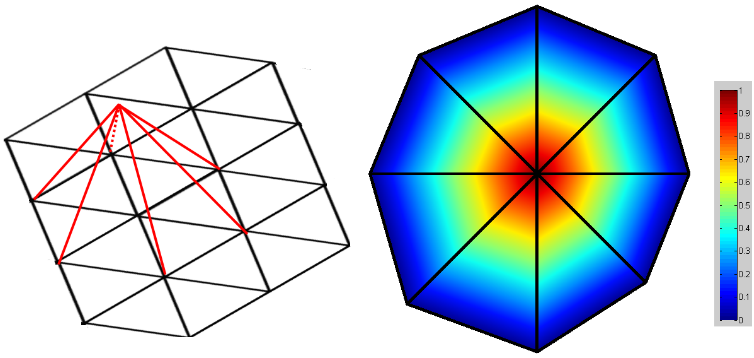

Figure 2.5: A “hat” function for the center vertex, which is surrounded by some triangles. The hat function has a value of 1 at the center, and tapers to zero at the boundary.

The surface gradient of the simplex coordinates are constant vectors. Therefore, we can reformulate the position vector $\boldsymbol{\rho}$ as:

$$\boldsymbol{\rho} = \nabla_S \xi_i \cdot (\boldsymbol{\rho} - \mathbf{r}_i) + 1, 1 \leq i \leq 3. \tag{2.14}$$

Eq. (2.14) is very useful for convolutional integrals of the Green function and the BFs. Since the most commonly used BFs are polynomials, their integrations over a triangle is very important.

$$\iint_{\Delta} \xi_1^i \xi_2^j \xi_3^k dS = \frac{2S_0 i! j! k!}{(2+i+j+k)!}, \tag{2.15}$$

where i, j, k are nonnegative integers. ξ_1, ξ_2, ξ_3 are completely symmetric in (2.15), which is also a manifest of the advantage of simplex coordinates. To make the accuracy as good as possible, the triangles should avoid having sharp angles.

2.2.2 Simplex coordinates for tetrahedrons

Four non-coplanar points form a tetrahedron [21]. The cartesian coordinates of these vertices are denoted as $\mathbf{r}_i = \hat{\mathbf{x}}x_i + \hat{\mathbf{y}}y_i + \hat{\mathbf{z}}z_i, (1 \leq i \leq 4)$. Any point inside the tetrahedron can be expressed as $\mathbf{r} = \hat{\mathbf{x}}x + \hat{\mathbf{y}}y + \hat{\mathbf{z}}z$, but it is in general inconvenient since it depends on each specific tetrahedron. A more common practice is to use *simplex coordinates*, which are a normalized coordinate system independent of a concrete tetrahedron. There are four simplex coordinates, i.e. $\xi_i, (1 \leq i \leq 4)$.

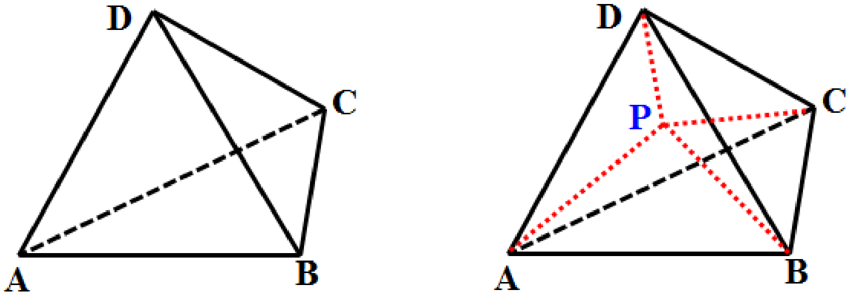

Figure 2.6: A tetrahedron is formed by four vertices **ABCD**. **P** is an arbitrary point inside **ABCD**, and divides it into four smaller tetrahedral elements.

Let the vertices $\mathbf{A}, \mathbf{B}, \mathbf{C}, \mathbf{D}$ be $\mathbf{r}_1$ through $\mathbf{r}_4$, they form the original tetrahedron T_0, whose volume is V_0. V_0 is a mixed product of vectors:

$$V_0 = \frac{1}{6}|(\mathbf{B} - \mathbf{A}) \times (\mathbf{C} - \mathbf{A}) \cdot (\mathbf{D} - \mathbf{A})|. \tag{2.16}$$

$\mathbf{r}$ denotes the coordinate of an arbitrary point $\mathbf{P}$ inside the tetrahedron. Clearly, T_0 is divided into four smaller tetrahedrons: $\mathbf{PBCD}, \mathbf{PCDA}, \mathbf{PDAB}, \mathbf{PABC}$, which are numbered T_A, T_B, T_C, T_D, respectively. The simplex coordinates are:

$$\xi_1 = \frac{V_A}{V_0}, \xi_2 = \frac{V_B}{V_0}, \xi_3 = \frac{V_C}{V_0}, \xi_4 = \frac{V_D}{V_0}. \tag{2.17}$$

These coordinates are a linear combination of x, y, z, and are nonnegative and have a simple partition of unity relation:

$$\xi_1 + \xi_2 + \xi_3 + \xi_4 = \frac{V_A}{V_0} + \frac{V_B}{V_0} + \frac{V_C}{V_0} + \frac{V_D}{V_0} = 1. \tag{2.18}$$

Eq. (2.18) is important to ensure the completeness of the basis functions. A point $\mathbf{r}$ inside the tetrahedron is $\mathbf{r} = \sum_{n=1}^{n=4} \mathbf{r}_n \xi_n$. A general formula for integrating the polynomials of the simplex coordinates is:

$$\iiint_{T_0} \xi_1^i \xi_2^j \xi_3^k \xi_4^l dV = \frac{6V_0 i!j!k!l!}{(i+j+k+l+3)!}, \tag{2.19}$$

where i, j, k, l are integers. The simplex coordinates are used to define functions over a tetrahedral region. Clearly, the simplex coordinates are independent of any specific tetrahedron, and it is very convenient to use. The gradient of the functions ξ_i is a constant vectors. In a tetrahedron, if the magnetization vectors are known only at the four vertices. The magnetization vector inside the volume is interpolated linearly as

$$\mathbf{M}(\mathbf{r}) \approx \sum_{i=1}^{i=4} \mathbf{M}_i \xi_i(\mathbf{r}). \tag{2.20}$$

Eq. (2.20) defines a continuous and first order differentiable function. Higher order basis functions, which are polynomials of $\xi_1, \xi_2, \xi_3, \xi_4$, are smoother and can make the numeric method more accurate at the price of a higher computational cost. The quadratic basis functions are also investigated.

2.3 Field evaluation

2.3.1 Evaluation of the applied field

I$\mathbf{H}_{\text{app}}$ is a given function or it might need to be solved based on other quantities such as current. For example, $\mathbf{H}_{\text{app}}$ generated by a coil current I is given by the Biot-Savart formula:

$$\mathbf{H}_{\text{app}}(\mathbf{r}) = \nabla \times \oint_{Coil} \frac{I}{4\pi|\mathbf{r}-\mathbf{r}'|} d\mathbf{r}' = \frac{I}{4\pi} \oint_{Coil} \frac{\mathbf{r}-\mathbf{r}'}{|\mathbf{r}-\mathbf{r}'|^3} \times d\mathbf{r}'. \tag{2.21}$$

The coil is formed by a number of line segments, represented by N_c points. The coordinates of the points are $\mathbf{r}_1, \ldots, \mathbf{r}_{N_c}$. The integral in Eq. (2.21) is then converted into some summations:

$$\mathbf{H}_{\text{app}}(\mathbf{r}) \approx \frac{I}{4\pi} \sum_{i=1}^{i=N_c-1} \frac{\frac{\mathbf{r}_i+\mathbf{r}_{i+1}}{2} - \mathbf{r}}{|\frac{\mathbf{r}_i+\mathbf{r}_{i+1}}{2} - \mathbf{r}|^3} \times (\mathbf{r}_{i+1} - \mathbf{r}_i). \tag{2.22}$$

2.3.2 Evaluation of exchange field with a tetrahedral mesh

$\mathbf{H}_{\text{ex}}$ is modeled by the Laplacian operator, i.e. $\mathbf{H}_{\text{ex}} = M_S l_{\text{ex}}^2 \nabla^2 \hat{\mathbf{m}}$, where $\nabla^2 = \frac{\partial^2}{\partial x^2} + \frac{\partial^2}{\partial y^2} + \frac{\partial^2}{\partial z^2}$, l_{ex} is the exchange length. ∇^2 is essentially a linear and symmetric operator, its dicretization leads to a symmetric matrix. $\mathbf{H}_{\text{ex}}$ is approximated by the values of $\hat{\mathbf{m}}$ at surrounding vertices. To compute the value of $\mathbf{H}_{\text{ex}}$ at boundary nodes, an artificial boundary condition is used throughout the chapter:

$$\frac{\partial \hat{\mathbf{m}}}{\partial \hat{\mathbf{n}}} = \mathbf{0}. \tag{2.23}$$

The influence of $\mathbf{H}_{\text{ex}}$ is to make adjacent magnetizations to point to the same or similar directions. It seems intuitive to just put the ∇^2 operator in front of Eq. 2.9, and move it onto the s-BFs, yielding:

$$\nabla^2 \hat{\mathbf{m}}(\mathbf{r}) \approx \nabla^2 \sum_{n=1}^{n=V} b_n(\mathbf{r}) \hat{\mathbf{m}}_n = \sum_{n=1}^{n=V} \nabla^2 b_n(\mathbf{r}) \hat{\mathbf{m}}_n. \tag{2.24}$$

This method, however, does not work. Since here we have taken ξ_i as the s-BFs, which are linear functions. Then it follows $\nabla^2 b_n = 0$, indicating that these functions are insufficient to be differentiated twice. A common approach to overcome this problem is to use a carefully chosen testing function (TF) such that each function (either BF or TF) is differentiated only once. There are a few constraints on the choice of t_f. First of all, the number of TFs should be exactly the same as the BFs, otherwise we cannot get a square matrix to represent ∇^2. Second, the TFs must be linearly independent and complete. Thirdly, the TFs should be as simple as possible to facilitate implementation. $\nabla^2 f$ is assumed to be a slowly varying function in a small domain V_P, but the TF is a rapidly changing function in V_P. For an internal vertex P, surrounded by a volume V_P that consists of a number of tetrahedrons (typically 10-20), t_f much vanish at the boundary of the V_P. Second, t_f should be a positive function such that $\iint_{\partial V_P} t_f dS > 0$. In this way, ∇^2 can be approximated as:

$$\nabla^2 f \approx \frac{\iiint_\Omega t_f \nabla^2 f dV}{\iiint_\Omega t_f dV} = -\frac{\iiint_\Omega \nabla t_f \cdot \nabla f dV}{\iiint_\Omega t_f dV}, \tag{2.25}$$

where t_f is a testing function chosen by the programmers, f can be $M_x, M_y, \text{or} M_z$.

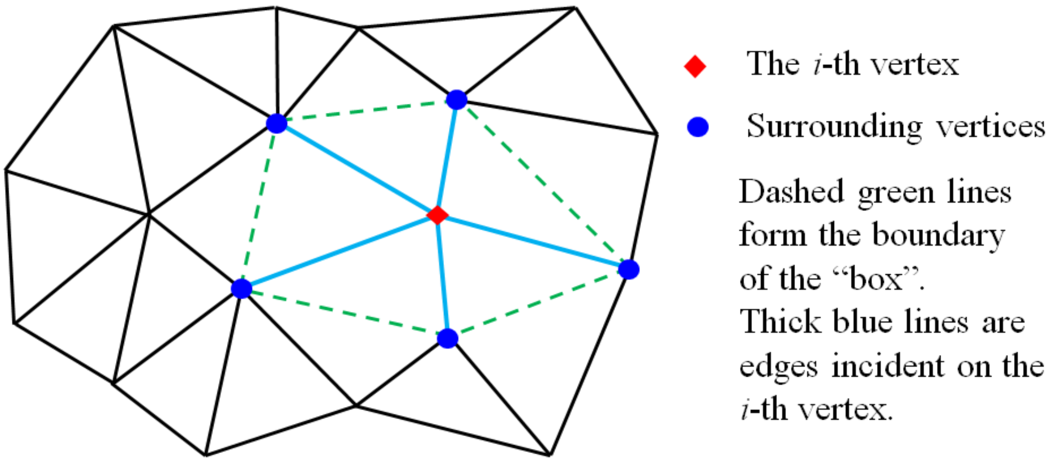

Figure 2.7: Illustration of the box method for a planar triangular mesh. The "◇" symbol in the center is the *i*-th node. The "○" symbols are the surrounding nodes.

As a natural choice, the simplex coordinates are used as BFs and TFs. This has been the most widely adopted formulation for exchange field evaluation in tetrahedral meshes. Let $\mathbb{L} \in \mathcal{R}^{N\times N}$ be the discretized stiffness matrix, its element is $\mathbb{L}_{mn} = \iiint_{\mathrm{T}} \nabla\xi_m \cdot \nabla\xi_n dV$. Inside a tetrahedron, both $\nabla\xi_m$ and $\nabla\xi_n$ are constant vectors, their dot product is also a constant, the integration is straightforward. The ratio $\frac{L_{max}}{L_{min}}$ is a critical factor that influences the speed of FastMag. Here L_{max} and L_{min} are the longest and shortest edge lengthes in the mesh. For this reason, if possible, the mesh should be uniformly discretized. We note that the exchange field, is one of the main reasons for the inaccuracy in numerical solutions. It is also responsible for the slowness in the time stepping of LLGE. The reason is due to the fact that the eigenvalues of $\mathbb{L}$ span from 0 to $+\infty$.

2.3.3 Evaluation of magnetostatic potential

We discuss three approaches for demagnetization field, all of which are mathematically equivalent.

Method I. This is to directly use the tensor Green function $\underline{\underline{\mathbf{G}}} = \nabla\nabla\frac{1}{4\pi|\mathbf{r}-\mathbf{r}'|}$. The demagnetization is written as:

$$\begin{aligned}\mathbf{H}_{\mathrm{m}}(\mathbf{r}) &= \iiint_{\Omega} \underline{\underline{\mathbf{G}}} \cdot \mathbf{M}(\mathbf{r}')d\mathbf{r}'. = \iiint_{\Omega} \nabla\nabla \frac{1}{4\pi|\mathbf{r}-\mathbf{r}'|} \\ &= \iiint_{\Omega} \left[\frac{1}{4\pi|\mathbf{r}-\mathbf{r}'|^3} - \frac{(\mathbf{r}-\mathbf{r}')(\mathbf{r}-\mathbf{r}')}{4\pi|\mathbf{r}-\mathbf{r}'|^5} \right] \cdot \mathbf{M}(\mathbf{r}')d\mathbf{r}'.\end{aligned} \tag{2.26}$$

Furthermore, it has a matrix form.

$$\begin{pmatrix} H_{m,x} \\ H_{m,y} \\ H_{m,z} \end{pmatrix} = \iiint_{\Omega} \begin{pmatrix} G_{xx} & G_{xy} & G_{xz} \\ G_{yx} & G_{yy} & G_{yz} \\ G_{zx} & G_{zy} & G_{zz} \end{pmatrix} \begin{pmatrix} M_x \\ M_y \\ M_z \end{pmatrix} d\mathbf{r}', \tag{2.27}$$

where $G_{uv} = \frac{\partial^2 G}{\partial u \partial v}$, u and v are any two of x, y, z. Eq. (2.26) directly transforms an input $\mathbf{M}$ into the demagnetization field. It is direct, and it has been used extensively in FDMs because the integrals on a cubic grid have a simple closed form. For FEMs, Eq. (2.26) is quite complex due to the high order singularity of $\underline{\underline{\mathbf{G}}}$ which absorbs double gradient operators $\nabla\nabla$. Since the matrix has nine elements, the evaluation could be implemented by nine times MVPs. If FFT is used, the FFTs of $G_{uv} = \frac{\partial^2 G}{\partial u \partial v}$ have been precomputed and stored, it would still require three FFT evaluations for M_x, M_y, M_z, and three inverse FFTs. Moreover, in this method the dyadic Green function is hypersingular and it requires corrections for the near field interactions, which takes a large amount of time and memory. To sum up, this method is very suited for FDMs but it is not an efficient candidate for FEMs.

Method II. This method relies on the scalar potential $\phi(\mathbf{r})$:

$$\phi(\mathbf{r}) = \iiint_{\Omega} \frac{\nabla' \cdot \mathbf{M}(\mathbf{r}')}{4\pi|\mathbf{r}-\mathbf{r}'|} d\mathbf{r}' - \oiint_{\partial\Omega} \frac{\hat{\mathbf{n}}(\mathbf{r}') \cdot \mathbf{M}(\mathbf{r}')}{4\pi|\mathbf{r}-\mathbf{r}'|} d\mathbf{r}'. \tag{2.28}$$

This method employs the volume charge $\rho_V = \nabla \cdot \mathbf{M}$ and surface charge $\rho_S = -\hat{\mathbf{n}} \cdot \mathbf{M}$. When the linear BFs are used, ρ_V is a piecewise constant and ρ_S is a linear function. The charge is a scalar quantity, and its convolution with the Green function needs only one FFT evaluation for the charge, and one inverse FFT. A drawback of this method is that it needs to differentiate the boundary nodes from the interior ones, bringing in an inconvenience.

Moreover, the volume charge obtained from numerical differentiation may have a poor accuracy if the magnetization vector has large spatial variations. Although it has been widely used, it was found to be numerically unstable for ultrathin plate problems, where the accuracy of the integrals is very crucial.

Method III. The scalar potential has another form:

$$\phi(\mathbf{r}) = \iiint_{\Omega} \mathbf{M}(\mathbf{r}') \cdot \nabla' \left(\frac{1}{4\pi|\mathbf{r}-\mathbf{r}'|} \right) d\mathbf{r}', \tag{2.29}$$

where $\phi(\mathbf{r})$ is the potential. The field is the gradient of the potential: $\mathbf{H}_{\mathrm{m}} = -\nabla\phi$, therefore it can be cast as:

$$\mathbf{H}_{\mathrm{m}}(\mathbf{r}) = \nabla \iiint_{\Omega} \mathbf{M}(\mathbf{r}') \cdot \nabla \frac{1}{4\pi|\mathbf{r}-\mathbf{r}'|} d\mathbf{r}'. \tag{2.30}$$

Let $G_x = \frac{\partial G}{\partial x}, G_y = \frac{\partial G}{\partial y}, G_z = \frac{\partial G}{\partial z}$, since $\nabla G \cdot \mathbf{M} = G_x M_x + G_y M_y + G_z M_z$, it seems that Eq. (2.30) must be carried out by three FFTs for $\mathbf{M}_x$, $\mathbf{M}_y$, $\mathbf{M}_z$ and one inverse FFT for the potential. Moreover, G_x, G_y, G_z are more singular than G, so it is quite cumbersome to evaluate the integrals in Eq. (2.30) in FEMs. However, if we assume that the magnetization vector inside each tetrahedral element is a constant, Eq. (2.30) can be simplified.

The rest of this subsection is devoted to the third method, which is simple, accurate and robust. The geometry is formed by a number of tetrahedrons, i.e. $\Omega = \bigcup_{n=1}^{n=N} \mathrm{T}_n$, where T_n is the n-th tetrahedron. Inside each tetrahedron, the magnetization is assumed to be uniform, and the magnetization vector is:

$$\mathbf{m}_C = \frac{1}{4} \sum_{n=1}^{n=4} \hat{\mathbf{m}}_n, \tag{2.31}$$

where $\hat{\mathbf{m}}_n$ is the magnetization vector at the n-th vertex of the tetrahedron. Note that $\mathbf{m}_C$ is generally not a unit vector. Then it follows for the far field

$$\iiint_{\mathrm{Tet}} \hat{\mathbf{m}}(\mathbf{r}) \cdot \nabla' \frac{1}{|\mathbf{r}-\mathbf{r}'|} d\mathbf{r}' \approx \mathbf{m}_C \cdot \iiint_{\mathrm{Tet}} \nabla' \frac{1}{|\mathbf{r}-\mathbf{r}'|} d\mathbf{r}' = \mathbf{m}_C \cdot \oiint_{\partial\mathrm{Tet}} \frac{\hat{\mathbf{n}}'}{|\mathbf{r}-\mathbf{r}'|} d\mathbf{r}'. \tag{2.32}$$

Note that the boundary of a tetrahedron consists of four triangles. The integral over a triangle can be executed as follows:

$$\iint_{\Delta} \frac{\hat{\mathbf{m}}(\mathbf{r})}{|\mathbf{r}-\mathbf{r}'|} d\mathbf{r}' \approx \frac{\mathbf{m}_C S_{\Delta}}{3} \sum_{n=1}^{n=3} \frac{1}{|\mathbf{r}-\mathbf{r}_n|}, \tag{2.33}$$

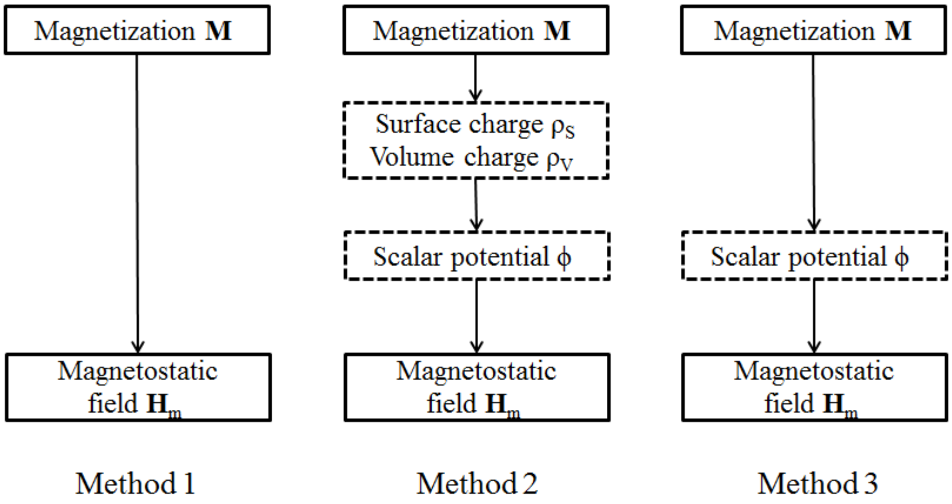

Figure 2.8: A comparison of the three methods for evaluating the demagnetization field in FEMs. The quantities contained in the dashed boxes such as magnetic charge and potential are fictitious.

where S_Δ is the area of a triangle. In the integration, the original vertices of the mesh are used as quadrature points, which is not only convenient but also very economic. Since each vertex is shared by 10 to 20 tetrahedrons, this method leads to a large saving. Experimental results show that this method is very stable and accurate enough for our applications. It should be mentioned that there are many alternative quadrature rules that result in better accuracy. However, these rules require a much larger number of quadrature points. The small improvement in the accuracy is counteracted by a much larger computational time (at least 20 times larger). For this reason, we do not use the more complex and accurate quadrature rules [72, 73]. Besides, this approach does not require one to distinguish the boundary nodes from the other vertices, so it is more convenient.

Another advantage of this method is related to the analytic integrals for the near field corrections. Since the integrals are all two dimensional surface integrals in this method, they are much easier to handle than the three dimensional volumetric counterparts. A common drawback associated with **MethodII** and **MethodIII** is that when the potential is known, the field, defined with a gradient operator, has to be evaluated numerically with the mesh. Therefore, the overall accuracy critically depend on the quality of the mesh. Moreover, at the boundary $\mathbf{H}_\mathrm{m}$ is discontinuous in the normal direction. Therefore, it is not well-defined. Empirically, this gradient operator is not the major source of error.

2.4 Fast algorithms for field evaluations

In the preceding subsection, the vertices of the mesh are used as quadrature nodes [74, 75]. Suppose vertex i, whose position is $\mathbf{r}_i$ takes a collocated charge q_i. The potential at i is evaluated as:

$$\psi_i = \sum_{j=1, j\neq i}^{j=N} \frac{q_j}{4\pi|\mathbf{r}_i - \mathbf{r}_j|}, 1 \leq i \leq N. \tag{2.34}$$

Obviously, formula (2.34) indicates an $\mathcal{O}(N^2)$ complexity computation. When N is a small number, it is not slow. But when N is much larger, it becomes slow. There have been a number of algorithms that attacks this classical problem. The methods are in two categories. The famous Fast Multipole Method (FMM) and the Non-uniform Grid Interpolation (NGIM) are in the first class [41, 76, 77, 78, 40], which relies on a hierarchical decomposition of the computational domain. An octal tree is used to represent the structure. This kinds of methods employs the fact that the potential of the form $\frac{1}{|\mathbf{r}-\mathbf{r}'|}$ decays slowly when $\mathbf{r}$ and $\mathbf{r}'$ are well-separated.

Algorithms in the other category are purely algebraic, such as Fast Fourier Transform. The idea lies in the fact that the integral in Eq. (2.29) is a convolution, in which the Green function is translational invariant.

The correction is based on the analytic evaluation of an analytic integral $I(\mathbf{r}) = \iint_\Delta \frac{1}{|\mathbf{r}-\mathbf{r}'|} d\mathbf{r}'$, where Δ denotes a triangle. A vertex in a the mesh represents a spatial domain (Ω_V) formed by all tetrahedrons that share the vertex. Let d_{max} be the longest length of all edges that start from from V. Moreover two parameters are used, *RangeParameter*(β_{RP}) and *ErrorControl*(ϵ_c). All the vertices in enclosed by the sphere centered at V with a radius of $\beta_{RP} d_{max}$ are called near points. The number of near points is directly related to β_{RP}. The number of near points significantly influences the memory costs and accuracy. In practice we found that

$\beta_{RP} = 2.0$ would be sufficient. Moreover, not all near points need to be accounted for, we only choose the points that result in an error that is smaller than a threshold ϵ_c. In the implementation, the first step is to identify the a list of "near" points for every vertex. Two methods are presented here in the following subsection.

2.4.1 Analytic integrals for singularity extraction

All the integrals encountered in the singularity extraction can be reduced to the following form:

$$I(\mathbf{r}) := \iint_{\Delta} \frac{1}{|\mathbf{r} - \mathbf{r}'|} dS'. \tag{2.35}$$

The surface integral is difficult to handle, and what we can solve directly is line integrals. The idea is to find a vector function $\mathbf{f} = (\boldsymbol{\rho}' - \boldsymbol{\rho})|\mathbf{r}' - \mathbf{r}|^m |\boldsymbol{\rho}' - \boldsymbol{\rho}|^n$, where m and n are integers to be determined. The surface divergence of the function should satisfy:

$$\nabla'_S \cdot \mathbf{f} = \frac{1}{|\mathbf{r}' - \mathbf{r}|} \tag{2.36}$$

To identify m and n, one has:

$$\begin{aligned} \nabla'_S \cdot \mathbf{f} =& \nabla'_S \cdot [(\boldsymbol{\rho}' - \boldsymbol{\rho})|\mathbf{r}' - \mathbf{r}|^m |\boldsymbol{\rho}' - \boldsymbol{\rho}|^n] \\ =& (n+2)|\mathbf{r}' - \mathbf{r}|^m |\boldsymbol{\rho}' - \boldsymbol{\rho}|^n + m|\mathbf{r}' - \mathbf{r}|^{m-2} |\boldsymbol{\rho}' - \boldsymbol{\rho}|^{n+2} \end{aligned} \tag{2.37}$$

Comparing Eq. (2.36) with Eq. (2.37), one must have $m = 1$, $n = -2$. So the result is of the form:

$$\nabla'_S \cdot \frac{|\mathbf{r} - \mathbf{r}'|}{|\boldsymbol{\rho} - \boldsymbol{\rho}'|^2} (\boldsymbol{\rho} - \boldsymbol{\rho}') = \frac{1}{|\mathbf{r} - \mathbf{r}'|}, \tag{2.38}$$

where ∇'_S is a surface divergence operator that affects the primed quantities. By using surface divergence theorem and integration by parts, $I(\mathbf{r})$ is transformed into three line integrals, finally it has a closed form:

$$\begin{aligned} I(\mathbf{r}) =& \sum_{i=1}^{i=3} \left[d_i \ln \frac{s_i^+ + \sqrt{(s_i^+)^2 + d_i^2 + h^2}}{s_i^- + \sqrt{(s_i^-)^2 + d_i^2 + h^2}} \right] \\ & - h \sum_{i=1}^{i=3} \tan^{-1} \frac{d_i s_i^+}{d_i^2 + (s_i^+)^2 + h\sqrt{(s_i^+)^2 + d_i^2 + h^2}} \\ & + h \sum_{i=1}^{i=3} \tan^{-1} \frac{d_i s_i^-}{d_i^2 + (s_i^-)^2 + h\sqrt{(s_i^-)^2 + d_i^2 + h^2}}. \end{aligned} \tag{2.39}$$

The meanings of the quantities are listed in Eq. (2.40). In Fig. 2.9, $\mathbf{A}, \mathbf{B}, \mathbf{C}$ form

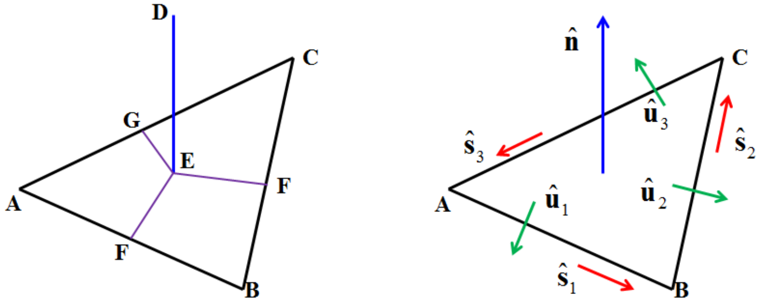

Figure 2.9: A triangle formed by **ABC**, **D** is the observation point.

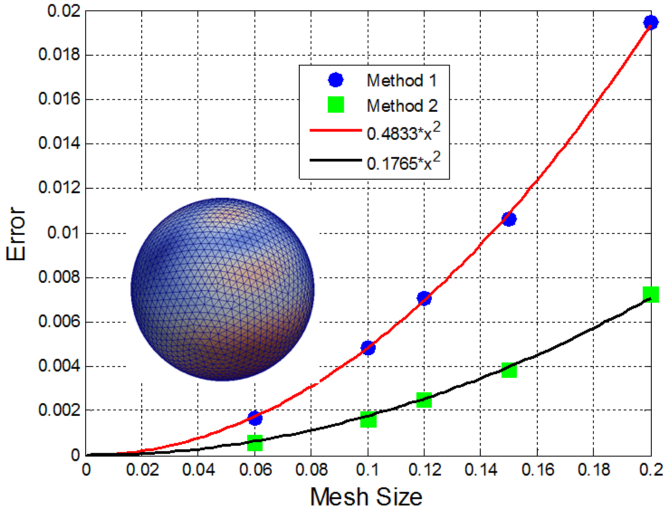

Figure 2.10: Accuracy of the proposed methods versus the mesh size. The unit sphere is uniformly polarized, i.e. $\hat{\mathbf{m}} = \hat{\mathbf{z}}$. The potential is $\phi = \frac{z}{3}$. It shows that the error in the potential is proportional to the square of the mesh size

a triangle, $\mathbf{r}$ is the coordinate of the observation point. ρ is the projection of $\mathbf{r}$ onto the plane formed by the triangle. $\mathbf{r}'$ is the integration point, since $\mathbf{r}$ is on the plane, it is also written as $\boldsymbol{\rho}'$. The quantities that are used in the analytic integrals

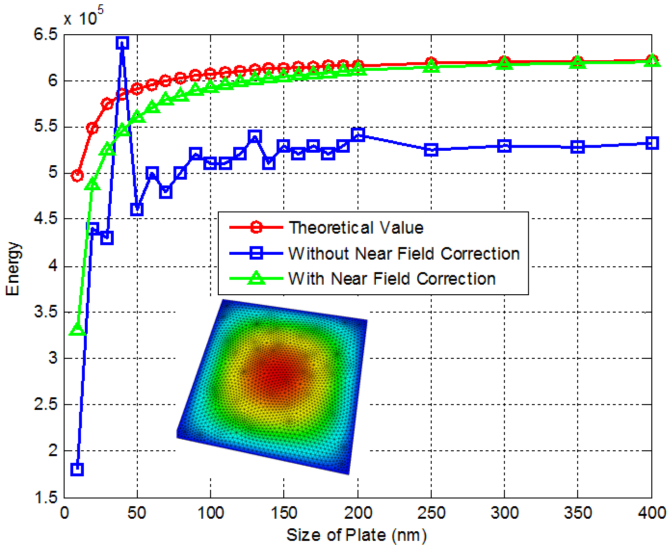

Figure 2.11: Accuracy of the proposed methods versus the mesh size. The thin plate is uniformly polarized, i.e. $\hat{\mathbf{m}} = \hat{\mathbf{z}}$.

are:

$$\begin{cases} \hat{\mathbf{n}} = \frac{(\mathbf{B}-\mathbf{A})\times(\mathbf{C}-\mathbf{B})}{|(\mathbf{B}-\mathbf{A})\times(\mathbf{C}-\mathbf{B})|}, \hat{\mathbf{s}}_1 = \frac{\mathbf{B}-\mathbf{A}}{|\mathbf{B}-\mathbf{A}|}, \hat{\mathbf{s}}_2 = \frac{\mathbf{C}-\mathbf{B}}{|\mathbf{C}-\mathbf{B}|}, \hat{\mathbf{s}}_3 = \frac{\mathbf{A}-\mathbf{C}}{|\mathbf{A}-\mathbf{C}|}, \\ \hat{\mathbf{u}}_1 = \hat{\mathbf{s}}_1 \times \hat{\mathbf{n}}, \hat{\mathbf{u}}_2 = \hat{\mathbf{s}}_2 \times \hat{\mathbf{n}}, \hat{\mathbf{u}}_3 = \hat{\mathbf{s}}_3 \times \hat{\mathbf{n}}, \\ s_1^+ = (\mathbf{B}-\mathbf{D}) \cdot \hat{\mathbf{s}}_1, s_1^- = (\mathbf{A}-\mathbf{D}) \cdot \hat{\mathbf{s}}_1, \\ s_2^+ = (\mathbf{C}-\mathbf{D}) \cdot \hat{\mathbf{s}}_2, s_2^- = (\mathbf{B}-\mathbf{D}) \cdot \hat{\mathbf{s}}_2, \\ s_3^+ = (\mathbf{A}-\mathbf{D}) \cdot \hat{\mathbf{s}}_3, s_3^- = (\mathbf{C}-\mathbf{D}) \cdot \hat{\mathbf{s}}_3, \\ h = |(\mathbf{A}-\mathbf{D}) \cdot \hat{\mathbf{n}}|, \\ d_1 = (\mathbf{A}-\mathbf{D}) \cdot \hat{\mathbf{u}}_1, d_2 = (\mathbf{B}-\mathbf{D}) \cdot \hat{\mathbf{u}}_2, d_3 = (\mathbf{C}-\mathbf{D}) \cdot \hat{\mathbf{u}}_3. \end{cases} \tag{2.40}$$

The quantities $s_i^\pm$ and d_i can be positive or negative or zero. When $s_i^\pm < 0$, the expression $s_i^\pm + \sqrt{(s_i^\pm)^2 + h^2 + d_i^2}$ may result in a big cancellation error, in this scenario it is wiser to use:

$$s_i^\pm + \sqrt{(s_i^\pm)^2 + h^2 + d_i^2} = \frac{h^2 + d_i^2}{-s_i^\pm + \sqrt{(s_i^\pm)^2 + h^2 + d_i^2}}. \tag{2.41}$$

Eq. (2.41) avoids cancellation errors and it is hence more reliable. The procedure described here is used for triangles, but it extends automatically to general planar polygons.

To further confirm the accuracy, we computed the magnetic potential and field inside a unit sphere with a magnetization distribution $\mathbf{M} = \hat{\mathbf{x}}x + \hat{\mathbf{y}}y + \hat{\mathbf{z}}z$. For a mesh of average size $0.1, 0.06, 0.04$, the error in the potential was $0.35\%, 0.12\%, 0.05\%$, and the error in the field was $2.88\%, 1.47\%, 0.87\%$, respectively.

2.5 Some examples

There are four standard micromagnetic simulation problems [79]. For problem 3, with the discretizatoin of about 20 nodes per dimension, the transition between the flower and vortex states was obtained at the cube edge length $8.5 l_{ex}$. The average magnetizaton vectors are $\langle m \rangle_y = 0.35$ in the vortex state, and $\langle m \rangle_z = 0.97$ in the flower state, which is in a good agreement with other reported results. We also ran many simulations, including reversal in magnetic particles and arrays, domain wall motion in wires or rings, magnetic write head switching, and arrays of spin transfer torque oscillators, and found the magnetization dynamics behavior correct and robust with respect to the mesh density. Next we applied FastMag into simulating magnetic recording heads, which are large and complex structures that are used in every hard drive [80]. They have many fine features and need many rounds of numerical simulations in the design process. It has a trapezoidal pole tip, a wrap-around shield, and a soft underlayer. The size is $5\mu m \times 5\mu m \times 5\mu m$.

The pole tip is tapered from a rectangular shape of 150nm × 460nm to a trapezoidal form of 60nm × 80nm × 30nm nanometers over a throat height of 150nm. The pole tip has a small uniaxial anisotropy along the cross track direction of $H_K = 1.6 \times 10^3$A/m, and $\mu_0 M_S = 1.6$T, and $A_{\text{ex}} = 1.3 \times 10^{-11}$J/m.

We used a set of four meshes, with different discretization sizes.

- M0 was a mesh in which the maximal discretization of 6nm was set on the interface surface of the pole tip/air bearing surface, on the surface around the gap in the shield, and on the surface of the soft underlayer (SUL) that is below over the shield. The rest of the surfaces and volumes had the maximal discretization of 150nm. The generated mesh was nonuniform to smoothly

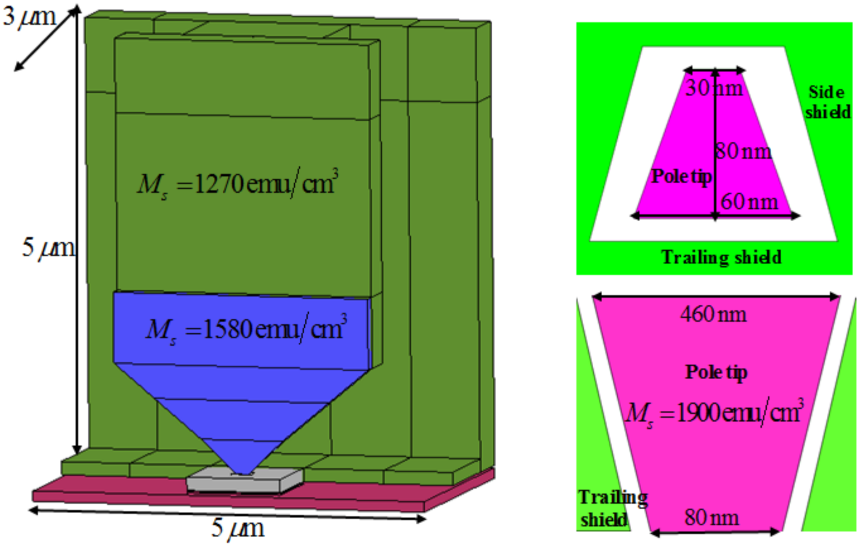

Figure 2.12: The structure of a magnetic recording head. Its dimensions are $5\mu m \times 5\mu m \times 3\mu m$. The two small figures in the right side show the shield

Table 2.1: Four meshes used in the recording head simulation.

Mesh	Number of nodes	Number of tetrahedrons
$M0$	$83K$	$283K$
$M1$	$156K$	$552K$
$M1_{NS}$	$75K$	$296K$
$M2$	$1M$	$5.3M$
$M3$	$4M$	$23M$

transition from the denser to coarser discretization where needed. This mesh was considered as a typical mesh that might be used to provide guidance for qualitative head dynamics behavior.

- M1 was a refinement of Mesh 0. The surface criteria of 6nm around the pole tip of Mesh 0 were kept. Mesh 1 had the largest element size of 12nm in the volume of the pole tip, shield, and the part of the SUL below the shield. The rest of the geometry had the largest element size of 150nm. M1 was for a writer design without shield (single pole) and the discretization was similar to M1. Meshes M1 and M1$_{NS}$ were chosen as they sometimes may be considered as adequate for obtaining the dynamic field near the pole tip.

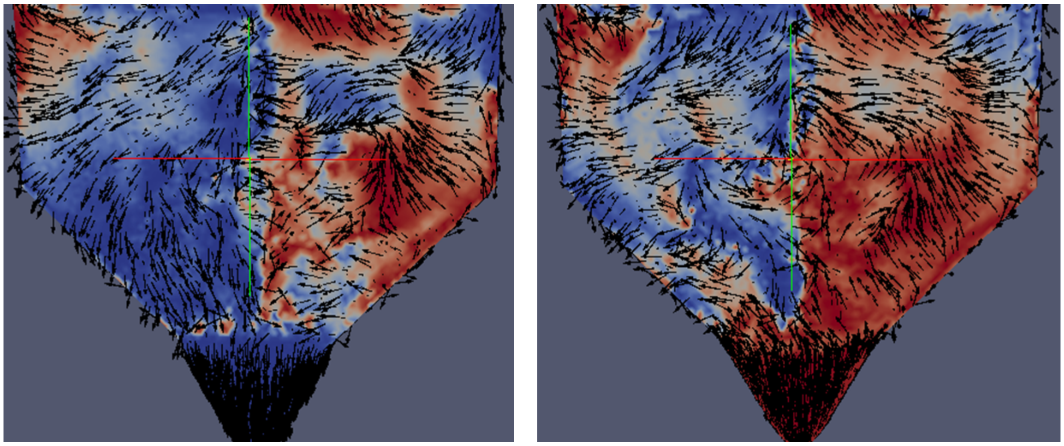

Figure 2.13: Magnetization distribution on the surface of the recording head.

- M2 had all denser parts discretized as in M1. In addition, it had the largest elements size of 24nm in the volume of the bottom part of main pole, 30nm in the volume of the top part of the main pole, and 45nm in the rest of the bulk of the head (i.e. the yoke, the return pole, and entire SUL).
- M3 had all denser parts discretized as in M1. The maximum element size used in the rest of the head was 24nm.

Using the high-performance FastMag micromagnetic simulator, we studied the magnetization and magnetic field dynamics of a realistic recording head model. The dynamics was considered as a function of the mesh density for different switching rates and current waveforms. Improper discretization may result in incorrect magnetization behavior.

2.6 Quadratic basis functions

The linear BF (LBF) is very robust, and yield very good results that have been shown in the preceding sections. However, one concern is that the exchange field may not be accurate enough. Quadratic basis functions (QBFs) are implemented for solving the LLGE via the FEM. This involves the introduction of a set of special TFs compatible with the QBFs for evaluating the Laplacian operator.

The results by using QBFs are significantly more accurate than those via linear basis functions. QBF approach leads to significantly more accurate results than conventionally used approaches based on linear basis functions. Importantly QBFs allow reducing the error of computing the exchange field by increasing the mesh density for structured and unstructured meshes. Numerical examples demonstrate the feasibility of the method.

2.6.1 Ten QBFs on a tetrahedrons

We showed that $\xi_1, \xi_2, \xi_3, \xi_4$ are four linear BFs for a tetrahedron, which are complete to $1, x, y, z$. The QBFs must be complete six more functions x^2, y^2, z^2, xy, yz, zx. So there are ten QBFs for a tetrahedron. The standard choice of these ten QBFs are:

$$\begin{aligned} &q_1 = (2\xi_1 - 1)\xi_1, q_2 = (2\xi_2 - 1)\xi_2, q_3 = (2\xi_3 - 1)\xi_3, q_4 = (2\xi_4 - 1)\xi_4, \\ &q_5 = 4\xi_1\xi_2, q_6 = 4\xi_1\xi_3, q_7 = 4\xi_1\xi_3, q_8 = 4\xi_2\xi_3, q_9 = 4\xi_2\xi_4, q_{10} = 4\xi_3\xi_4. \end{aligned} \tag{2.42}$$

The completeness of these QBFs lies in the fact that $\sum_{i=1}^{i=10} q_i = 1$. The first four BFs q_1, q_2, q_3, q_4 are associated with the original vertices of the mesh (called T1 nodes), can have negative values, the minimum value is $-\frac{1}{8}$. The other six BFs correspond to the medians of the six edges of a tetrahedron, they are referred to as T2 nodes.

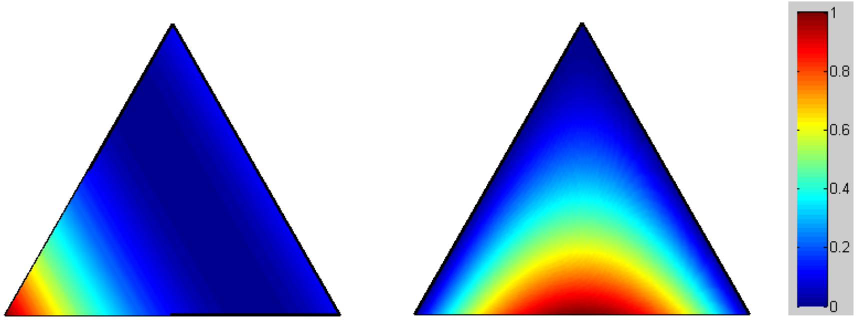

Figure 2.14: Two kinds of QBFs defined on a triangle. The first is tied to an original vertex, the second is associated with the median of an edge.

To evaluate the Laplacian, one might choose the QBFs as the TFs. This testing approach works well for non-boundary nodes. However, for the boundary nodes, a problem appears. The surface integral should be non-vanishing to enforce the boundary condition $\frac{\partial f}{\partial n} = 0$. However, for the T1 nodes located at the boundary, $\iint_{Triangle} (2\xi_i - 1)\xi_i dS = 0$ the surface integral is conducted over a boundary triangle. Therefore, there is an imbalance between T1 and T2 nodes. Physically this phenomenon should not occur and we attribute it to the improper use of testing functions in the Galerkin approach for this case. We propose a method to overcome this problem, following two guidelines in choosing a set of TFs.

- For an internal (non-boundary) node, the TF is nonzero at the point itself, and it tapers to zero at the boundary of a "box".
- The ratio of the integrals $\iint t_i dS / \iiint t_i dV$, should be the same for both types of nodes on a boundary triangle S and the corresponding tetrahedron V.

There are several candidates that can serve as testing functions. The particular set of TFs implemented here is:

$$\begin{aligned} &t_1 = \xi_1^5, t_2 = \xi_2^5, t_3 = \xi_3^5, t_4 = \xi_4^5, \\ &t_5 = (\xi_1\xi_2)^{2.5}, t_6 = (\xi_1\xi_3)^{2.5}, t_7 = (\xi_1\xi_3)^{2.5}, \\ &t_8 = (\xi_2\xi_3)^{2.5}, t_9 = (\xi_2\xi_4)^{2.5}, t_{10} = (\xi_3\xi_4)^{2.5}. \end{aligned} \tag{2.43}$$

Let i', j', k', l' be either integer or half integer[1]. When the integrand is of the form $\xi_1^{i'}\xi_2^{j'}\xi_3^{k'}\xi_4^{l'}$, formula (2.19) still holds. But the definition of factorials for half integers must be specified. Let i' be a half integer and $i = i' + \frac{1}{2}$. The factorial of the half integers is defined as [81]:

$$i'! = \left(i - \frac{1}{2}\right)! = \Gamma\left(i + \frac{1}{2}\right) = \sqrt{\pi} \prod_{j=0}^{j=i-1} \left(j + \frac{1}{2}\right), \tag{2.44}$$

$\sqrt{\pi}$ appears in Eq. (2.44) because of $\Gamma\left(\frac{1}{2}\right) = \sqrt{\pi}$. There are two reasons why these TFs are chosen. First, they are convenient to implement. Second, the numerical values of the Laplacian at the boundary nodes are consistent with the values obtained when using LBFs. The error of using the QBFs via this approach

---

[1] i' is a half integer if and only if $i' - \frac{1}{2}$ is an integer.

decreases linearly with h for unstructured meshes, and it is much smaller than that obtained when using LBFs.

When QBFs are taken, one still needs to handle the near field correction for the close point interactions. But in this case the problem is becoming even more challenging. The integrals used for QBFs are put in the appendix.

The presented higher-order accurate approach for evaluating the exchange field is verified via two examples, including a test case for the field itself and a solution of a micromagnetic problem. The first example is to test the approach by computing a given function with known Laplacian. Specifically, the following function is chosen $f = e^{x^2+y-2z^2}$, with $\nabla^2 f = (4x^2 - 1 + 4z^2)e^{x^2+y-2z^2}$. A cube with a dimension of $1 \times 1 \times 1$ is considered, with structured and unstructured meshes of different density. For structured meshes both LBF and QBF approaches yield $error = \mathcal{O}(h^2)$. On the other hand for unstructured meshes, much higher errors are obtained for LBFs and this error does not scale with h, indicating error $error = \mathcal{O}(1)$. QBFs on the other hand lead to a low error, with $error = \mathcal{O}(h)$ for unstructured mesh. Similar behavior is observed for many arbitrary structures and functions using unstructured meshes. These results are shown in Fig. 2.15. Next, the accuracy of the presented QBF approach is tested with a complete LLG solver, which is a higher-order extension of the FastMag micromagnetic simulator. We consider a rectangular domain, with a dimension of $100\text{nm} \times 10\text{nm} \times 10\text{nm}$ with the following parameters $H_K = 0, M_S = 5 \times 10^5\text{A/m}, l_{ex} = 8\text{nm}, \alpha = 0.2$. The initial state of the magnetization is $\hat{\mathbf{m}} = \hat{\mathbf{z}}$, an external field of $\mathbf{H}_{\text{app}} = (-\hat{\mathbf{x}}100 - \hat{\mathbf{z}}1000)\frac{\text{A}}{\text{m}}$ is applied to the region $0 \leq x \leq 10\text{nm}$ to reverse the magnetization. The average values of the x-component of the magnetization components $\langle m \rangle_x$ is compared for structure and unstructured meshes with LBFs and QBFs. To demonstrate effects of the exchange field the solutions were obtained without the magnetostatic field. The unstructured mesh for QBFs (Mesh M1) has 331 vertices and 1339 tetrahedrons. To make fair comparisons between LBFs and QBFs, each tetrahedron of $M1$ is divided into 8 smaller tetrahedrons, by adding medians of edges of M1 to the mesh. Then the unstructured mesh for the LBFs (Mesh M2) has 2145 vertices and 10712 tetrahedrons. We also show the results of LBFs with M1. From Fig. 2.16,

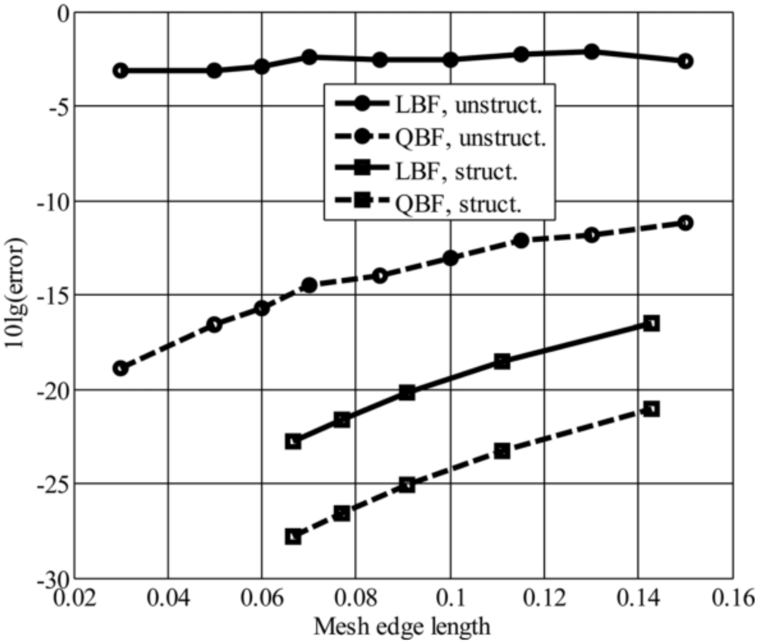

Figure 2.15: Root-Mean-Square (RMS) error in the numerical evaluation of Laplacian operator using LBFs and QBFs, over structured and unstructured meshes of different edge lengths.

clear discrepancies in the dynamic behavior are observed, which are due to the differences in the exchange field.

2.7 Conclusion

This chapter has presented the algorithms in FastMag, a fast micromagnetic simulator for solving the LLG equation. FastMag discretizes a general computational domain into tetrahedral elements. The differential operators are calculated similar to conventional FEM method. The magnetostatic field is computed by superposition principles in the computational domain parts. Efficient quadrature rules and analytical integration for overlapping elements with a singular integral kernel are used to discretize the superposition integral. The discretized integrals are computed using precorrected FFT with the computational complexity of $\mathcal{O}(N \ln(N))$. The simulator is implemented on GPUs, which offer massive paral-

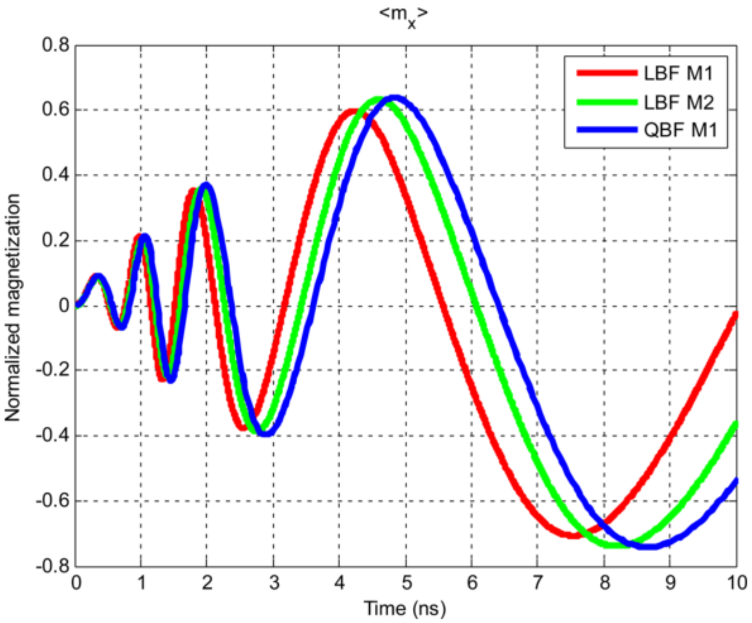

Figure 2.16: Comparisons in the $\langle m \rangle_x$ for dynamic magnetization in a rod for LBFs with M1 and M2 and for QBFs with M1.

lelization at a low cost, converting a simple desktop to a powerful machine matching performance of a CPU cluster.

Acknowledgements: Chapter 2, in part, is based on four journal articles:

(1) R. Chang, S. Li, M. V. Lubarda, B. Livshitz, V. Lomakin, "FastMag: Fast micromagnetic solver for large-scale simulations," Journal of Applied Physics 109, 07D358 (2011). (2) M. V. Lubarda, S. Li, R. Chang, M. A. Escobar, E. E. Fullerton, V. Lomakin, "Domain wall motion in magnetically frustrated nanorings," Physical Review B. vol. 85, 214428, 2012. (3) R. Chang, S. Li, M. A. Escobar, M. V. Lubarda, and V. Lomakin, "Accurate evaluation of exchange fields in finite element micromagnetic solvers," Journal Appl. Phys., vol. 111, p.07D129, 2012. (4) M. A. Escobar, M. V. Lubarda, S. Li, R. Chang, B. Livshitz, and V. Lomakin, "Micromagnetic analysis of write head dynamics using FastMag," IEEE Trans. Magn., vol. 48, no. 5, May 2012. The dissertation author was the contributing author to these articles.

Chapter 3

Jacobian vector product methods

The Landau-Lifshitz-Gilbert equation (LLGE) describes the temporal evolution of the magnetization. It is posed as an initial value problem. Given an initial state at time $t = 0$, one wants to see what the magnetization behaves in a later time $t = t_{out}$. Therefore, the time integration is an important topic for numerical solution of LLGE. An efficient method is introduced that enables analytical calculations of Jacobian vector products (JVPs) in the context of a Jacobian-free Newton-Krylov (JFNK) framework [82, 83] for solving the nonlinear equations that arise from the LLGE, which is nonlinear in nature. For example, to obtain the steady state of a magnetic system, one has to solve an equation:

$$\mathbf{M} \times \left[\mathbf{H}_{\text{app}} + l_{\text{ex}}^2 \mathbf{M} + \frac{H_K}{M_S}(\mathbf{M} \cdot \hat{\mathbf{k}})\hat{\mathbf{k}} + \nabla\nabla \cdot \iiint_{\Omega} \frac{\mathbf{M}(\mathbf{r}')}{4\pi|\mathbf{r}' - \mathbf{r}|} d\mathbf{r}' \right] = \mathbf{0}. \tag{3.1}$$

Such an equation is quadratic in terms of $\mathbf{M}$. The discretization of Eq. (3.1) gives rise to a large number of coupled equations, which are very challenging. The general idea is to use Newton methods.

3.1 Newton methods

The Newton method was first developed for one-variable nonlinear equation of the form $f(x) = 0, x \in \mathcal{R}$, whose solution has no simple closed form. The function $f(x)$ is assumed to be smooth. Let x^* be the "exact" solution. In an iterative process, we starts from an initial guess x_0, and suppose we have a solution

x_n. To get the next value x_{n+1}, one approximates the derivative by using a first order finite difference (FD):

$$f(x_{n+1}) = f(x_n) + f'(x_n)(x_{n+1} - x_n) + \text{higher order terms}. \tag{3.2}$$

It is expected that $0 \approx |f(x_{n+1})| < |f(x_n)|$, and we simply omit the higher order terms to obtain:

$$x_{n+1} = x_n - \frac{f(x_n)}{f'(x_n)}. \tag{3.3}$$

The processed is iterated and it is terminated when $|f(x_{n+1})| < \epsilon$, where ϵ is a prescribed accuracy level. One of the key steps in the Newton methods is to calculate the derivative of $f(x)$, which is a scalar function for one-variable functions. The Newton method is extendable to a multivariable system without major modifications. However, the concept of "derivative" must be modified. Consider a system of N coupled nonlinear equations:

$$\mathbf{F}(\mathbf{x}) = \begin{bmatrix} F_1(x_1, x_2, \ldots, x_N) \\ F_2(x_1, x_2, \ldots, x_N) \\ \vdots \\ F_N(x_1, x_2, \ldots, x_N) \end{bmatrix} = \mathbf{0}, \tag{3.4}$$

where $\mathbf{F}, \mathbf{x}, \mathbf{0} \in \mathcal{R}^N$. The first order "derivative" is a Jacobian matrix $\mathbb{J}$:

$$\mathbb{J} = \begin{bmatrix} \frac{\partial F_1}{\partial x_1} & \frac{\partial F_1}{\partial x_2} & \cdots & \frac{\partial F_1}{\partial x_N} \\ \frac{\partial F_2}{\partial x_1} & \frac{\partial F_2}{\partial x_2} & \cdots & \frac{\partial F_2}{\partial x_N} \\ \vdots & \vdots & \ddots & \vdots \\ \frac{\partial F_N}{\partial x_1} & \frac{\partial F_N}{\partial x_2} & \cdots & \frac{\partial F_N}{\partial x_N} \end{bmatrix}. \tag{3.5}$$

With $\mathbb{J}$, the iteration format of this multi-variable system becomes:

$$\mathbf{x}_{n+1} = \mathbf{x}_n - [\mathbb{J}(\mathbf{x}_n)]^{-1}\mathbf{F}(\mathbf{x}_n), \tag{3.6}$$

where $[\mathbb{J}(\mathbf{x}_n)]^{-1}$ is the inverse of $\mathbb{J}(\mathbf{x}_n)$. Let $\Delta x_n = \mathbf{x}_n - \mathbf{x}_{n+1}$, Eq. (3.6) is equivalent to solve a linear equation:

$$\mathbb{J}(\mathbf{x}_n)\Delta\mathbf{x}_n = \mathbf{F}(\mathbf{x}_n). \tag{3.7}$$

In this way, we have converted the original intractable nonlinear equations into a series of linear system problems. Before solving Eq. (3.7), one must know how to represent the matrix $\mathbb{J}(\mathbf{x}_n)$. Evaluation of $\mathbf{F}(\mathbf{x}_n)$ requires an $\mathcal{O}(N)$ memory space and an $\mathcal{O}(N\log N)$ complexity. It is expected that $\mathbb{J}(\mathbf{x}_0)$ should cost no more. Henceforth, one should not compute $\mathbf{J}(\mathbf{x}_n)$ elementwise since it would cost $\mathcal{O}(N^2)$ time if $\mathbb{J}(\mathbf{x}_n)$ is a dense matrix. If $\mathbb{J}(\mathbf{x}_0)$ is a sparse matrix with only $\mathcal{O}(N)$ nonzero elements.

Here is a simple example. Let $F_1(x_1,x_2) = x_1x_2 + x_2^2 - 0.1 = 0, F_2(x_1,x_2) = x_1^2 + 3x_2^2 - 0.4 = 0, (x_1, x_2 > 0)$. The Jacobian is $\mathbb{J} = \left(\begin{smallmatrix} x_2 & x_1+2x_2 \\ 2x_1 & 6x_2 \end{smallmatrix}\right)$. The exact solution is $\mathbf{x}_{exact} = (x_1,x_2)^T = \left(\frac{2+\sqrt{5}}{5+\sqrt{5}}, \frac{1}{5+\sqrt{5}}\right)^T = (0.5854, 0.1382)^T$. Starting from the initial guess $x_1 = 0.2, x_2 = 0.3$, the Newton method reaches $\mathbf{x}_4 = (0.5859, 0.1380)^T$ in just a 4 iterations such that $\frac{|\mathbf{x}_4 - \mathbf{x}_{exact}|}{|\mathbf{x}_{exact}|} < 10^{-3}$.

3.2 Krylov methods

As is mentioned in the first chapter, it is hard to solve a large linear matrix problem. Iterative methods are a common option. They are projection methods for solving $\mathbb{A}\boldsymbol{x} = \boldsymbol{b}$ using the Krylov subspace:

$$\mathcal{K}_m(\mathbb{A}, \boldsymbol{b}) = span(\boldsymbol{b}, \mathbb{A}\boldsymbol{b}, \mathbb{A}^2\boldsymbol{b}, \ldots, \mathbb{A}^{m-1}\boldsymbol{b}), \tag{3.8}$$

where $\mathbb{A} \in \mathcal{R}^{N\times N}$ is a matrix, $\boldsymbol{x}, \boldsymbol{b} \in \mathcal{R}^N$ are column vectors. The Krylov-based methods only need matrix-vector products in the iterations. Therefore, the Krylov methods can be "free" from any matrices. Most widely used Krylov solvers include generalized minimal residual method (GMRES), Transpose-free quasi-minimal residual(TFQMR), Biconjugate gradient stabilized (BiCGstab), etc. The iterative solvers only requires a "black box" function, which takes an input column vector $\boldsymbol{y}$, and outputs a column vector $\boldsymbol{z}$. This function implements $\boldsymbol{z} = \mathbb{A}\boldsymbol{y}$ internally and implicitly.

GMRES approaches the exact solution of $\mathbb{A}\boldsymbol{x} = \boldsymbol{b}$ by the vector $\boldsymbol{x}_n$ that minimizes the Euclidean norm of the residual $\boldsymbol{r}_n = \mathbb{A}\boldsymbol{x}_n - \boldsymbol{b}$. The vectors $\boldsymbol{b}, \mathbb{A}\boldsymbol{b}, \ldots, \mathbb{A}\boldsymbol{b}^{m-1}$ in $\mathcal{K}_m(\mathbb{A}, \boldsymbol{b})$ are almost linearly dependent. Consequently, they should not be taken as basis vectors. Instead, an Arnoldi iteration is applied to orthogonalize the vectors: $\boldsymbol{q}_0, \boldsymbol{q}_1, \ldots, \boldsymbol{q}_{m-1}$. The GREMS solver then minimizes the residual errors in the subspaces spanned by the orthogonalized vectors.

3.3 Time integration for LLGE

The Landau-Lifshitz-Gilbert equation (LLGE) models dynamical magnetization phenomena in micro- and nano-meter scales. For its predictive power, solutions of LLGE provide detailed (otherwise unavailable) information for the analysis, design of a variety of magnetic devices such as magnetic write/read heads, bit patterned media, spin-transfer torque (STT) [84] magnetic random access memories (MRAMs). For example, obtaining hysteresis loops of nanoparticles is a simple application of LLGE. As a time domain (TD) partial differential equation (PDE), the LLGE describes the dynamics of magnetization as a result of competing forces between applied field, anisotropic field, demagnetization field and exchange field. Unfortunately, due to the presence of the last two fields and its high nonlinearity, LLGE cannot be solved analytically even for very simple geometric structures such as cubes and spheres. Therefore, numerical methods are unavoidably demanded. A set of arbitrary ODEs with N equations take a form

$$\dot{\mathbf{y}} := \frac{d\mathbf{y}}{dt} = \mathbf{f}(\mathbf{y}, t). \tag{3.9}$$

where $\mathbf{y}$ is a column vector, representing a set of N variables. $\mathbf{f}$ denotes N functions. Eq. (3.9) is the most general form of a system of ODEs. For example, in LLGE, $\mathbf{y}$ can be the magnetization vector.

After the $\mathbf{H}_{\text{eff}}$ has been computed by applying the FEM, the LLGE is cast into an ODE problem, provided by an initial condition. Numerical methods for solving initial value problems (IVPs) typically fall into two classes: linear multistep methods, or Runge-Kutta methods. The methods can also be divided as either explicit or implicit. Explicit methods in the category of linear multistep methods include Adams-Bashforth methods. For instance, we can have implicit linear multistep methods, and backward differentiation formulas (BDFs), and many types of implicit Runge-Kutta methods. A rule of thumb states that *stiff* ODEs require implicit methods, whereas *non-stiff* problems could be solved more efficiently with explicit methods.

For simplicity, we use a linear sequence of time $t_n = t_0 + nh$, where t_0 is the starting time, h is the time step.

3.3.1 Explicit methods

In the explicit methods, $\mathbf{y}$ is updated by its previous values, using only RHS evaluations. For instance, the Euler method approximates the derivative by a forward difference:

$$\dot{\mathbf{y}}(t) \approx \frac{\mathbf{y}(t+h) - \mathbf{y}(t)}{h}, \tag{3.10}$$

which follows:

$$\mathbf{y}(t+h) \approx \mathbf{y}(t) + h\mathbf{f}(\mathbf{y}(t), t). \tag{3.11}$$

Eq. (3.11) is usually applied recursively at the discrete time steps to yield:

$$\mathbf{y}_{n+1} = \mathbf{y}_n + h\mathbf{f}(\mathbf{y}_n, t_n). \tag{3.12}$$

It is seen that the explicit methods employ the previous information of $\mathbf{y}$ to get its value at future steps. The cost in the addition and multiplication in Eq. (3.12) is negligible, the dominant cost is the evaluation of RHS. However, this approach becomes less stable when the problem is *stiff*.

3.3.2 Stiffness of ODEs

The term *stiffness* has been mentioned multiple times. But what is exactly *stiffness*? There exists no simple or general definition. Roughly speaking, an ODE is *stiff* if the solution being sought is varying slowly, but there are close solutions that vary quickly. For simplicity, consider a linear constant coefficient inhomogeneous system:

$$\dot{\mathbf{y}} = \mathbb{A}\mathbf{y} + \mathbf{e}(t). \tag{3.13}$$

where $\mathbb{A} \in \mathbb{R}^{N\times N}$, $\mathbf{e}(t) \in \mathbb{R}^N$ is an excitation vector. Let $\lambda_i, 1 \leq i \leq N$ be the eigenvalues of $\mathbb{A}$. λ_i determines the eigen modes of the solutions in $\mathbf{y}$. For a physical problem, $\Re(\lambda_i) \leq 0$, otherwise the system would be unstable. If $|\Re(\lambda_i)|$ is large, then the mode $\exp(\lambda_i t)$ decays quickly. Otherwise, the decay is slow. A stiffness ratio can be defined as:

$$SR = \frac{|\Re(\overline{\lambda})|}{|\Re(\underline{\lambda})|}, \tag{3.14}$$

where $|\Re(\underline{\lambda})| \leq |\Re(\lambda_i)| \leq |\Re(\overline{\lambda})|$. The stiffness is related to the differences between the eigen modes with the fastest and slowest decay.

The real problems, the matrix size is large and it has many eigenvalues. It is inevitable to have a large stiffness. Especially, the Jacobian matrix from FEM discretization of the LLGE is stiff.

3.3.3 Implicit methods

The presented analytic Jacobian vector product (AJVP) methods are geared to avoid explicitly forming the fully-populated Jacobian matrices, thus achieving a low memory cost. The AJVP method is based on the definition of a linear operator $\mathcal{L}$, which is a dense matrix. Employing $\mathcal{L}$, the AJVP needs only a single evaluation of the right-hand side and cross product operations with an $\mathcal{O}(N)$ or $\mathcal{O}(N \log N)$ (N is the degrees of freedom) complexity if fast algorithms (e.g. fast Fourier transform, fast multipole method) are used to compute the magnetostatic field. AJVP makes more accurate, reliable and faster evaluations of matrix vector products in iterative linear solvers. The performance of the proposed AJVP was demonstrated in our finite element-based micromagnetic simulator FastMag. Examples show that AJVPs used in backwards differentiation formulas provide much larger time steps than do explicit methods. By using FastMag, numerical simulations of recording head systems discretized into 4 million tetrahedral elements verified the effectiveness of the AJVP methods.

Explicit methods in principle can handle stiff problem, at a very slow speed. To overcome this problem, implicit methods should be adopted. A simple example of implicit method is backward Euler method:

$$\dot{\mathbf{y}}(t+h) \approx \frac{\mathbf{y}(t+h) - \mathbf{y}(t)}{h}, \tag{3.15}$$

which has discrete the form:

$$\mathbf{y}_{n+1} = \mathbf{y}_n + h\mathbf{f}(\mathbf{y}_{n+1}, t_{n+1}). \tag{3.16}$$

Since $\mathbf{y}_{n+1}$ appears in both sides of Eq. (3.16), it has to be solved. Thus solving a system of equations is a typical requirement for implicit methods.

If $\mathbf{f}$ is a nonlinear function of $\mathbf{y}$, then solutions to Eq. (3.16) become quite complicated. It is at this point that the Newton methods should be used. The first one to *linearize* the nonlinear problem. Eq. (3.16) can be linearized as:

$$\underbrace{[\mathbb{I} - h\mathbb{J}(\mathbf{y}^m_{n+1})]}_{\mathbb{A}}\underbrace{(\mathbf{y}^{m+1}_{n+1} - \mathbf{y}^m_{n+1})}_{\boldsymbol{x}} = \underbrace{-\mathbf{y}^m_{n+1} - h\mathbf{f}(\mathbf{y}^m_{n+1}, t_{n+1}) + \mathbf{y}_n}_{\boldsymbol{b}}. \tag{3.17}$$

where $\mathbf{y}^m_{n+1}$ is the known result in the $m-$th iteration for $\mathbf{y}_{n+1}$ in the nonlinear iterations. The unknown is $\mathbf{y}^{m+1}_{n+1}$, which requires the solutions to Eq. (3.17), which is a linear equation. Let $\mathbb{A} = \mathbb{I} - h\mathbb{J}(\mathbf{y}^m_{n+1})$, $\boldsymbol{x} = \mathbf{y}^{m+1}_{n+1} - \mathbf{y}^m_{n+1}$, $\boldsymbol{b} = -\mathbf{y}^m_{n+1} - h\mathbf{f}(\mathbf{y}^m_{n+1}, t_{n+1}) + \mathbf{y}_n$. Then the linear equation is $\mathbb{A}\boldsymbol{x} = \boldsymbol{b}$.

3.4 Jacobian free Newton Krylov

In a Krylov solver for Eq. (3.17), one needs to provide Jacobian vector products (JVPs):

$$\boldsymbol{u} = \mathbb{A}\boldsymbol{v} = \boldsymbol{v} - h\mathbb{J}(\mathbf{y}^m_{n+1}) \cdot \boldsymbol{v}, \tag{3.18}$$

where $\boldsymbol{u}, \boldsymbol{v}$ are column vectors. The naïve definition of JVP takes $\mathcal{O}(N^2)$ operations, which is too prohibitive and as a result it is rarely used and an alternative method is used instead:

$$\mathbf{u} = \lim_{\delta \to 0} \frac{\mathbf{f}(\mathbf{y} + \delta\mathbf{v}, t) - \mathbf{f}(\mathbf{y}, t)}{\delta}, \tag{3.19}$$

where δ is a real parameter. One can simply use a forward finite difference based on formula (3.19):

$$\mathbf{u} \approx \frac{\mathbf{f}(\mathbf{y} + \delta\mathbf{v}, t) - \mathbf{f}(\mathbf{y}, t)}{\delta}, \tag{3.20}$$

alternatively, the central difference method can also be used:

$$\mathbf{u} \approx \frac{\mathbf{f}(\mathbf{y} + \delta\mathbf{v}, t) - \mathbf{f}(\mathbf{y} - \delta\mathbf{v}, t)}{2\delta}, \tag{3.21}$$

where δ is a carefully chosen constant. It cannot be too large since it should approach zero; it cannot be too small either, otherwise the substraction in Eq. (3.20) causes a very big error. There has been many papers [82] that discussed how to choose δ to make the solution accurate and fast.

In LLGE, $\mathbf{y} = \mathbf{m}^1$, and $\mathbf{f}(\mathbf{y}, t) = -\frac{1}{1+\alpha^2}\left[\mathbf{m} \times \mathbf{H}_{\text{eff}} + \alpha \mathbf{m} \times (\mathbf{m} \times \mathbf{H}_{\text{eff}})\right]$. $\mathbf{H}_{\text{eff}}$ is a linear operator times $\mathbf{m}$ plus an applied field $\mathbf{H}_{\text{app}}$, i.e.

$$\mathbf{H}_{\text{eff}} = \mathcal{L}\mathbf{m} + \mathbf{H}_{\text{app}}, \tag{3.22}$$

where the linear operator $\mathcal{L}$ is

$$\left[\mathcal{L}(\mathbf{m})\right](\mathbf{r}) = H_K(\hat{\mathbf{k}} \cdot \mathbf{m})\hat{\mathbf{k}} + M_S l_{ex}^2 \nabla^2 \mathbf{m} + M_S \nabla \iiint_\Omega \nabla' \frac{1}{4\pi|\mathbf{r} - \mathbf{r}'|} \cdot \mathbf{m}(\mathbf{r}') d\mathbf{r}'. \tag{3.23}$$

The function $\mathbf{f}(\mathbf{m}, t)$ is nonlinear, but it is the product and summation of linear operators. The linear operator $\mathcal{L}$ is an important abstraction of the effective field in the computations, which plays a major role in the analytic approach. Any linear operator has two fundamental properties:

$$\begin{aligned} &\mathcal{L}(\mathbf{u} + \mathbf{v}) = \mathcal{L}(\mathbf{u}) + \mathcal{L}(\mathbf{v}), \\ &\mathcal{L}(a\mathbf{u}) = a\mathcal{L}(\mathbf{u}), \end{aligned} \tag{3.24}$$

where a is a real constant, $\mathbf{u}, \mathbf{v}$ are arbitrary vectors.

3.4.1 JVP for the precessional torque

The precessional torque in the LLGE is:

$$\mathbf{T}_{\text{p}}(\mathbf{m}) := \mathbf{m} \times \left[\mathcal{L}(\mathbf{m}) + \mathbf{H}_{\text{app}}\right]. \tag{3.25}$$

According to Eq. (3.19), the corresponding JVP is

$$\mathbb{J}_{\text{p}}(\mathbf{m}) \cdot \mathbf{v} = \lim_{\delta \to 0} \frac{(\mathbf{m} + \delta\mathbf{v}) \times \left[\mathcal{L}(\mathbf{m} + \delta\mathbf{v}) + \mathbf{H}_{\text{app}}\right] - \mathbf{m} \times \left[\mathcal{L}(\mathbf{m}) + \mathbf{H}_{\text{app}}\right]}{\delta}. \tag{3.26}$$

The numerator of Eq. (3.26) is quadratic in terms of δ, is expanded:

$$\begin{aligned} &(\mathbf{m} + \delta\mathbf{v}) \times \left[\mathcal{L}(\mathbf{m} + \delta\mathbf{v}) + \mathbf{H}_{\text{app}}\right] - \mathbf{m} \times \left[\mathcal{L}(\mathbf{m}) + \mathbf{H}_{\text{app}}\right] \\ =&\delta\left[\mathbf{v} \times \mathbf{H}_{\text{eff}}(\mathbf{m}) + \mathbf{m} \times \mathcal{L}\mathbf{v}\right] + \delta^2 \mathbf{v} \times \mathcal{L}\mathbf{v}. \end{aligned} \tag{3.27}$$

Inserting Eq. (3.27) into Eq. (3.26), one immediately has:

$$\mathbb{J}_{\text{p}}(\mathbf{m}) \cdot \mathbf{v} = \mathbf{v} \times \mathbf{H}_{\text{eff}}(\mathbf{m}) + \mathbf{m} \times \mathcal{L}\mathbf{v}. \tag{3.28}$$

---

[1] Here we do not use $\hat{\mathbf{m}}$ since in the time integration, the $\mathbf{m}$ cannot be kept as a unit vector. Moreover, the results of this chapter are not dependent on whether it is unitary or not.

Eq. (3.28) shows that the JVP depends on $\mathbf{m}$, since the Jacobian matrix is not a constant. This result is no surprising, since the precessional torque is intrinsically a quadratic functional of $\mathbf{m}$. The differentiation operation in the Jacobian matrix reduces the power of $\mathbf{m}$.

3.4.2 JVP for the damping torque

The damping torques in the LLGE reads:

$$\mathbf{T}_{\mathrm{d}}(\mathbf{m}) := \mathbf{m} \times \mathbf{m} \times [\mathcal{L}(\mathbf{m}) + \mathbf{H}_{\mathrm{a}}] \,. \tag{3.29}$$

The corresponding JVP is

$$\begin{aligned} &\mathbb{J}_{\mathrm{d}}(\mathbf{m}) \cdot \mathbf{v} \\ =& \lim_{\delta \to 0} \frac{(\mathbf{m} + \delta\mathbf{v}) \times (\mathbf{m} + \delta\mathbf{v}) \times [\mathcal{L}(\mathbf{u} + \delta\mathbf{v}) + \mathbf{H}_{\mathrm{app}}] - \mathbf{m} \times \mathbf{m} \times [\mathcal{L}(\mathbf{m}) + \mathbf{H}_{\mathrm{app}}]}{\delta}. \end{aligned} \tag{3.30}$$

The numerator in Eq. (3.30) is expanded in terms of polynomials of δ:

$$\begin{aligned} &(\mathbf{m} + \delta\mathbf{v}) \times (\mathbf{m} + \delta\mathbf{v}) \times [\mathcal{L}(\mathbf{m} + \delta\mathbf{v}) + \mathbf{H}_{\mathrm{app}}] - \mathbf{m} \times \mathbf{m} \times [\mathcal{L}(\mathbf{m}) + \mathbf{H}_{\mathrm{app}}] \\ =&\delta \left[\mathbf{m} \times \mathbf{v} \times \mathbf{H}_{\mathrm{eff}}(\mathbf{m}) + \mathbf{v} \times \mathbf{m} \times \mathbf{H}_{\mathrm{eff}}(\mathbf{m}) + \mathbf{m} \times \hat{\mathbf{m}} \times \mathcal{L}\mathbf{v}\right] + \\ &\delta^2 \left[\mathbf{v} \times \mathbf{v} \times \mathbf{H}_{\mathrm{eff}}(\mathbf{m}) + \mathbf{m} \times \mathbf{v} \times \mathcal{L}\mathbf{v} + \mathbf{v} \times \mathbf{m} \times \mathcal{L}\mathbf{v}\right] + \\ &\delta^3 \mathbf{v} \times \mathbf{v} \times \mathcal{L}\mathbf{v}. \end{aligned} \tag{3.31}$$

Inserting Eq. (3.31) into Eq. (3.30) gives the AJVP:

$$\mathbb{J}_{\mathrm{d}}(\mathbf{m}) \cdot \mathbf{v} = \mathbf{m} \times \mathbf{v} \times \mathbf{H}_{\mathrm{eff}}(\hat{\mathbf{m}}) + \mathbf{v} \times \mathbf{m} \times \mathbf{H}_{\mathrm{eff}}(\hat{\mathbf{m}}) + \mathbf{m} \times \mathbf{m} \times \mathcal{L}\mathbf{v}. \tag{3.32}$$

There are three terms, this because the damping torque is a cubic functional of $\mathbf{m}$. Assume that we have known $\mathbb{J}_{\mathrm{p}}$, then Eq. (3.32) becomes:

$$\mathbb{J}_{\mathrm{d}}(\mathbf{m}) \cdot \mathbf{v} = \mathbf{m} \times [\mathbb{J}_{\mathrm{p}} \cdot \mathbf{v}] + \mathbf{v} \times \mathbf{m} \times \mathbf{H}_{\mathrm{eff}}(\mathbf{m}). \tag{3.33}$$

The result Eq. (3.32) is quadratic in terms of $\mathbf{m}$, since the Jacobian matrix $\mathbb{J}_{\mathrm{p}}$ is actually a quadratic form. To further reduce the computational cost, Eq. (3.32) utilizes $\mathbb{J}_{\mathrm{p}}(\mathbf{m}) \cdot \mathbf{v}$, which is already known. The JVP of the classical LLGE thus has 5 terms in total.

3.4.3 JVP for the STT

In the presence of an impressed current density $\mathbf{j}$ that passes through a magnetic film, there is an induced spin-transfer torque (STT), which changes the states of $\hat{\mathbf{m}}$, which are:

$$\begin{aligned}\mathbf{T}_1(\mathbf{m}) &= \mathbf{m} \times \mathbf{j} \cdot \nabla \mathbf{m}. \\ \mathbf{T}_2(\mathbf{m}) &= \mathbf{m} \times (\mathbf{m} \times \mathbf{j} \cdot \nabla \mathbf{m}).\end{aligned} \tag{3.34}$$

The JVPs for these two parts take the form:

$$\begin{aligned}\mathbb{J}_{\mathbf{T}1} \cdot \mathbf{v} &= \mathbf{v} \times (\mathbf{j} \cdot \nabla \mathbf{m}) + \mathbf{m} \times (\mathbf{j} \cdot \nabla \mathbf{v}). \\ \mathbb{J}_{\mathbf{T}2} \cdot \mathbf{v} &= \mathbf{v} \times (\mathbf{m} \times \mathbf{j} \cdot \nabla \mathbf{m}) + \mathbf{m} \times (\mathbf{v} \times \mathbf{j} \cdot \nabla \mathbf{m}) + \mathbf{m} \times (\mathbf{m} \times \mathbf{j} \cdot \nabla \mathbf{v}).\end{aligned} \tag{3.35}$$

From Eq. (3.35), one has $\mathbb{J}_{\mathbf{T}2} \cdot \mathbf{v} = \mathbf{m} \times (\mathbb{J}_{\mathbf{T}1} \cdot \mathbf{v}) + \mathbf{v} \times (\mathbf{m} \times \mathbf{j} \cdot \nabla \mathbf{m})$. Similar to the precessional and damping torques, these two torques are also quadratic and cubic, respectively. The resulting JVP also contains 5 terms.

3.5 JVPs for differential algebraic equations

The LLGE has multiple forms. One of the popular forms is a differential algebraic equation:

$$\mathbf{F}(t, \mathbf{m}, \dot{\mathbf{m}}) = \dot{\mathbf{m}} + \mathbf{m} \times [\gamma \mathbf{H}_{\text{eff}}(\mathbf{m}) - \alpha \dot{\mathbf{m}}] = \mathbf{0}. \tag{3.36}$$

In this implicit equation, $\mathbf{F}(t, \mathbf{m}, \dot{\mathbf{m}})$ is still nonlinear in terms of $\mathbf{m}$. But the nonlinearity is only quadratic, which is simpler than the explicit form. Moreover, this equation is linear in terms of $\dot{\mathbf{m}}$. Here we need two kinds of AJVP:

$$\mathbb{J}_{\mathbf{m}} \cdot \mathbf{v} = \frac{\partial \mathbf{F}}{\partial \mathbf{m}} \cdot \mathbf{v} = \mathbf{v} \times (\gamma \mathbf{H}_{\text{eff}} - \alpha \dot{\mathbf{m}}) + \mathbf{m} \times \mathcal{L}(\mathbf{v}), \tag{3.37}$$

$$\mathbb{J}_{\dot{\mathbf{m}}} \cdot \mathbf{v} = \frac{\partial \mathbf{F}}{\partial \dot{\mathbf{m}}} \cdot \mathbf{v} = \mathbf{v} - \mathbf{m} \times \alpha \mathbf{v}. \tag{3.38}$$

These two formulas are used in IDA solvers. It was found that the IDA and the CVODE solvers give rise to the same time stepping results. For this reason, the IDA solver is not indispensable for the LLGE.

Table 3.1: Information for the meshes

Mesh	M1	M2	M3	M4	M5
Discretization	30	15	10	7.5	6
No. tets	2021	15490	50087	95747	188887
No. vertices	631	3678	10808	20112	38085
No. time steps(1)	4640	8133	11266	18488	23123
CPU time(1)	20	98	627	2459	9961
No. time steps(2)	2559	3675	5245	5139	4229
CPU time(2)	26	115	691	1038	2387

3.6 Examples

The proposed AJVP approach has been applied extensively in FastMag. The correctness and efficiency of the AJVP was used in the simulation of complex recording heads. In this section we present some simpler examples. A thin magnetic film of dimensions 30nm × 300nm × 600nm is considered. We use five sets of meshes, M1, M2, M3, M4 and M5. The corresponding discretization h ranges from 30nm to 6nm. In this simulation, $l_{ex} = 10\text{nm}, M_S = 10^6 \frac{\text{A}}{\text{m}}$, there is no anistropic or applied field. A damping constant $\alpha = 0.2$ was assumed. The simulations were terminated at $t_{end} = 10\text{ns}$. We list the timings of three methods: (1) explicit method, (2) implicit method with approximate Jacobian, and (3) implicit method with JVP. The initial magnetization state is $\frac{1}{\sqrt{3}}(1, 1, 1)$. Table 3.1 infers that the total CPU time of JVP is larger than total CPU time of explicit (t_{exp}) method when N is smaller than 11 thousand. In these cases, h is larger than l_{ex}, and the resulting ODEs are not stiff. The JVP does not derive benefits. However, as h becomes smaller than l_{ex}, t_{exp} grows approximately quadratically with N, however, JAP increases only linearly. Consequently, the JVP can significantly. Fig. 3.1 compares the average magnetization vector between the results from two the explicit method and the JVP. There are no observable differences between them. This validates the correctness of the proposed procedures.

We can see the timing results in Table 3.1. The explicit requires a fast increasing number of time steps. On the other hand, the JVP method requires an almost fixed number of time steps. Consequently, the total simulation is almost linear with respect to the problem size.

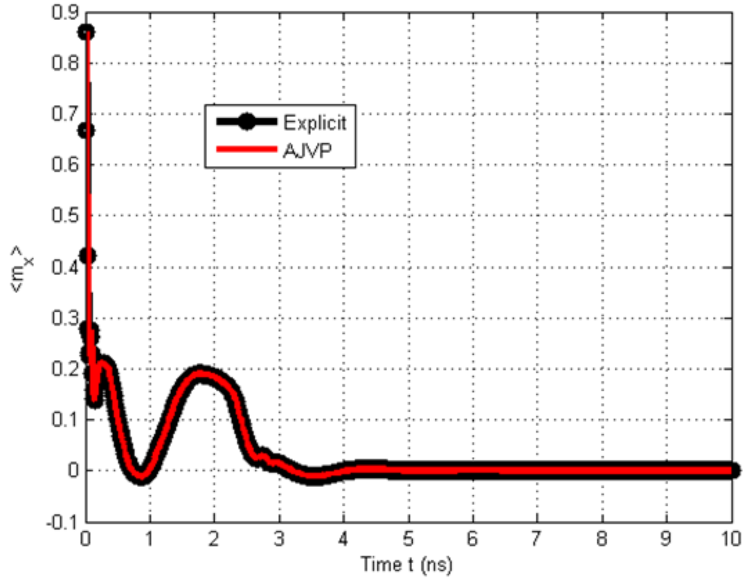

Figure 3.1: Comparison of the average m_x in M5.

3.7 Conclusion

A new operator-based analytic method for computing JVPs encountered in implicit time integration of LLGE was proposed. The linear operator $\mathcal{L}$ plays a critical role in the implementation of AJVP. The AJVP is highly accurate because it uses no approximation. Its accuracy is of the same level as that of the RHS evaluations. The presented approaches are also cost-effective, without increasing memory consumption or extra RHS evaluations. Numerical examples validate our methods. Moreover, they are applicable for many other simulations.

The proposed methods can also be useful in preconditioning. For example, we can discard the magnetostatic field in the AJVPs, and use them as a preconditioner to the original dense system. We can also apply the AJVPs to nonlinear differential equations (i.e. $\mathbf{M} \times \mathbf{H}_{\text{eff}} = \mathbf{0}$) to solve for equilibrium states from the LLGE. Further research includes providing an efficient preconditioning for solving the linear equations associated with the Jacobian matrix. For instance, we could formulate explicitly the Jacobian matrix for a small region of the mesh which is densely discretized, and invert the blockwise Jacobians with brute forces such as

Table 3.2: List of analytic formulas for JVPs

Name	Function	Jacobian-vector product
Precessional term	$\mathbf{m} \times (\mathcal{L}\mathbf{m} + \mathbf{H}_{\text{app}})$	$\mathbf{v} \times (\mathcal{L}\mathbf{m} + \mathbf{H}_{\text{app}}) + \mathbf{m} \times \mathcal{L}\mathbf{v}$
Damping term	$\mathbf{m} \times [\mathbf{m} \times (\mathcal{L}\mathbf{m} + \mathbf{H}_{\text{app}})]$	$\mathbf{v}\times[\mathbf{m}\times(\mathcal{L}\hat{\mathbf{m}}+\mathbf{H}_{\text{app}})]+\hat{\mathbf{m}}\times[\mathbf{v}\times(\mathcal{L}\mathbf{m}+\mathbf{H}_{\text{app}})]+\mathbf{m}\times(\mathbf{m}\times\mathcal{L}\mathbf{v})$
Nnonadiabatic term	$\mathbf{m} \times \mathbf{j} \cdot \nabla\mathbf{m}$	$\mathbf{v} \times \mathbf{j} \cdot \nabla\mathbf{m} + \mathbf{m} \times \mathbf{j} \cdot \nabla\mathbf{v}$
The other term	$\mathbf{m} \times (\mathbf{m} \times \mathbf{j} \cdot \nabla\mathbf{m})$	$\mathbf{v} \times \mathbf{m} \times \mathbf{j} \cdot \nabla\hat{\mathbf{m}} + \mathbf{m} \times \mathbf{v} \times \mathbf{j} \cdot \nabla\mathbf{m} + \mathbf{m} \times \mathbf{m} \times \mathbf{j} \cdot \nabla\mathbf{v}$
Normalization	$\frac{\mathbf{m}}{\lvert\mathbf{m}\rvert}$	$\frac{\mathbf{v}}{\lvert\mathbf{m}\rvert} - \frac{\mathbf{m}\cdot\mathbf{v}}{\lvert\mathbf{m}\rvert^3}\mathbf{m}$
Advection term	$\mathbf{m} \cdot \nabla\mathbf{m}$	$\mathbf{v} \cdot \nabla\mathbf{m} + \mathbf{m} \cdot \nabla\mathbf{v}$

Gaussian elimination. The stiffness of the whole problem may be greatly relieved and higher speed-ups can be achieved. The commonly used functions in the LLGE is listed in Table 3.2.

Chapter 4

New basis functions for surface integral equations

Surface integral equations (SIEs) are a powerful tool for modeling a myriad of electromagnetic related problems such as scattering, diffraction, reflection and transmissions. The SIEs assume that electric and magnetic currents are present on the surfaces [34, 85]. Traditional approach to solving SIEs models a surface by discretizing it into a number of triangles.

In this chapter, we present a framework for solving surface integral equation on quadrilateral, triangular, and mixed quadrilateral-triangular meshes. A quadrilateral basis function (QBF) is defined for each edge that separates two quadrilaterals. The QBF seems to be impertinent to the triangular mesh. The initial meshes are represented in terms of quadrilateral barycentric meshes (QBM-s), which are obtained by partitioning each initial quadrilateral and triangle into four and three barycentric quadrilaterals, respectively. After the barycentric refinement, each "small" edge is associated with a QBF (To distinguish it from the original QBF, the QBF on the barycentric mesh is termed bQBF).

The bQBFs serve a dual role. First, they allow forming primary basis functions (PBFs) [86], which are well suited for representing surface currents on quadrilateral, triangular and mixed meshes. Second, the bQBFs are used to construct dual basis function (DBFs), which are natural for using in conjunction with Calderón multiplicative preconditioners (CMPs). These bQBFs, PBFs, and DBFs result in a substantial reduction in the number of nonzero elements in the sparse projection matrices for PBFs and DBFs as well as reduction of unknowns and quadrature points. When these PBFs and DBFs are used in CMPs, they reduce the number of iterations and eliminate the dense mesh breakdown of the surface electric field integral equation. Numerical examples demonstrate the efficiency of using the introduced bQBFs with associated PBFs and DBFs for solving electromagnetic surface electric field integral equations on quadrilateral, triangular, and mixed meshes.

4.1 Introduction to surface integral equations

Electromagnetic scattering is a universal phenomena. The reflection, transmission, dispersion of lights are all special cases of scattering. The scattering theory assumes that the total field $(\mathbf{E}, \mathbf{H})$ has two parts [87]. The first one is the incident field $(\mathbf{E}^{\mathrm{inc}}, \mathbf{H}^{\mathrm{inc}})$, which are generated by some sources at an angular frequency of ω. A time convention $\exp(i\omega t)(i = \sqrt{-1})$ is assumed and suppressed. If the sources are far away from the scatterer, the incident field is a plane wave. The corresponding wavenumber is $k = \frac{4\pi^2 c}{\omega}$, where c is the speed of light. The second part is the scattered one $(\mathbf{E}^{\mathrm{sc}}, \mathbf{H}^{\mathrm{sc}})$, which is induced by the incident field inside the scatterers. The relation is simply:

$$\mathbf{E} = \mathbf{E}^{\mathrm{inc}} + \mathbf{E}^{\mathrm{sc}}, \mathbf{H} = \mathbf{H}^{\mathrm{inc}} + \mathbf{H}^{\mathrm{sc}}. \tag{4.1}$$

Surface integral equations (SIEs) are extensively used for analyzing electromagnetic radiation and scattering from perfect electric conducting (PEC) structures and homogeneous dielectric materials [88]. Two kinds of SIEs or their combinations are frequently used: electric field integral equation (EFIE) and magnetic field integral equation (MFIE), which are obtained by enforcing boundary conditions for tangential electric and magnetic fields, respectively.

Consider a surface Γ, which supports a surface electric current $\mathbf{J}$, and a

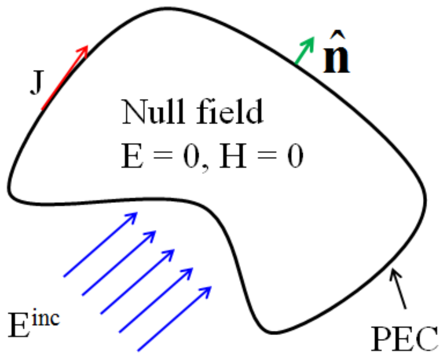

Figure 4.1: Scattering of electromagnetic field from a PEC surface. The scatterer is PEC. There is an induced electric current **J** flowing on the surface of the PEC.

surface magnetic current **M**. The relationship is simply put:

$$\begin{aligned}\mathbf{A}(\mathbf{r}) &= \oiint_\Gamma \frac{\exp(-ik|\mathbf{r}-\mathbf{r}'|)}{4\pi|\mathbf{r}-\mathbf{r}'|}\mathbf{J}(\mathbf{r}')d\mathbf{r}',\\ \mathbf{F}(\mathbf{r}) &= \oiint_\Gamma \frac{\exp(-ik|\mathbf{r}-\mathbf{r}'|)}{4\pi|\mathbf{r}-\mathbf{r}'|}\mathbf{M}(\mathbf{r}')d\mathbf{r}'.\end{aligned} \tag{4.2}$$

The scattered fields generated by the potentials are written as

$$\begin{aligned}\mathbf{E}^{\mathrm{sc}} &= \frac{i}{k}(\nabla\nabla\cdot + k^2)\mathbf{A} - \eta\nabla\times\mathbf{F},\\ \mathbf{H}^{\mathrm{sc}} &= \frac{i}{k}(\nabla\nabla\cdot + k^2)\mathbf{F} + \frac{1}{\eta}\nabla\times\mathbf{A}.\end{aligned} \tag{4.3}$$

4.1.1 EFIE and MFIE operators

Consider a PEC surface Γ, which supports a surface current distribution **J** induced by an incident time harmonic electric field $\mathbf{E}^{\mathrm{inc}}$ [89]. The magnetic current is absent, i.e. $\mathbf{M} = \mathbf{0}$. The scattered and the incident fields are related through

$$\mathcal{T}(\mathbf{J}) = \hat{\mathbf{n}} \times \mathbf{E}^{\mathrm{sca}}/\eta = -\hat{\mathbf{n}} \times \mathbf{E}^{\mathrm{inc}}/\eta \tag{4.4}$$

where η is the wave impedance and $\mathcal{T}$ is the EFIE operator which is split into its singular and hypersingular parts: $\mathcal{T} = \mathcal{T}_s + \mathcal{T}_h$.

$$[\mathcal{T}_s(\mathbf{J})](\mathbf{r}) = ik\hat{\mathbf{n}} \times \oiint_\Gamma \frac{\exp(-ik|\mathbf{r}-\mathbf{r}'|)}{4\pi|\mathbf{r}-\mathbf{r}'|}\mathbf{J}(\mathbf{r}')d\mathbf{r}', \tag{4.5}$$

Table 4.1: Comparisons between $\mathcal{T}$ and $\mathcal{K}$

EFIE $\mathcal{T}$	MFIE $\mathcal{K}$
Easy to implement	Difficult to implement
Discontinuous operator	Compact/bounded operator
Applies to open structure	Applies only to closed surface
Numerically more accurate	Numerically less accurate

$$[\mathcal{T}_h(\mathbf{J})](\mathbf{r}) = \frac{i}{k}\hat{\mathbf{n}} \times \nabla \oiint_{\Gamma} \frac{\exp(-ik|\mathbf{r}-\mathbf{r}'|)}{4\pi|\mathbf{r}-\mathbf{r}'|} \nabla'_S \cdot \mathbf{J}(\mathbf{r}') d\mathbf{r}'. \tag{4.6}$$

The same phenomena can be describe by enforcing the boundary conditions for the magnetic field [90], yielding the MFIE:

$$\frac{\mathbf{J}}{2} - \mathcal{K}(\mathbf{J}) = \hat{\mathbf{n}} \times \mathbf{H}^{\text{inc}}, \tag{4.7}$$

where the MFIE operator is:

$$[\mathcal{K}(\mathbf{J})](\mathbf{r}) = \hat{\mathbf{n}} \times \nabla \times \oiint_{\Gamma} \frac{\exp(-ik|\mathbf{r}-\mathbf{r}'|)}{4\pi|\mathbf{r}-\mathbf{r}'|} \mathbf{J}(\mathbf{r}') d\mathbf{r}'. \tag{4.8}$$

$\mathcal{T}$ and $\mathcal{K}$ are the most commonly used integral operators in electromagnetics [34, 85]. They have quite different characteristics although they are closely related to each Computational Methods for Electromagneticsother. The properties of these two operators are summarized in Table 4.1.

$\mathcal{T}$ is an ill-posed operator. While the singular values of $\mathcal{T}_s$ cluster around the origin, that of $\mathcal{T}_h$ gather at infinity. As a result, $\mathcal{T}$ has two branches of singular values [1], one at zero and the other at infinity, and its condition number approaches infinity when densely discretized. $\mathcal{K}$ is a compact operator for smooth geometries, which means that its singular values are concentrated around zero. Consequently, $\frac{\mathcal{I}}{2} \pm \mathcal{K}$ is well-conditioned and gives fast convergence in an iterative solver. Here $\mathcal{I}$ is an identity operator on Γ.

Resonances happen when the operators have a nontrivial nullspace:

$$\mathcal{T}(\mathbf{J}) = \mathbf{0}, \left(\frac{\mathcal{I}}{2} - \mathcal{K}\right)(\mathbf{J}) = \mathbf{0}. \tag{4.9}$$

---

[1] It is noteworthy to mention the differences between singular values and eigenvalues for an operator $\mathcal{T}$. There are no necessary relationships between the two, since the singular values of $\mathcal{T}$ are the square root of eigenvalues of $\mathcal{T}^\dagger\mathcal{T}$, where $\mathcal{T}^\dagger$ is the conjugate transpose of $\mathcal{T}$.

where **J** is a nonzero function. Sometimes the resonance is physical, because the fields are bouncing back and forth inside the closed structure. However, the resonance is often fictitious. In this case, the solutions to either EFIE or MFIE are not unique. To make sure that unique solution exists, the combined field integral equation (CEIE) is used:

$$\mathcal{C}_\alpha(\mathbf{J}) = \alpha\mathcal{T}(\mathbf{J}) + (1-\alpha)\left(\frac{\mathcal{I}}{2} - \mathcal{K}\right)(\mathbf{J}) = \alpha\frac{\hat{\mathbf{n}} \times \mathbf{E}^{\mathrm{inc}}}{\eta} + (1-\alpha)\hat{\mathbf{n}} \times \mathbf{H}^{\mathrm{inc}}. \quad (4.10)$$

where α is a constant in the range of $0 < \alpha < 1$.

4.1.2 Calderón identities

Both EFIE and MFIE are mathematical abstractions of the electromagnetic scattering phenomena. They can be solved separately or simultaneously. There must some relationships between them, which are best characterized by the Calderón identities [91, 92, 93, 94]:

$$\mathcal{T}^2 - \mathcal{K}^2 = -\frac{\mathcal{I}}{4}, \mathcal{T}\mathcal{K} + \mathcal{K}\mathcal{T} = \mathcal{O}. \quad (4.11)$$

It has been suggested that $\mathcal{T}$ can be regularized into a second kind integral operator as a direct consequence of the Calderón identities. Based on the fact that $\mathcal{K}$ and $\mathcal{K}^2$ are compact operators, it follows from Eq. (4.11) that $\mathcal{T}^2$ has a bounded singular value spectrum clustered at $-\frac{1}{4}$ [95]. Consequently, $\mathcal{T}^2$ has better spectrum properties than $\mathcal{T}$. However, the discretization of $\mathcal{T}^2$ is more complicated than that of $\mathcal{T}$ because there is no closed form for $\mathcal{T}^2$. From the identity $\nabla_S \cdot (\hat{\mathbf{n}} \times \nabla\phi) \equiv 0$, where ϕ is an arbitrary scalar function defined on Ω, it follows that square of $\mathcal{T}_h$ always vanishes, i.e. $\mathcal{T}_h^2 = \mathcal{O}$, which is necessary for implementing CMP [95]. Any Calderón based preconditioner must satisfy this property. Since $\mathcal{T}^2 = \mathcal{T}_s^2 + \mathcal{T}_s\mathcal{T}_h + \mathcal{T}_h\mathcal{T}_s$, one may just drop the term $\mathcal{T}_h^2$ in numeric solutions, but in this way the preconditioner is not multiplicative and it is very complicated, suffered from low accuracy and speed issues.

This working mechanism of a preconditioner based on the Calderón identities is closely related to the properties of surface current and the v-BFs.

4.2 Vector basis functions on surfaces

The representation of currents on a surface is important for calculating **J** and/or **M**. To accommodate for numerical computations in numerical methods, current can be modeled on the meshed elements, where basis functions (BFs) are defined and are used to expand **J** and **M**.

Rao-Wilton-Glisson (RWG) [39] BFs on are among the most popular divergence-conforming vector BFs for triangular meshes. In this section, we focus on defining v-BFs on a quadrilateral mesh.

4.2.1 Parameterized quadrilaterals

The of RWG-BFs seem to be quite simple. However, the definition of v-BFs on quadrilateral meshes is more involved. Early work already handled the case of rooftop BFs on rectangular elements. However, QBFs on an arbitrary quadrilateral mesh were proposed much later. To describe such an element, we must borrow the language of differential geometry. A quadrilateral is formed by four non-overlapping vertices, which are not necessarily coplanar. Any quadrilateral

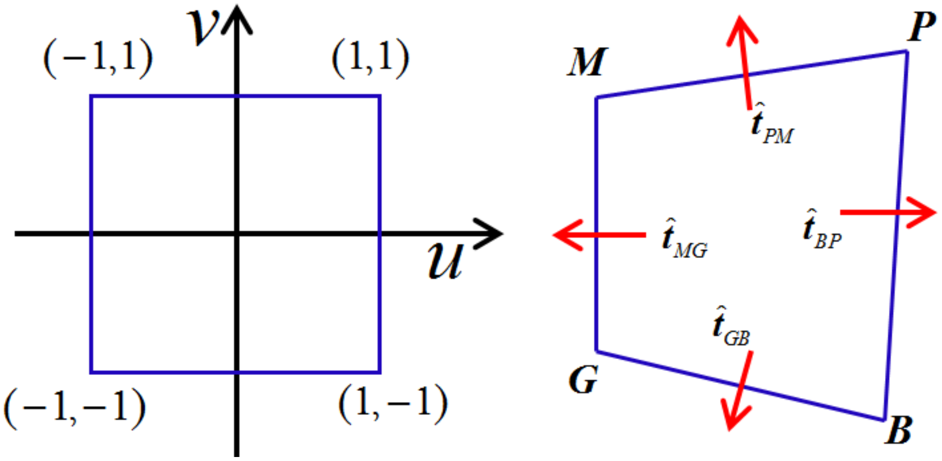

Figure 4.2: Via a bilinear transformation, a square is projected into a quadrilateral **GBPM**. $\hat{\mathbf{t}}_{\mathbf{GB}}, \hat{\mathbf{t}}_{\mathbf{BP}}, \hat{\mathbf{t}}_{\mathbf{PM}}$ and $\hat{\mathbf{t}}_{\mathbf{MG}}$ are unit vectors normal to the boundary edges and perpendicular to $\hat{\mathbf{n}}$.

can be viewed as a mapping from a parametric square to the physical space [21]:

$$\mathbf{r} = N_0(u,v)\mathbf{G} + N_1(u,v)\mathbf{B} + N_2(u,v)\mathbf{P} + N_3(u,v)\mathbf{M}, \tag{4.12}$$

where $u, v \in [-1,1]$, $N_0(u,v), N_1(u,v), N_2(u,v), N_3(u,v)$ are s-BFs:

$$\begin{aligned} N_0(u,v) &= \frac{(1-u)(1-v)}{4}, N_1(u,v) = \frac{(1+u)(1-v)}{4}, \\ N_2(u,v) &= \frac{(1+u)(1+v)}{4}, N_3(u,v) = \frac{(1-u)(1+v)}{4}. \end{aligned} \tag{4.13}$$

Two natural basis vectors tangential to the quadrilateral are [96]:

$$\begin{aligned} \mathbf{r}_u &= \frac{\partial \mathbf{r}}{\partial u} = \frac{1}{4}\left[(1-v)(\mathbf{B}-\mathbf{G}) + (1+v)(\mathbf{P}-\mathbf{M})\right], \\ \mathbf{r}_v &= \frac{\partial \mathbf{r}}{\partial v} = \frac{1}{4}\left[(1-u)(\mathbf{M}-\mathbf{G}) + (1+u)(\mathbf{P}-\mathbf{B})\right]. \end{aligned} \tag{4.14}$$

Furthermore, we have $\mathbf{r}_{uu} = \frac{\partial^2 \mathbf{r}}{\partial u^2} = \mathbf{0}, \mathbf{r}_v = \frac{\partial^2 \mathbf{r}}{\partial v^2} = \mathbf{0}, \mathbf{r}_{uv} = \frac{\partial^2 \mathbf{r}}{\partial u \partial v} = \frac{1}{4}(\mathbf{P}+\mathbf{G}-\mathbf{B}-\mathbf{M})$. If $\mathbf{r}_{uv} = \frac{\partial^2 \mathbf{r}}{\partial u \partial v} \neq \mathbf{0}$, the quadrilateral has a negative curvature. A unit vector normal to the surface is $\hat{\mathbf{n}} = \mathbf{r}_u \times \mathbf{r}_v / |\mathbf{r}_u \times \mathbf{r}_v|$. The determinant of Jacobian is $\det(\mathbf{j}) = \mathbf{r}_u \times \mathbf{r}_v \cdot \hat{\mathbf{n}} = |\mathbf{r}_u \times \mathbf{r}_v|$. An arbitrary vector function is applied on the surface:

$$\mathbf{f}(\mathbf{r}) = \frac{f_1(u,v)\mathbf{r}_u + f_2(u,v)\mathbf{r}_v}{\det(\mathbf{j})}, \tag{4.15}$$

where $f_1(u,v), f_2(u,v)$ are arbitrary differentiable functions. The surface divergence of $\mathbf{f}(\mathbf{r})$ is

$$\nabla_S \cdot \mathbf{f}(\mathbf{r}) = \frac{1}{\det(\mathbf{j})}\left(\frac{\partial f_1}{\partial u} + \frac{\partial f_2}{\partial v}\right). \tag{4.16}$$

Consider a special vector field on this quadrilateral:

$$\mathbf{f}(\mathbf{r}) = \frac{(1+u)\mathbf{r}_u}{\det(\mathbf{j})}. \tag{4.17}$$

As shown in Fig. 4.2, **GBPM**. $\hat{\mathbf{t}}_{\mathbf{GB}}, \hat{\mathbf{t}}_{\mathbf{BP}}, \hat{\mathbf{t}}_{\mathbf{PM}}$ and $\hat{\mathbf{t}}_{\mathbf{MG}}$ are outward pointing unit vectors normal to the four edges and also to $\hat{\mathbf{n}}$. According to Eq. (4.14), on the edge $\mathbf{MG}, u = -1$ and $\mathbf{f}(u,v) = \mathbf{0}$. On the edge $\mathbf{GB}$, $v = -1$ and $\mathbf{r}_u = (\mathbf{G}-\mathbf{B})/2$, which indicates that $\mathbf{f}(u,v) \cdot \hat{\mathbf{t}}_{\mathbf{GB}} = \mathbf{0}$. Similarly, it is found $\mathbf{f}(u,v) \cdot \hat{\mathbf{t}}_{\mathbf{PM}} = \mathbf{0}$. Finally, on the edge $\mathbf{BP}$, $u = 1$ and $\mathbf{r}_v = (\mathbf{P}-\mathbf{B})/2$. One has

$$\mathbf{f}(u,v) \cdot \hat{\mathbf{t}}_{\mathbf{BP}} = \frac{2\mathbf{r}_u}{\det(\mathbf{j})} \cdot \frac{2\mathbf{r}_v \times \hat{\mathbf{n}}}{L_{\mathbf{BP}}} = \frac{4}{L_{\mathbf{BP}}}, \tag{4.18}$$

where $L_{\mathbf{BP}}$ is the length of edge $\mathbf{BP}$. It is therefore clear that $\mathbf{f}(u, v)$ has zero normal components on edges $\mathbf{GB}, \mathbf{BP}$, and $\mathbf{MG}$, it has a constant normal component on $\mathbf{BP}$. In accordance to (4.16), the surface divergence of (4.17) is $\nabla_S \cdot \mathbf{f}(u, v) = \frac{1}{\det(\mathbf{j})}$. It follows from (4.16) that the total charge on the surface is $\iint_Q \nabla_S \cdot \mathbf{j} dS = \iint_Q \frac{1}{\det(\mathbf{j})} dS = \int_{-1}^{1} du \int_{-1}^{1} dv = 4$. This result is totally independent of the shape or size of the quadrilateral.

4.2.2 Quadrilateral basis function

The QBF described here is the 0th order BFs defined on quadrilaterals in reference, it [25] is also a generalization of the rooftop BF on rectangles [87]. Similar to the RWG defined on two adjacent triangles, the QBF is supported over a pair of adjacent quadrilaterals (Fig. 4.3). The first quadrilateral, Q_1, is formed by vertices $\mathbf{G}, \mathbf{B}, \mathbf{P}, \mathbf{M}$ and the second quadrilateral, Q_2, is formed by the vertices $\mathbf{B}, \mathbf{H}, \mathbf{N}, \mathbf{P}$, The quadrilaterals are parameterized as

$$\mathbf{r} = \begin{cases} N_0(u_1, v_1)\mathbf{G} + N_1(u_1, v_1)\mathbf{B} + N_2(u_1, v_1)\mathbf{P} + N_3(u_1, v_1)\mathbf{M}, \mathbf{r} \in Q_1, \\ N_0(u_2, v_2)\mathbf{B} + N_1(u_2, v_2)\mathbf{H} + N_2(u_2, v_2)\mathbf{N} + N_3(u_2, v_2)\mathbf{P}, \mathbf{r} \in Q_2, \end{cases} \tag{4.19}$$

where $u_1, u_2 \in [-1, 1]$. Similar to (4.14), on each quadrilateral, two natural tangential vectors are given by $\mathbf{r}_{ui} = \frac{\partial \mathbf{r}}{\partial u_i}, \mathbf{r}_{vi} = \frac{\partial \mathbf{r}}{\partial v_i}$, a unit normal vector is $\hat{\mathbf{n}}_i = \frac{\mathbf{r}_{ui} \times \mathbf{r}_{vi}}{|\mathbf{r}_{ui} \times \mathbf{r}_{vi}|}$, the determinant of the Jacobian is $\det(\mathbf{j}_i) = \hat{\mathbf{n}}_i \cdot \mathbf{r}_{ui} \times \mathbf{r}_{vi}$ [97]. A divergence conforming BF associated with $\mathbf{BP}$ is

$$\mathbf{b}_{\mathbf{BP}}^{QBF}(\mathbf{r}) = \begin{cases} (1 + u_1)\frac{\mathbf{r}_{u1}}{\det(\mathbf{j}_1)}, \mathbf{r} \in Q_1, \\ (1 - u_2)\frac{\mathbf{r}_{u2}}{\det(\mathbf{j}_2)}, \mathbf{r} \in Q_2. \end{cases} \tag{4.20}$$

$\mathbf{b}_{\mathbf{BP}}^{QBF}(\mathbf{r})$ represents a current starting from edge $\mathbf{GM}$, crossing $\mathbf{BP}$, and terminating at $\mathbf{HN}$. It effectively depicts a current perpendicular to $\mathbf{BP}$. It is parallel to edges $\mathbf{GB}$, $\mathbf{BH}$, $\mathbf{NP}$ and $\mathbf{PM}$ and has a constant normal component on the edge BP equal to $\frac{4}{L_{\mathbf{BP}}}$. There is no fictitious line charge along any edge. As indicated by (4.16), the surface divergence of $\mathbf{b}_{\mathbf{BP}}^{QBF}(\mathbf{r})$ is

$$\nabla_S \cdot \mathbf{b}_{\mathbf{BP}}^{QBF}(\mathbf{r}) = \begin{cases} \frac{1}{\det(\mathbf{j}_1)}, \mathbf{r} \in Q_1, \\ \frac{-1}{\det(\mathbf{j}_2)}, \mathbf{r} \in Q_2. \end{cases} \tag{4.21}$$

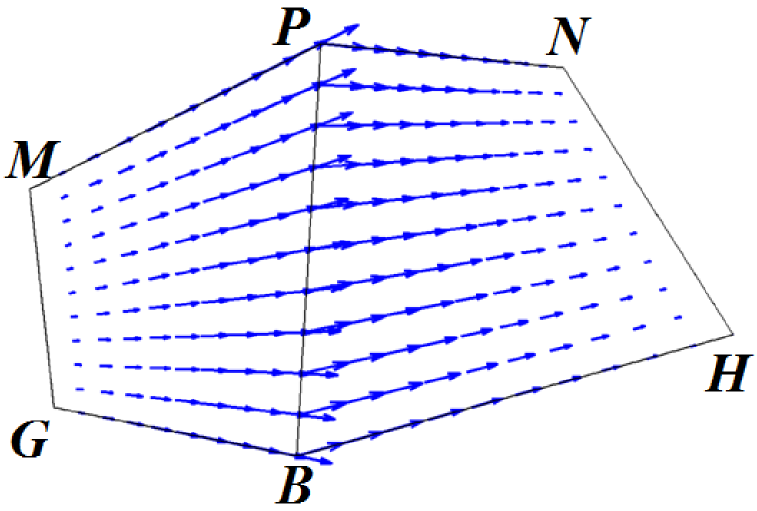

Figure 4.3: A QBF representing a current flow across edge **BP**. It has a postive charge density on Q_1 and negative charge density on Q_2.

The quadrilateral Q_1 has a positive charge density, and the total charge is 4. The quadrilateral Q_2 has a negative charge density, and the total charge is -4, making the charge conservation automatically enforced. Unlike RWG-BFs on triangles, the charge density on a quadrilateral is generally not uniform, except when it is a parallelogram. The charge density is inversely proportional to $\det(\mathbf{j}_i)$. However, Eq. (4.16) indicates that the charge is uniform in the parameter space (u, v), which eases numerical integrations. It is further noted that the BF (4.20) has units of inverse length. This definition is chosen to make the Gram matrix dimensionless and well-conditioned for the CMP implemented in this chapter. Eq. (4.20) can also be normalized to become dimensionless. The QBFs defined on QBMs serve here as a building-block for constructing new sets of PBFs and DBFs as well as for implementing a CMP for quadrilateral, triangular, and mixed meshes. The QBFs can also be used to discretize the EFIE and MFIE for an all-quadrilateral mesh.

4.2.3 Matrix equation for SIEs

Once the surface is meshed and we have proper v-BFs. One can define two column vectors $\boldsymbol{I} = [I_1, I_2, \ldots, I_{N_E}]^T, \boldsymbol{V} = [V_1, V_2, \ldots, V_{N_E}]^T$. $\boldsymbol{I}$ and $\boldsymbol{V}$ denote the vectors for the electric current and excitation, respectively. The unknown surface current $\mathbf{J}(\mathbf{r})$ is expanded in terms of the v-BFs on a polygonal mesh:

$$\mathbf{J}(\mathbf{r}) \approx \sum_{n=1}^{n=N_E} I_n \mathbf{f}_n(\mathbf{r}). \tag{4.22}$$

Here I_n is a complex-valued coefficient of the m-th v-BF. With these formulas in hand, the impedance matrix $\mathbb{Z}$ can be written as

$$\mathbb{Z}_{mn}^{EFIE} = i \iint_{S_m} d\mathbf{r} \iint_{S_n} d\mathbf{r}' \frac{e^{-ik|\mathbf{r}-\mathbf{r}'|}}{4\pi\,|\mathbf{r}-\mathbf{r}'|} \left[k\mathbf{f}_m(\mathbf{r}) \cdot \mathbf{f}_n(\mathbf{r}') - \frac{\nabla_S \cdot \mathbf{f}_m(\mathbf{r}) \nabla'_S \cdot \mathbf{f}_n(\mathbf{r}')}{k} \right]. \tag{4.23}$$

The matrix $\mathbb{Z}^{EFIE}$ is complex-valued and symmetric. The BF $\mathbf{f}_n(\mathbf{r}')$ residing on a pair of polygons P_n^+, P_n^- is the source, and the TF $\mathbf{f}_m(\mathbf{r})$ residing on another pair of triangles P_m^+, P_m^- is the receiver. Therefore, the BF and TF can be regarded as transmitter and receiver antennas respectively. As a four-fold integral, $\mathbb{Z}_{mn}^{EFIE}$ is difficult to evaluate. Our approach is to first calculate the vector and scalar potentials, and then integrate the potentials using standard quadrature.

As to the MFIE, the discretized matrix equation becomes:

$$\frac{1}{2} \sum_{n=1}^{n=N_E} I_n \mathbf{f}_n(\mathbf{r}) - \hat{\mathbf{n}} \times \nabla \times \sum_{n=1}^{n=N_E} I_n \oiint_{\Gamma} \frac{e^{-ik|\mathbf{r}-\mathbf{r}'|}}{4\pi\,|\mathbf{r}-\mathbf{r}'|} \mathbf{f}_n(\mathbf{r}') d\mathbf{r}' \approx \hat{\mathbf{n}} \times \mathbf{H}^{\text{inc}}. \tag{4.24}$$

The next procedure is to test Eq. (4.24). The choice of test functions is not obvious [98, 99]. Traditional approach used the Galerkin methods:

$$\sum_{n=1}^{n=N_E} \left\langle \mathbf{f}_m, \frac{1}{2}\mathbf{f}_n(\mathbf{r}) - \hat{\mathbf{n}} \times \nabla \times \oiint_{\Gamma} \frac{e^{-ik|\mathbf{r}-\mathbf{r}'|}}{4\pi\,|\mathbf{r}-\mathbf{r}'|} \mathbf{f}_n(\mathbf{r}') d\mathbf{r}' \right\rangle I_n \approx \left\langle \mathbf{f}_m, \hat{\mathbf{n}} \times \mathbf{H}^{\text{inc}} \right\rangle. \tag{4.25}$$

The above equation has a matrix form:

$$\mathbb{Z}^{MFIE} \boldsymbol{I} = \boldsymbol{H}, \tag{4.26}$$

where $\mathbb{Z}^{MFIE}$ is an $N_E \times N_E$ matrix, $\boldsymbol{H} = [H_1, H_2, \ldots, H_{N_E}]^T$ is the excitation vector. In Eq. (4.25), unfortunately, the curl operator $\nabla\times$ cannot be moved to either the $\mathbf{f}_m$ or $\mathbf{f}_n$. Therefore, one has to handle the hypersingular integrand $\nabla G_k(\mathbf{r}, \mathbf{r}')$. Although both EFIE and MFIE can be solved using the v-BFs, in practice, it was found that the EFIE formulation gives rise to a much more accurate solution than Eq. (4.26) [100, 98, 101].

4.3 Necessity of dual basis functions

The electric and magnetic currents are quasi-orthogonal to each other on surfaces. Therefore, two sets of BFs are needed for their representation, namely primary basis functions (PBFs) and dual basis functions (DBFs). Combined applications of PBFs and DBFs can yield well-conditioned discretized matrix systems and suppress fictitious resonances for homogeneous dielectric scattering problems [102, 103, 104, 105]. DBFs are indispensable not only for dielectric but also for PEC structures where only electric currents are present. For instance, the EFIE operator $\mathcal{T}$ is known to give rise to ill-conditioned impedance matrices upon discretization. Based on Calderón identities [106, 107, 108], Calderón multiplicative preconditioners (CMPs) [95, 109] were proposed to attack this problem, where operator product $\mathcal{T}\mathcal{T}$ is involved. DBFs are needed to properly implement the CMPs. Moreover, the MFIE has poor accuracy if RWG is used as both expansion function and testing function (TF). The accuracy can be greatly improved if DBFs of RWG-BFs are used as TFs [110, 101, 111, 112]. To meet these requirements [102], DBFs should (i) lead to no fictitious line charge, (ii) have the same number as that of PBFs, (iii) be divergence-conforming and quasi-curl conforming, (iv) be quasi-orthogonal to PBFs, (v) yield well-conditioned Gram matrix, (vi) and ensure cancellation of the square of the hypersingular part of the EFIE operator.

4.4 Quadrilateral Barycentric Meshes

This section defines QBMs for quadrilateral, triangular and mixed meshes and describes the parameterization of barycentric quadrilaterals. Then, it defines bQBFs based on two adjacent quadrilaterals. These bQBFs are used for constructing PBFs and DBFs.

We start by defining QBM for quadrilaterals, proceed with triangles, and complete with mixed quadrilateral-triangle combinations. Consider a mesh consisting of N_Q convex quadrilaterals. Shown in Fig. 4.4 are two adjacent quadrilaterals $Q_1(\mathbf{ABEF})$ and $Q_2(\mathbf{BCDE})$.

A QBM is constructed by partitioning each quadrilateral into four barycentric quadrilaterals, which is accomplished by connecting its centroid with its edges midpoints. In Fig. 4.4, $\mathbf{M} = \frac{\mathbf{A}+\mathbf{B}+\mathbf{E}+\mathbf{F}}{4}$ is the centroid of $Q_1, \mathbf{G}, \mathbf{P}, \mathbf{K}, \mathbf{L}$ are the midpoints of edges $\mathbf{AB}, \mathbf{BE}, \mathbf{EF}$, and $\mathbf{FA}$. Similarly, $\mathbf{N} = \frac{\mathbf{B}+\mathbf{C}+\mathbf{D}+\mathbf{E}}{4}$ is the centroid of $Q_2, \mathbf{H}, \mathbf{I}, \mathbf{J}, \mathbf{P}$ are the midpoints of edges $\mathbf{BC}, \mathbf{CD}, \mathbf{DE}$, and $\mathbf{EB}$, respectivley. Dividing Q_1 yields four barycentric quadrilaterals $\boldsymbol{\alpha}, \boldsymbol{\beta}, \boldsymbol{\gamma}, \boldsymbol{\delta}$ and Q_2 also gives rise to four barycentric quadrilaterals $\boldsymbol{\epsilon}, \boldsymbol{\zeta}, \boldsymbol{\eta}, \boldsymbol{\theta}$. These barycentric quadrilaterals form a QBM, and the total number of barycentric quadrilaterals is $4N_Q$. Now consider a triangular mesh having N_T triangles. Shown in Fig. 4(a) are two adjacent triangles $T_1(\mathbf{ABD})$ and $T_2(\mathbf{BCD})$. The total number of bQBFs in a mixed mesh is $2N_E + 3N_T + 4N_Q$.

Dividing an original mesh into smaller quadrilaterals seems to increase the complexity. However, the purpose is to develop new BFs that have superior properties for both EFIE and MFIE. With more v-BFs, one can combine the bQBFs to get new PBF and their DBFs.

4.5 New Primal basis functions

This section introduces PBFs for quadrilateral, triangular, and mixed meshes. Each PBF is associated with an edge separating two elements, and the PBF denotes a current flow that is approximately perpendicular to the edge.

4.5.1 Quadrilateral meshes

Consider the two quadrilaterals in Fig. 4.4. A PBF is designated for edge **BE** that separates the two quadrilaterals and is expressed as a linear combination of six bQBFs:

$$\mathbf{f}_{\mathbf{BE}} = c_1(\mathbf{b}_1 + \mathbf{b}_2) + c_2(\mathbf{b}_3 + \mathbf{b}_4 + \mathbf{b}_5 + \mathbf{b}_6), \tag{4.27}$$

where $\mathbf{b}_1$ through $\mathbf{b}_6$ are bQBFs defined in Eq. (4.20) associated with the barycentric edges 1 through 6 belonging to the two quadrilaterals in Fig. 4.4. The edges $\mathbf{LM}, \mathbf{MP}, \mathbf{PN}, \mathbf{NI}$ are not included since their directions are approximately perpendicular to the edge **BE**. The other edges such as $\mathbf{AG}, \mathbf{GB}, \mathbf{BH}, \mathbf{HC}, \mathbf{CI}, \mathbf{ID}$, $\mathbf{DJ}, \mathbf{JE}, \mathbf{EK}, \mathbf{KF}, \mathbf{FL}, \mathbf{LA}$ are not used. The coefficients for $\mathbf{b}_1$ and $\mathbf{b}_2$ must be

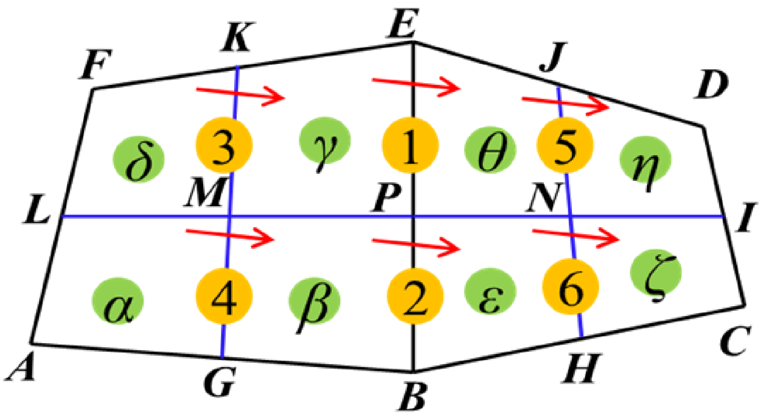

Figure 4.4: A PBF associated with edge **BE**, resides on two adjacent initial quadrilaterals Q_1 and Q_2. It is a linear combination of six bQBFs ($\mathbf{b}_1$ through $\mathbf{b}_6$) denoted by red arrows.

equal because the two are symmetric. Similarly, the coefficients of $\mathbf{b}_3$, $\mathbf{b}_4$, $\mathbf{b}_5$, $\mathbf{b}_6$ must be identical. We simply let $c_1 = \frac{1}{2}$. The remaining question is to determine c_2. The charge quadrilaterals $\boldsymbol{\alpha}, \boldsymbol{\beta}, \boldsymbol{\gamma}, \boldsymbol{\delta}$ should be equal, i.e. $c_1 - c_2 = c_2$. So one has $c_2 = \frac{1}{4}$. The expression is therefore:

$$\mathbf{f}_{\mathbf{BE}} = \frac{\mathbf{b}_1 + \mathbf{b}_2}{2} + \frac{\mathbf{b}_3 + \mathbf{b}_4 + \mathbf{b}_5 + \mathbf{b}_6}{4}. \tag{4.28}$$

The divergence of $\mathbf{f}_{\mathbf{BE}}$ is $\nabla_S \cdot \mathbf{f}_{\mathbf{BE}}(\mathbf{r}) = \frac{\pm 1}{4\det(\mathbf{j}_{\boldsymbol{x}})}$, where "+" is adopted for $\mathbf{r} \in \boldsymbol{\theta}, \boldsymbol{\epsilon}, \boldsymbol{\eta}, \boldsymbol{\zeta}$ with $\boldsymbol{x}$ referring to any of the eight barycentric quadrilaterals.Each of the barycentric quadrilaterals $\boldsymbol{\alpha}, \boldsymbol{\beta}, \boldsymbol{\gamma}, \boldsymbol{\delta}$ contains a charge of value 1, and each of the barycentric quadrilaterals $\mathbf{r} \in \boldsymbol{\theta}, \boldsymbol{\epsilon}, \boldsymbol{\eta}, \boldsymbol{\zeta}$ has a charge of value -1. The PBF denotes a current flow starting from edge **AF**, passing **BE** and terminating at **CD**. It gives no fictitious line charge, therefore, it is suitable for representing surface current densities on quadrilaterals. It is noted that for purely quadrilateral meshes, if DBFs are not invoked, Eq. (4.27) could be substituted by BFs defined on initial quadrilaterals. However, Eq. (4.27) is very useful when the impedance matrix for the bQBFs is available.

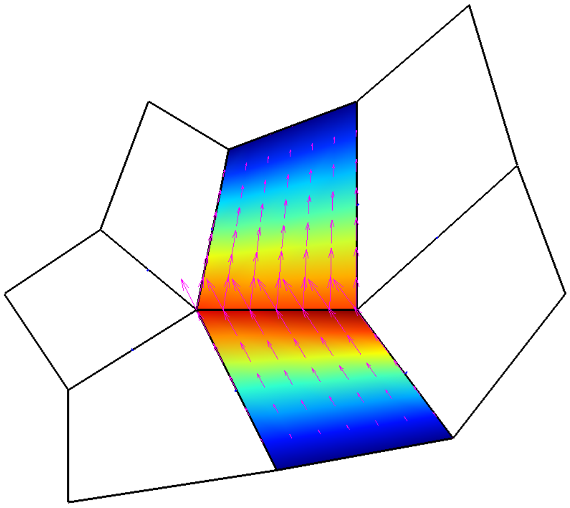

Figure 4.5: A PBF in a quadrilateral mesh. The color shows the magnitude of the PBF. Red color denotes larger values and blue color indicates smaller values.

4.5.2 Triangular meshes

Here we define a BF that is very similar to RWG, yet it is slightly different.

$$\mathbf{f}_{\mathbf{DB}} = c_3(\mathbf{b}_1 + \mathbf{b}_2) + c_4(\mathbf{b}_3 + \mathbf{b}_4 + \mathbf{b}_5 + \mathbf{b}_6), \tag{4.29}$$

where $\mathbf{b}_1$ through $\mathbf{b}_6$ are bQBFs defined in Eq. (4.20) associated with the barycentric edges 1 through 6 belonging to the two triangles in Fig. 4.6, and the red arrows denote their directions. The edges $\mathbf{IK}, \mathbf{KJ}$ are not used because they are perpendicular to $\mathbf{DB}$. The other edges such as $\mathbf{AE}, \mathbf{EB}, \mathbf{BF}, \mathbf{FC}, \mathbf{CG}, \mathbf{GD}, \mathbf{DH}, \mathbf{HA}$ are not included. The coefficients of $\mathbf{b}_1$ and $\mathbf{b}_2$ have to be equal due to symmetry. We simply let $c_3 = \frac{1}{2}$. The coefficients of $\mathbf{b}_3, \mathbf{b}_4, \mathbf{b}_5, \mathbf{b}_6$ are also identical. To determine c_4, we can enforce the condition that the quadrilaterals $\boldsymbol{\alpha}, \boldsymbol{\beta}$ have the same charge, i.e. $c_3 - c_4 = 2c_4$. So, $c_4 = \frac{1}{6}$. The whole expression is then:

$$\mathbf{f}_{\mathbf{DB}} = \frac{\mathbf{b}_1 + \mathbf{b}_2}{2} + \frac{\mathbf{b}_3 + \mathbf{b}_4 + \mathbf{b}_5 + \mathbf{b}_6}{6}. \tag{4.30}$$

The divergence is $\nabla_S \cdot \mathbf{f}_{\mathbf{DB}}(\mathbf{r}) = \frac{\pm 1}{3\det(\mathbf{j}_{\boldsymbol{x}})}$, where "+" is adopted for $\mathbf{r} \in \boldsymbol{\alpha}, \boldsymbol{\beta}, \boldsymbol{\gamma}$ and "−" is for $\mathbf{r} \in \boldsymbol{\delta}, \boldsymbol{\epsilon}, \boldsymbol{\zeta}$ with $\boldsymbol{x}$ referring to six barycentric quadrilaterals. The PBF is divergence conforming. It has a constant normal component on $\mathbf{DB}$ and zero normal components on the boundary edges $\mathbf{AB}$, $\mathbf{BC}$, $\mathbf{CD}$, $\mathbf{DA}$. Different from

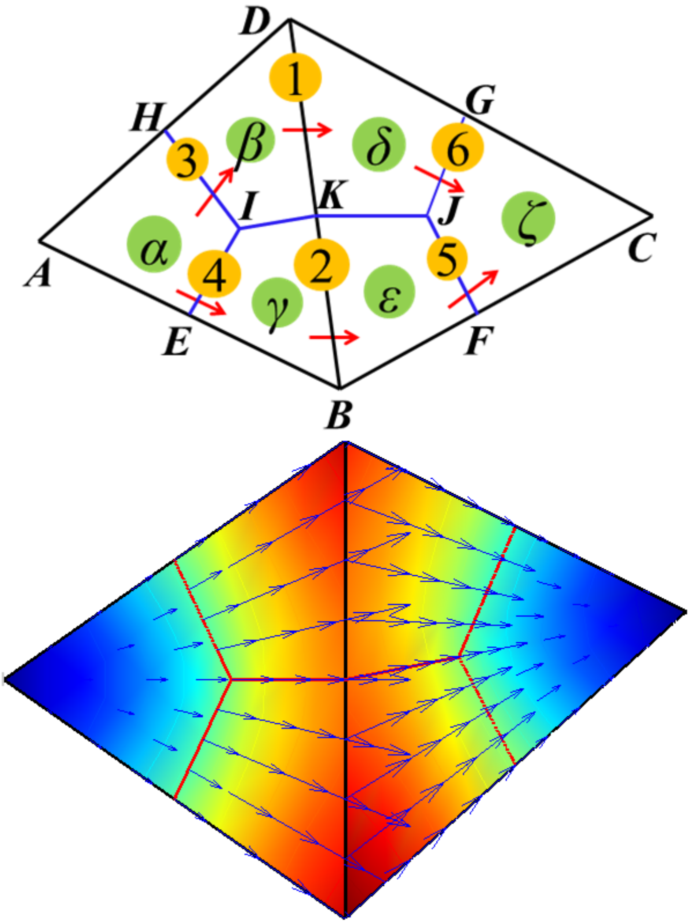

Figure 4.6: A PBF associated with **BD**, resides on two adjacent initial triangles $T_1(\mathbf{ABD})$ and $T_2(\mathbf{BCD})$, which are divided into barycentric quadrilaterals. It is a linear combination of six QBFs ($\mathbf{b}_1$ through $\mathbf{b}_6$) denoted by red arrows.

their counterparts on quadrilaterals, each barycentric quadrilateral on triangles has charge $\frac{4}{3}$ or $-\frac{4}{3}$. Similar to PBFs on quadrilaterals 4.4, the total charge on the triangle T_1 and T_2 is 4 and -4, respectively. The PBF Eq. (4.29) possesses properties making it suitable to represent currents on triangulated surfaces.

It is very similar to a pRWG associated with edge **DB**. However, there are also some differences. First, the RWG-BFs cannot be reconstructed by using the QBFs in Fig. 4.6. This can be observed from the fact that the divergence of a pRWG is a constant, but the divergence of the new PBF depends on the Jacobian, which is not a constant even for barycentric quadrilaterals on equilateral triangles.

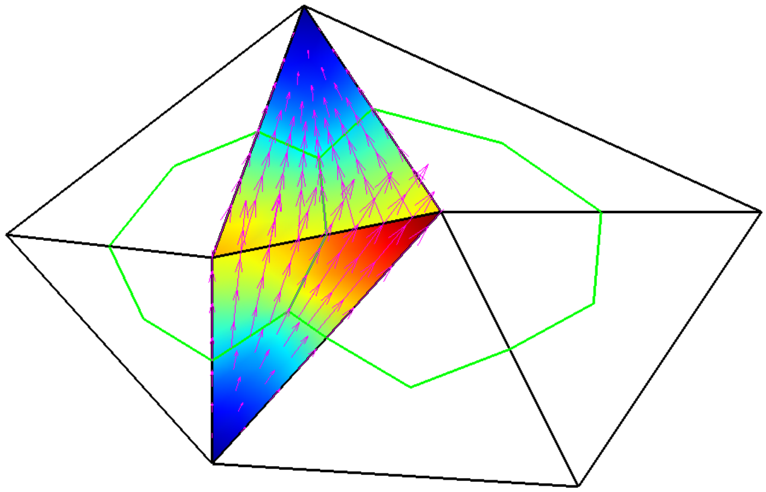

Figure 4.7: A PBF in a triangular mesh.

Second, there are discontinuities in the new PBF within each triangle. However, since the discontinuities only occur along tangential directions, fictitious line charge is absent. We indeed verified that the errors of using our PBFs and RWG-BFs in representing surface currents are very similar. We further note that the purpose of the new PBFs on triangles is not to replace the RWG-BFs but to enable efficient handling of mixed meshes and to facilitate implementation of CMP techniques for such meshes.

4.5.3 Mixed meshes

Combining the definitions of PBFs for pure quadrilaterals and triangles leads to the definition of PBFs on mixed meshes. This is possible because in either quadrilateral or triangular elements the normal component has a constant value on the shared boundary edge. The definition of PBFs from bQBFs can be accomplished by using an $N_b \times N_E$ sparse projection matrix $\mathbb{P}_1$, which has six nonzero elements in each column. The expression for the edge **BD** reads:

$$\mathbf{f}_{\mathbf{BD}} = \frac{\mathbf{b}_1 + \mathbf{b}_2}{2} + \frac{\mathbf{b}_3 + \mathbf{b}_4}{4} + \frac{\mathbf{b}_5 + \mathbf{b}_6}{6} \tag{4.31}$$

where $\mathbf{b}_1$ through $\mathbf{b}_6$ are bQBFs defined in Eq. (4.20) associated with the barycentric edges 1 through 6 belonging to the two triangles in Fig. 4.9.

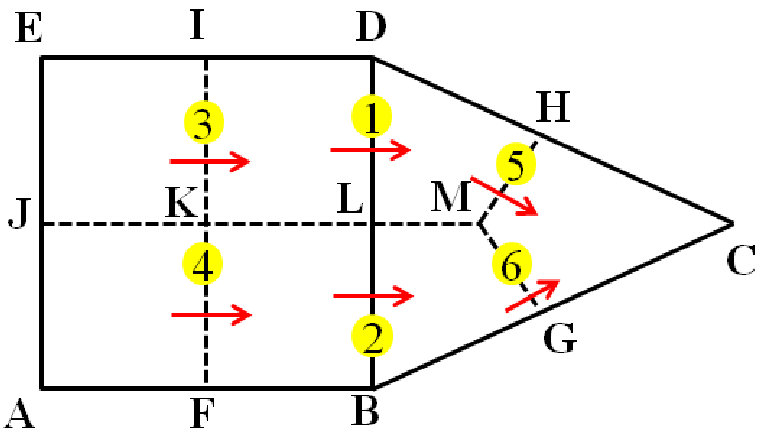

Figure 4.8: A PBF in a mixed mesh. The quadrilateral is **ABDE**, the triangle is **BCD**. The quadrilateral is divided into four smaller quadrilaterals.

We have discussed the how to construct PBFs using the barycentric mesh resulting from dividing a polygon into multiple quadrilaterals. The bQBFs give rise to a larger degree of freedom. The benefits are not clear until the DBFs are invoked.

4.6 Dual basis functions

Dual basis functions (DBFs) are discussed in this section. There are three types of DBFs, which are shown below.

4.6.1 Definition of DBFs

In defining DBFs, we do not need to distinguish whether the initial mesh comprises triangular, quadrilateral, or mixed elements because in every scenario the barycentric mesh contains only barycentric quadrilaterals. Henceforth, the DBFs can be defined uniformly for all situations. The DBF for a quadrilateral mesh is shown in Fig. 4.10. The DBT are supported by two polygons. The first polygon is **ONABCDEFGH**, the second is **OHIJKLMN**, they are separated by two edges **NO** and **HO**, which are indicated by dashed lines. In this case $N_{i1} = 5$, $N_{i2} = 4$.

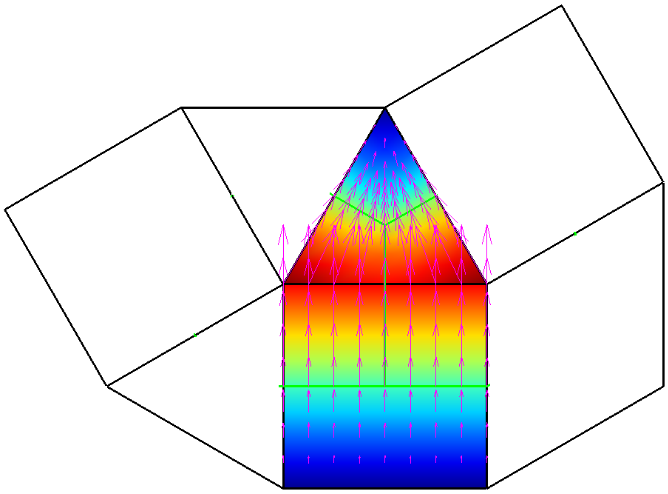

Figure 4.9: A PBF in a mixed mesh. The PBF resides on a quadrilateral patch and a triangle.

Consider the i-th internal edge $\mathbf{O}_1\mathbf{O}_2$. $\mathbf{O}_1$ is the left vertex and $\mathbf{O}_2$ is the right vertex. The numbers of initial elements around the two vertices are N_{i1} and N_{i2}, respectively. The reference PBF $f_{\mathbf{O}_1\mathbf{O}_2}(\mathbf{r})$ is perpendicular to the edge $\mathbf{O}_1\mathbf{O}_2$, the DBF should be orthogonal to it; therefore, we need to form a vector function that is parallel to $\mathbf{O}_1\mathbf{O}_2$. To satisfy this condition, the bQBFs $\mathbf{f}^{bQBF}_{\mathbf{OO}_1}, \mathbf{f}^{bQBF}_{\mathbf{OO}_2}$ must be discarded, and $\mathbf{f}^{bQBF}_{\mathbf{OH}}$ and $\mathbf{f}^{bQBF}_{\mathbf{ON}}$ should be included. All other edges indicated by the blue thick lines are not contained. The DBF is exactly the aforementioned PBF defined on the two polygons. The bQBFs are numbered in Fig. 4.11, and oriented counterclockwisely. The DBF can be partitioned into two parts, i.e. $\mathbf{F}_i = \mathbf{F}_i^{\text{left}} + \mathbf{F}_i^{\text{right}}$.

$$\begin{aligned} \mathbf{F}_{\text{left}} &= \mathbf{b}_{0_+} + \sum_{k=1}^{k=N_{i1}-1} \left(1 - \frac{2k}{N_{i1}}\right) \mathbf{b}_k, \\ \mathbf{F}_{\text{right}} &= -\mathbf{b}_{0_-} - \sum_{k=-(N_{i2}-1)}^{k=-1} \left(1 + \frac{2k}{N_{i2}}\right) \mathbf{b}_k. \end{aligned} \tag{4.32}$$

The coefficients are chosen by enforcing the total charge inside each barycentric quadrilateral to be a constant, while maintaining a symmetry. If N_{i1} or N_{i2} is an even number, there is a coefficient whose value is 0. Fig. 4.11 shows a DBF on a

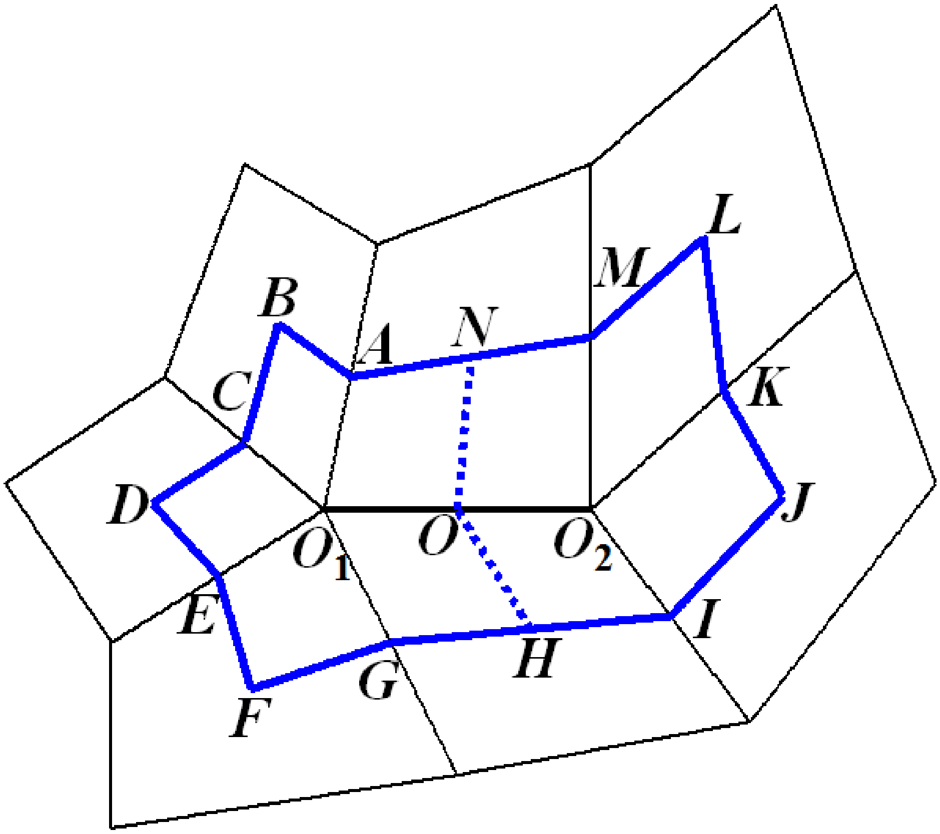

Figure 4.10: Two polygons on a quadrilateral mesh. The black thin lines form the original quadrilateral mesh. The referenced edge is $\mathbf{O}_1\mathbf{O}_2$. The thick blue lines form two polygons.

quadrilateral mesh, it can be written as

$$\mathbf{F}^{DBF}_{Quad} = \mathbf{b}_{0_+} + \frac{3}{5}\mathbf{b}_1 + \frac{1}{5}\mathbf{b}_2 - \frac{1}{5}\mathbf{b}_3 - \frac{3}{5}\mathbf{b}_4 - \mathbf{b}_{0_-} - \frac{1}{2}\mathbf{b}_{-1} - \frac{0}{4}\mathbf{b}_{-2} + \frac{1}{2}\mathbf{b}_{-3}. \quad (4.33)$$

Eq. (4.33) is a DBF that satisfies all the conditions. The vector plot of this DBF is also shown in Fig. 4.11.

The DBF on a triangular mesh is not very different from that on a quadrilateral mesh. The triangles in Fig. 4.12 has eight triangles in the left polygon ($N_{i1} = 8$), and seven triangles in the right polygon ($N_{i1} = 7$). The left polygon is formed by vertices $\mathbf{O}_0$**ABCDEFGHIJKLMNO**, its center is $\mathbf{O}_1$. The right polygon is centered at $\mathbf{O}_2$, formed by vertices $\mathbf{O}_0$**OPQRSTUVWXYZA**. The two polygons are separated by edges $\mathbf{O}_0\mathbf{A}$ and $\mathbf{O}_0\mathbf{O}$. The DBF follows the expression

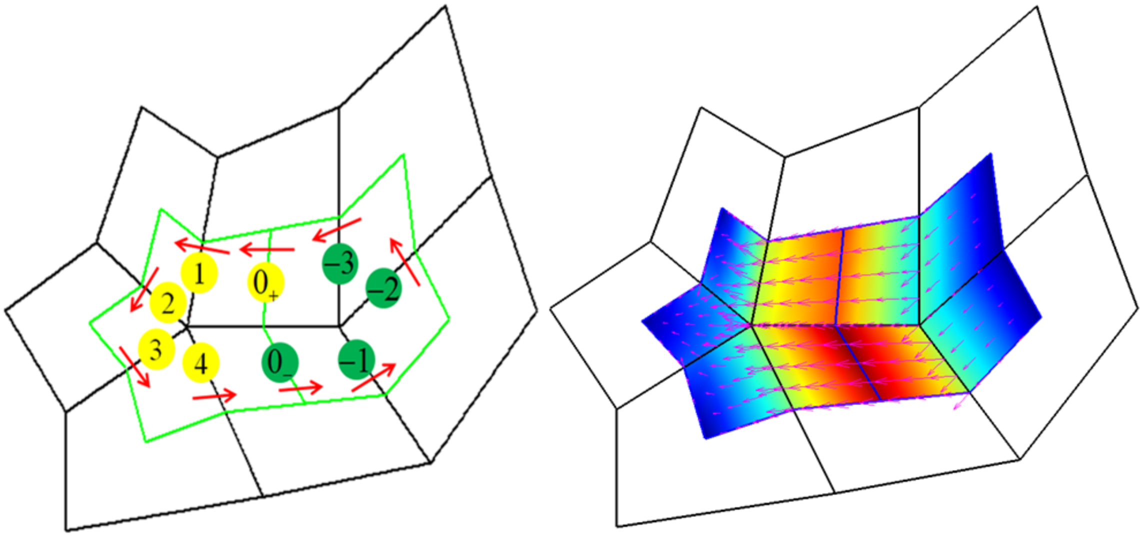

Figure 4.11: A DBF on a quadrilateral mesh. The DBF is approximated parallel to the referenced edge $\mathbf{O}_1\mathbf{O}_2$ (This edge has been shown in Fig. 4.10). This DBF is the summation of eight bQBFs. The coefficient of the bQBF numbered -2 is zero.

Eq. (4.33), and it is written as:

$$\begin{aligned}\mathbf{F}^{DBF}_{Tri} = \mathbf{b}_{0_+} + \frac{3}{4}\mathbf{b}_1 + \frac{1}{2}\mathbf{b}_2 + \frac{1}{4}\mathbf{b}_3 + \frac{0}{8}\mathbf{b}_4 - \frac{1}{4}\mathbf{b}_5 - \frac{1}{2}\mathbf{b}_6 - \frac{3}{4}\mathbf{b}_7 \\ -\mathbf{b}_{0_-} - \frac{5}{7}\mathbf{b}_{-1} - \frac{3}{7}\mathbf{b}_{-2} - \frac{1}{7}\mathbf{b}_{-3} - \frac{1}{7}\mathbf{b}_{-4} + \frac{3}{7}\mathbf{b}_{-5} + \frac{5}{7}\mathbf{b}_{-6}.\end{aligned} \tag{4.34}$$

This DBF has 15 bQBFs, but one of them has a zero coefficient. The coefficients ensures that each quadrilateral in the right polygon has equal positive charge, and that in the left polygon has equal negative charge. This DBF is very interesting in the sense that, although the original mesh is triangular, but the ingredient of this DBF is not RWG-BFs but the bQBF. The RWG-BFs can form the DBF, but the number of RWG-BFs is 30, which is more complex and difficult to implement. On the other hand, the quadrilateral can be divided into eight triangles, where RWG-BFs can be used to define the DBFs. But this way makes the implementation much more complex, and loses the good properties of the QBFs. The same procedure applies to a mixed mesh, shown in Fig. 4.14. The left polygon is formed by vertices $\mathbf{O}_0\mathbf{ABCDEFGHI}$, its center is $\mathbf{O}_1$. The right polygon is formed by vertices $\mathbf{O}_0\mathbf{IJKLMNA}$, its center is $\mathbf{O}_2$. The two polygons

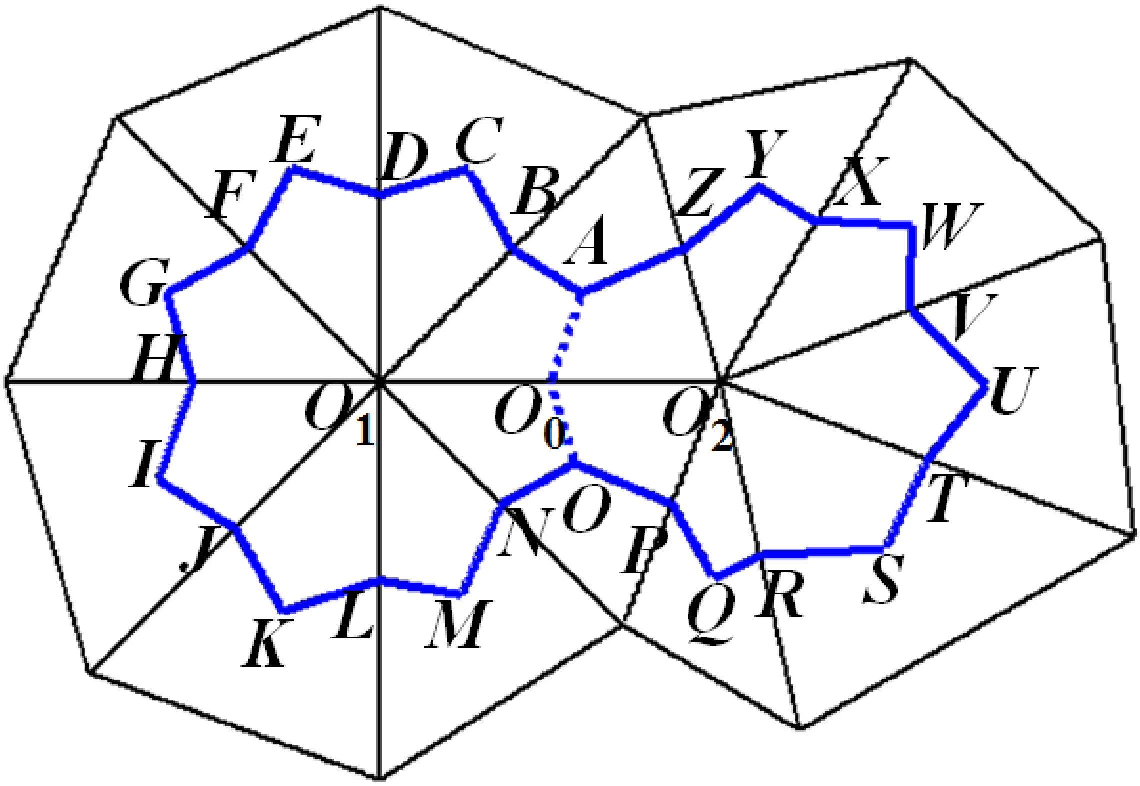

Figure 4.12: Two polygons on a triangular mesh. The triangles are denoted by solid black thin lines. The referenced edge is $\mathbf{O}_1\mathbf{O}_2$. The polygons formed by dividing each triangle into three quadrilaterals are indicated by blue thick lines.

are separated by edges $\mathbf{O}_0\mathbf{A}$ and $\mathbf{O}_0\mathbf{I}$. In the following case, the DBF reads:

$$\mathbf{F}^{DBF}_{Mixed} = \mathbf{b}_{0_+} + \frac{3}{5}\mathbf{b}_1 + \frac{1}{5}\mathbf{b}_2 - \frac{1}{5}\mathbf{b}_3 - \frac{3}{5}\mathbf{b}_4 - \mathbf{b}_{0_-} - \frac{2}{4}\mathbf{b}_{-1} - \frac{0}{4}\mathbf{b}_{-2} + \frac{2}{4}\mathbf{b}_{-3}. \quad (4.35)$$

The subdivided quadrilaterals that form a polygon are not necessarily coplanar. In the really cases, almost no polygon is planar for the curved surfaces.

4.6.2 Discussions on DBFs

We have seen that the idea of DBF relies on the polygons. The original elements (e.g. triangles and quadrilaterals) have no overlaps. Similarly, the polygons, formed by barycentrically dividing the original mesh, have no collisions. We can see the combination of the polygons is identical to the collection of the original

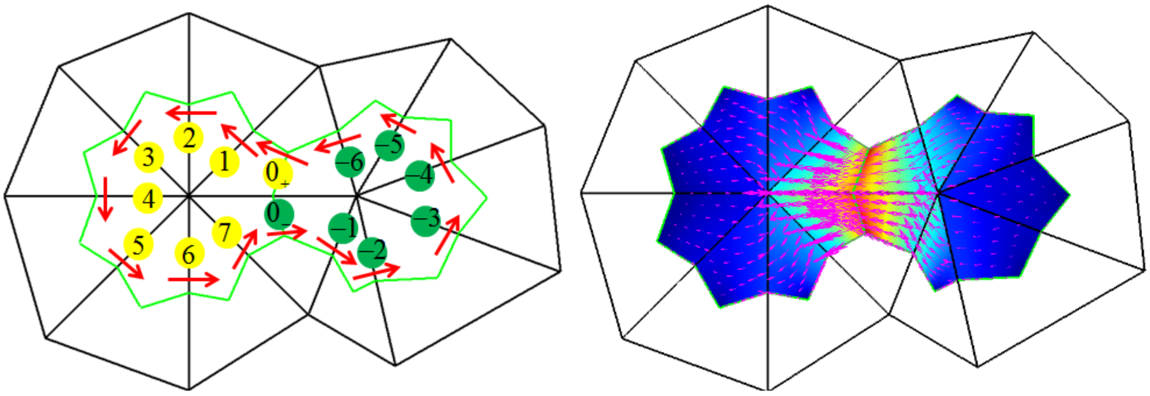

Figure 4.13: A DBF on a triangular mesh. The vector plots shows the direction and magnitude of the DBF, which is parallel to the referenced edge.

triangles and quadrilaterals: $\cup_{n=1}^{n=N_T} T_n \cup_{n=1}^{n=N_Q} Q_n = \cup_{n=1}^{n=V} P_n$. The number of edges in the polygonal mesh[2] is the same as that in the original mesh.

Each internal edge is assigned a PBF and a DBF. While the PBF is approximately perpendicular to reference edge, the DBF denotes a current flow quasi-parallel to it. The support of a DBF is divided into two polygons separated by the two barycentric edges 0_+ and 0_-. The left polygon contains only negative charge and the right one has positive charge. The total charges in the left and right polygons are -8 and 8 respectively. Each barycentric quadrilateral in the left polygon has charge $-\frac{8}{N_{i1}}$ and that in the right polygon has $\frac{8}{N_{i2}}$. Each RWG or new PBF straddles two adjacent initial elements. In contrast, each of the new introduced DBF is supported by two polygons formed by barycentric triangles or quadrilaterals, respectively. On a large smooth surface, if meshed into triangles, most of the vertices have six surrounding triangles. On the other hand, if meshed into quadrilaterals, each vertex has about four vertices. Therefore, roughly speaking, the duals of triangles are hexagons, and the duals of quadrilaterals are still quadrilaterals. In particular, for a planar mesh consisting of identical parallelograms, the polygons for DBFs are still parallelograms of the same shape. As an exam-

---

[2] The number of edges in a polygon is defined as the number of elements that the polygon resides on. This definition seems slightly strange. For instance, the left polygon in Fig. 4.10 seems to have 10 edges, but in our definition, it has only 5 edges, because the edges such as **OH** and **ON** occur simultaneously.

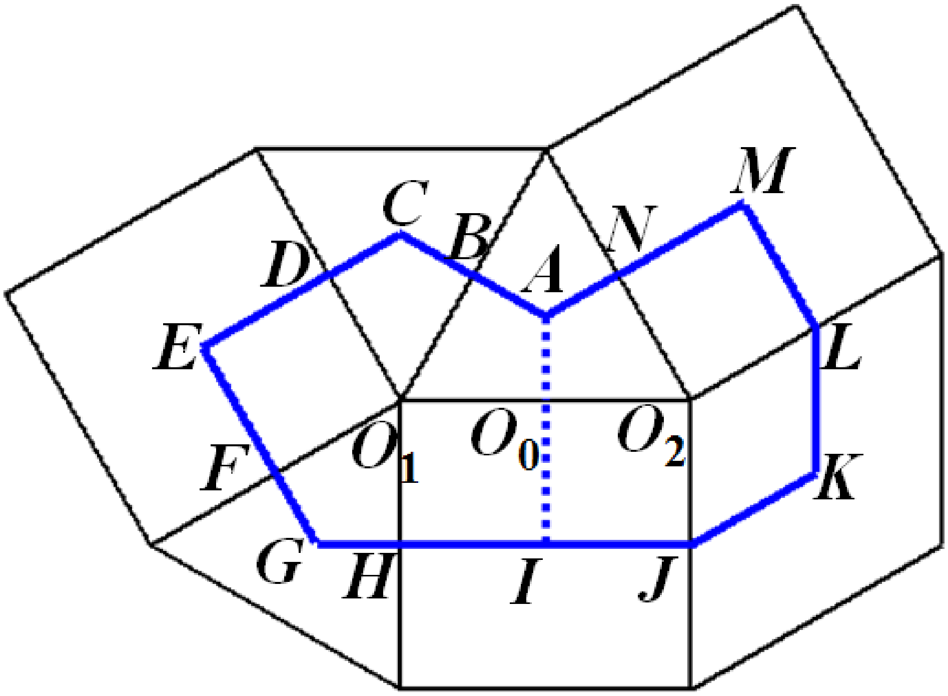

Figure 4.14: Two polygons on a mixed mesh. The original triangles and quadrilaterals are denoted by black thin lines. The polygons formed by dividing each triangle into three quadrilaterals are indicated by blue thick lines.

ple, the DBF of a rooftop BF is still rooftop. The introduced DBFs for triangles are built on the same polygons as BCBFs. However, BCBFs require polygons to be partitioned into barycentric triangles, and the new DBFs need polygons to be divided into barycentric quadrilaterals. This is ascribed to the introduced QBMs and QBBFs. The introduced DBFs on triangular meshes can be used as duals not only for the PBFs (29), but also for RWG-BFs. Applying Eulers polyhedral formula for a simply connected closed surface, one has $N_V + N_T + N_Q - N_E = 2$, where N_T and N_Q are the numbers of triangles and quadrilaterals, respectively. Pure triangular or quadrilateral meshes can be regarded as special cases of mixed meshes by letting $N_Q = 0$ or $N_T = 0$. According to the Loop-Star decomposition definitions [113, 114, 108], the total number of independent loop (solenoidal) BF-s comprised of PBFs is $N_V - 1$, and the total number of independent loop BFs composed of DBFs is $N_T + N_Q - 1$. Therefore we have (5.9) automatically enforced.

Consider a closed surface of area S. Suppose the surface is meshed into

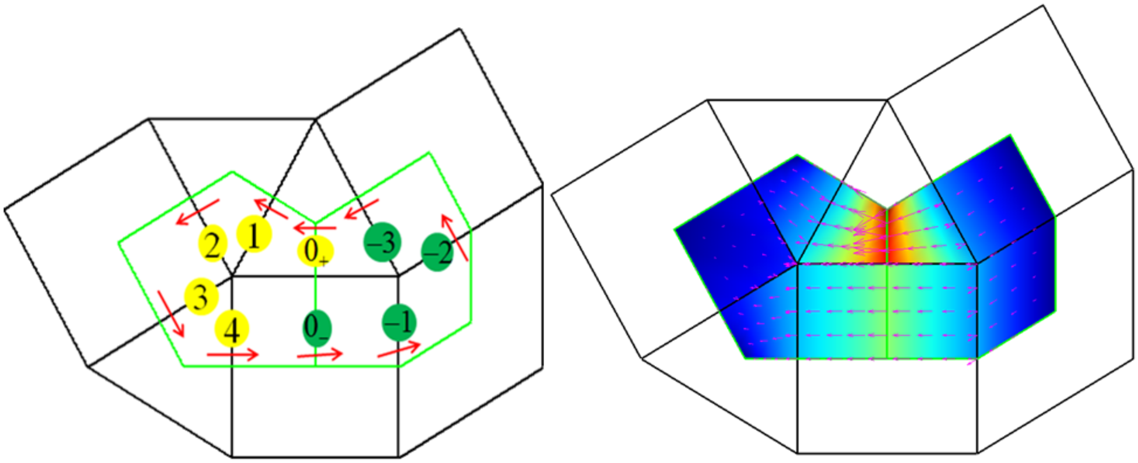

Figure 4.15: A DBF on a mixed mesh. The left polygon is residing on three triangles and two quadrilaterals, the right polygon is defined over one triangle and three quadrilaterals.

triangles only, with an average mesh size of δ, leading to $N_E \approx \frac{2\sqrt{3}S}{\delta^2}$, $N_b \approx \frac{12\sqrt{3}S}{\delta^2}$. For the same structure discretized into an all-quadrilateral mesh, one has $N_E \approx \frac{2S}{\delta^2}$, $N_b \approx \frac{8\sqrt{3}S}{\delta^2}$. On a typical quadrilateral mesh, each vertex is surrounded by 4 quadrilaterals and, accordingly, most of the DBFs contain only 6 QBBFs. On the other hand a typical BCBF consists of 24 bRWG-BFs. Therefore, using quadrilateral meshes results in a substantially reduced number of PBFs, DBFs, and barycentric BFs.

Each initial triangle, if divided into three barycentric quadrilaterals, needs at least three equally weighted quadrature points; whereas if partitioned into six barycentric triangles, it requires at least six quadrature points. The reduction in the number of quadrature nodes reduces the computational cost of CMPs.

Overlapped RWG and BCBFs on triangles cannot achieve exact orthogonality, even for equilateral triangles. However, rectangles as special quadrilaterals yield the exact orthogonality, and for large smooth surface most of the quadrilaterals can have a nearly perfect rectangular shape.

4.7 Helmholtz decompositions of vector field on a surface

Suppose $\mathbf{j}$ is a tangential vector field on a closed and simply connected smooth surface Γ, $\mathbf{j}$ may have three components:

$$\mathbf{j} = \mathbf{j}_S + \mathbf{j}_I + \mathbf{j}_H, \tag{4.36}$$

where $\mathbf{j}_S$ ($\nabla_S \cdot \mathbf{j}_S = 0, \nabla_S \times \mathbf{j}_S \neq \mathbf{0}$) is the solenoidal part, $\mathbf{j}_I$ ($\nabla_S \cdot \mathbf{j}_I \neq 0, \nabla_S \times \mathbf{j}_I = \mathbf{0}$) is the irrotational part, and $\mathbf{j}_H$ ($\nabla_S \cdot \mathbf{j}_H = 0, \nabla_S \times \mathbf{j}_H = \mathbf{0}$) is the harmonic component. Eq. (4.36) is very similar to the Helmholtz decomposition for volumetric vector fields. But there are also appreciable differences. For instance, the curl operator in three dimensional space is a vector operator intrinsically since the resulting vector can point to any direction. The surface unit normal vector is $\hat{\mathbf{n}}$. The surface curl $\nabla_S \times$ only points in $\hat{\mathbf{n}}$ direction. So $\nabla_S \times$ is essentially a scalar operator. It can be verified:

$$\begin{aligned} &\nabla_S \cdot (\hat{\mathbf{n}} \times \mathbf{j}_S) = \hat{\mathbf{n}} \cdot \nabla_S \times \mathbf{j}_S, \nabla_S \times (\hat{\mathbf{n}} \times \mathbf{j}_S) = \mathbf{0}, \\ &\nabla_S \cdot (\hat{\mathbf{n}} \times \mathbf{j}_I) = \mathbf{0}, \nabla_S \times (\hat{\mathbf{n}} \times \mathbf{j}_I) = (\nabla_S \cdot \mathbf{j}_I)\hat{\mathbf{n}}, \end{aligned} \tag{4.37}$$

From Eq. (4.37), it follows that $\mathbf{j}_S$ and $\mathbf{j}_I$ are completely *dual* to each other. They can be converted by rotating 90 degrees through the $\hat{\mathbf{n}}\times$ operation. The Helmholtz decomposition is important, since in the EFIEs, the surface charge density is related to the divergence of the current, i.e. $\nabla_S \cdot \mathbf{j} = i\omega\rho_S$. Since $\nabla_S \cdot \mathbf{j} = \nabla_S \cdot \mathbf{j}_I$, the two components $\mathbf{j}_S$ and $\mathbf{j}_H$ have no contribution to the surface charge. On a planar surface, $\mathbf{f}_1 = \hat{\mathbf{x}}x + \hat{\mathbf{y}}y$ is an irrotational part, since $\nabla_S \cdot \mathbf{f}_1(\mathbf{r}) = 2, \nabla_S \times \mathbf{f}_1(\mathbf{r}) = \mathbf{0}$. On the other hand, $\mathbf{f}_2 = -\hat{\mathbf{x}}y + \hat{\mathbf{y}}x$ is a solenoidal part, since $\nabla_S \cdot \mathbf{f}_2(\mathbf{r}) = 0, \nabla_S \times \mathbf{f}_2(\mathbf{r}) = 2\hat{\mathbf{z}}$. The curl of an RWG-BF is always zero. But the curl of an QBF is zero only if it is a parallelogram.

Consider a mixed triangular and quadrilateral mesh with E edges, F faces and V vertices [115, 116, 117]. If the number of genera is g, the number of independent harmonic fields is $2g$. The number of PBFs or DBFs is E. To represent $\mathbf{J}_I$, $\mathbf{J}_S$ and $\mathbf{J}_H$, the v-BFs are combined to form star BFs (SBFs), Local Loop BFs (LLBFs) and Global Loop BFs (GLBFs). There are $F-1$ SBFs, $V-1$ LLBFs, and

$2g$ GLBFs, corresponding to $\mathbf{j}_I$, $\mathbf{j}_S$, and $\mathbf{j}_H$, respectively. Each SBF is associated

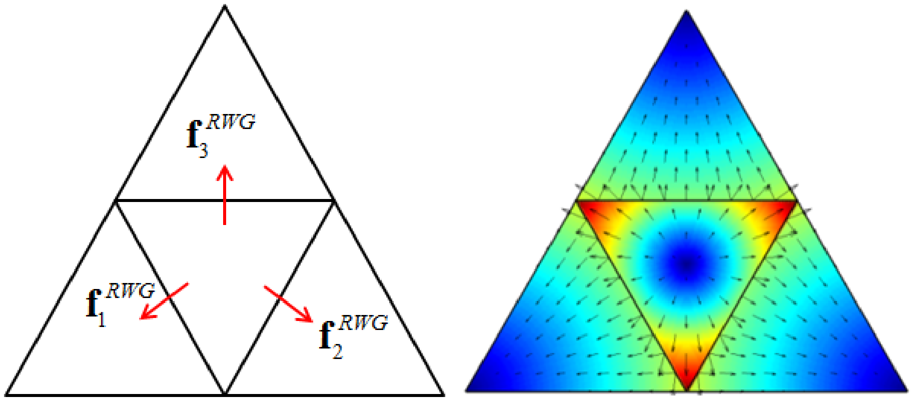

Figure 4.16: Vector plot of the SBF associated with a triangle, $\mathbf{f}_{SBF} = \sum_{i=1}^{i=3} \mathbf{f}_i^{RWG}$. The color denotes the magnitudes of the vector fields.

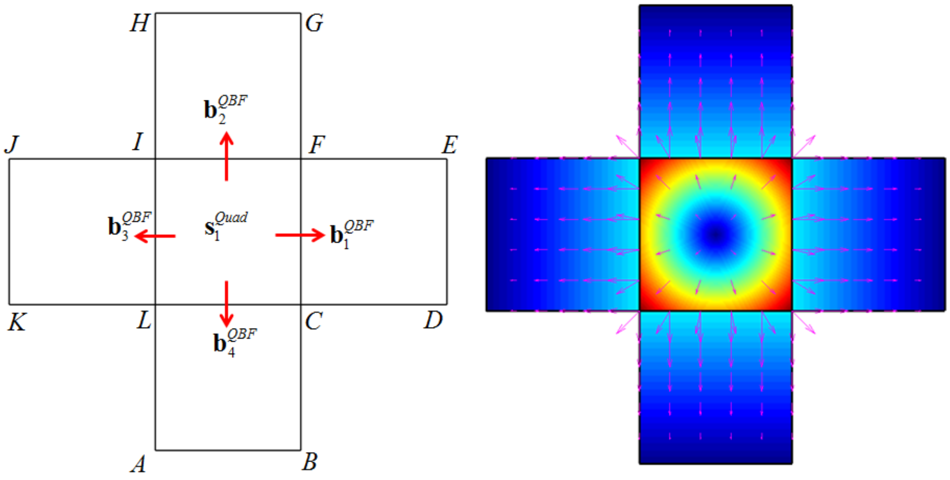

Figure 4.17: Vector plot of the SBF associated with a quadrilateral, $\mathbf{f}_{SBF} = \sum_{i=1}^{i=4} \mathbf{b}_i^{QBF}$. The color denotes the magnitudes of the vector fields.

with a patch (i.e. a triangle or a quadrilateral), and has three or four v-BFs. The physical meaning of an SBF is a radial current flowing out of the referenced patch [118, 115]. An integer matrix $\mathbb{S} \in \mathbb{N}^{E\times(F-1)}$ is used to map the BFs onto the SBFs. Each column of $\mathbb{S}$ has only three or four nonzero elements whose values can be only ± 1. Moreover, let $\mathbb{D}_{\mathbb{S}} = \mathbb{S}^T\mathbb{S}$, it is the graph Laplacian. $\mathbb{D}_{\mathbb{S}}$ is a high sparse, positive definite, and ill-conditioned matrix. Its off-diagonal nonzero elements are -1. Its diagonal elements are positive integers. If the i^{th} patch is a triangle, $(\mathbb{D}_\mathbb{S})_{ii} = 3$. Otherwise if it is a quadrilateral, $(\mathbb{D}_\mathbb{S})_{ii} = 4$. As a diagonal dominant matrix. $\mathbb{D}_\mathbb{S}$ is positive definite, and its condition number scales $\mathcal{O}(1/h^2)$, where h is the mesh size. Although $\mathbb{D}_\mathbb{S}$ has bad conditioning for large problems, an iterative solution of a linear equation $\mathbb{D}_\mathbb{S}\boldsymbol{x} = \boldsymbol{b}$ $(\boldsymbol{x}, \boldsymbol{b} \in \mathbb{C}^{(F-1)\times 1})$ takes only an $\mathcal{O}(E)$ cost by using efficient multigrid preconditioners.

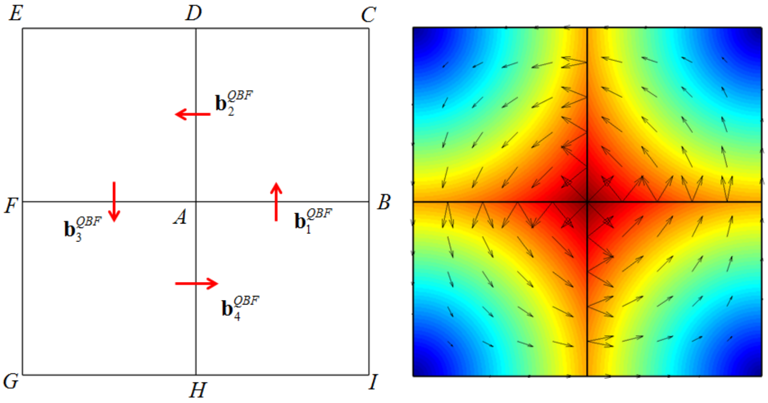

Figure 4.18: Vector plot of the LLBF associated with a quadrilateral. The color denotes the magnitudes of the vector fields.

Each LLBF is associated a vertex. It represents a current flowing around a vertex. Define an integer matrix $\mathbb{L} \in \mathbb{N}^{E\times(V-1)}$ that projects the BFs onto the LLBFs. Similar to $\mathbb{S}$, $\mathbb{L}$ is very sparse and its nonzero elements can be only 1 or -1. The rank of $\mathbb{L}$ is $V-1$. It can be verified that $\mathbb{L}^T\mathbb{S} = \mathbb{O}$, indicating that each SBF is completely independent of any LLBF. Furthermore, let $\mathbb{D}_\mathbb{L} = \mathbb{D}_\mathbb{L}^T\mathbb{L}$, it is the Laplacian of the dual graph, which has similar properties as $\mathbb{D}_\mathbb{S}$. If the i^{th} vertex has V_i triangular or quadrilateral elements around it, then $(\mathbb{D}_\mathbb{L})_{ii} = V_i$. The RWG-BFs could be equally represented by the SBFs and LLBFs if there is no GLBF.

The DBFs can also form the SBFs or LLBFs. A SBF is formed by a several DBFs that share a common vertex. So the number of SBFs is $V-1$. It denotes a current flowing out of the vertex. The DBFs also adopts a loop-star decomposition. The Star DBF is represented by a sparse matrix, and the number of independent

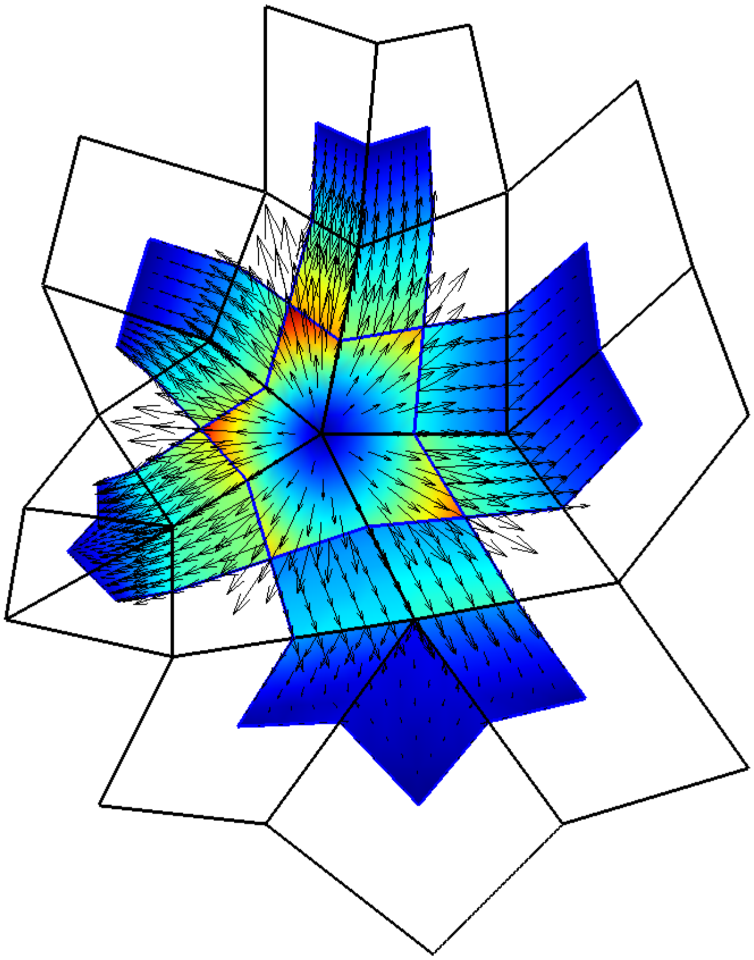

Figure 4.19: A SBF formed by five DBFs. The star BF represents a radial shaped current flowing out of the central polygon. This SBF is the summation of five DBFs that share the central polygon.

Star DBF is $V-1$. The Star DBFs yield a graph Laplacian. It is the same as $\mathbb{D}_{\mathbb{L}}$. In this sense, the SBF formed by the DBFs is *dual* to the LLBF of the PBFs. Around each triangle or quadrilateral there is a LLBF. The number of independent LLBFs formed by DBFs is $F-1$. The Local loop DBF is also indicated by a sparse matrix. The corresponding graph Laplacian is $\mathbb{D}_{\mathbb{L}}$.

The LLBF formed by the DBFs is *dual* or "orthogonal" to the SBFs constructed by the PBFs. The DBFs and the PBFs mutually complement each other's ability to expand electric or magnetic currents. These BFs seem to be quite com-

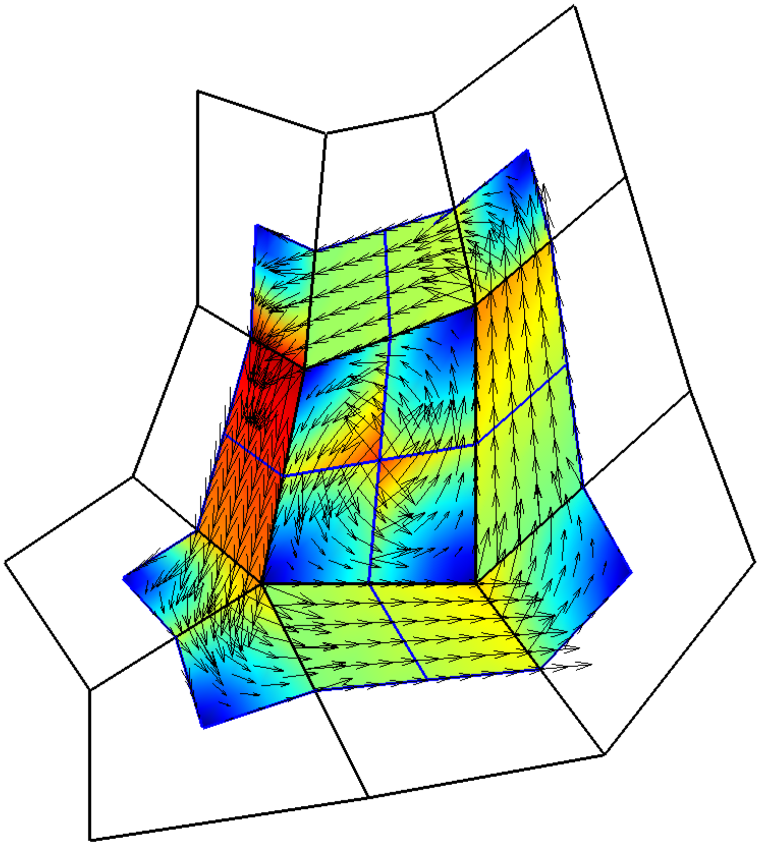

Figure 4.20: A loop BF formed by four DBFs. The loop BF depicts a circulating current flowing around the central quadrilateral. The divergence of the DBF is zero.

plex. But they are useful in accelerating the integral equations and improving the accuracy.

4.8 Global loop basis functions

The GLBF is not obvious, it does not exist on a plane or a sphere surface. But it can exist on a torus. A torus can be seen as a circular tube, whose cross section is a circle of radius r. The torus is parameterized as $\mathbf{r} = \hat{\mathbf{x}}(R + r\cos u)\cos v + \hat{\mathbf{y}}(R + r\cos u)\sin v + \hat{\mathbf{z}}r\sin u$, where R is the distance from the center of the torus to the center of the tube, $0 \leq u \leq 2\pi, 0 \leq v \leq \pi$. Two natural vectors are $\mathbf{r}_u = \frac{\partial \mathbf{r}}{\partial u} = -\hat{\mathbf{x}}r\sin u\cos v - \hat{\mathbf{y}}r\sin u\sin v + \hat{\mathbf{z}}r\cos u$ and

$\mathbf{r}_v = \frac{\partial \mathbf{r}}{\partial v} = -\hat{\mathbf{x}}(R + r\cos u)\sin v + \hat{\mathbf{y}}(R + r\cos u)\cos v$. The determinant of the Jacobian is $\det(\mathbf{j}) = |\mathbf{r}_u \times \mathbf{r}_v| = r(R + r\cos u)$. A unit vector normal to the surface is $\hat{\mathbf{n}} = \hat{\mathbf{x}}\cos u\cos v + \hat{\mathbf{y}}\cos u\sin v + \hat{\mathbf{z}}\sin u$. Let $\mathbf{b}_1 = \frac{\mathbf{r}_u}{\det(\mathbf{j})}$, $\mathbf{b}_2 = \frac{r}{R+r\cos u}\frac{\mathbf{r}_v}{\det(\mathbf{j})}$. These two vector functions are harmonic field, i.e. $\nabla_S \cdot (c_1\mathbf{b}_1 + c_2\mathbf{b}_2) = 0, \nabla_S \cdot [\hat{\mathbf{n}} \times (c_1\mathbf{b}_1 + c_2\mathbf{b}_2)] = 0$, where c_1 and c_2 are arbitrary constants. Moreover, $\mathbf{b}_1 \cdot \mathbf{b}_2 = 0$. On the torus, there can be only two independent harmonic fields, all others are a linear combination of $\mathbf{r}_u$ and $\mathbf{r}_v$.

We have observed that, SBF and LLBF are associated with a vertex or a patch. One intriguing question is whether a GLBF is related to some geometric element of a mesh. Before answering this question, we first classify two kinds of circles on a surface. A circle on a surface mesh is a set of consecutive edges that form a closed loop. Here we consider only simple circles. A circle is simple in the sense that it does not intersect with itself. A simple circle on the mesh can be viewed as a set of N consecutive of edges. A circle C can be expressed as a column vector $\boldsymbol{c}$ of length E, each of $\boldsymbol{c}$'s element can be only 0, or ± 1.

4.8.1 Contractible Circles

If c is a contractible circle, it holds

$$\mathbb{L}^T \boldsymbol{c} = \mathbf{0}. \tag{4.38}$$

As shown in Fig. 4.21, the green edges numbered $1, 2, 3, 4, 5$ form a contractible circle. These edges are oriented such that they point outwards. The edges indicated by dashed arrows together with edges $4, 5$ constitute an LLBF. The overlapping between the circle and the LLBF includes edges $4, 5$. In the contractible circle, the coefficients of these two edges are both 1, but in the LLBF, the coefficient of edge 4 is 1, and that of edge 5 is -1. Consequently, the coefficient vector for this LLBF is orthogonal to that for the contractible circle. Eq. (4.38) is an orthogonality relationship, which can be verified easily. One can assert that circles are independent of the LLBFs. On the other hand,

$$\mathbb{S}^T \boldsymbol{c} \neq \mathbf{0}. \tag{4.39}$$

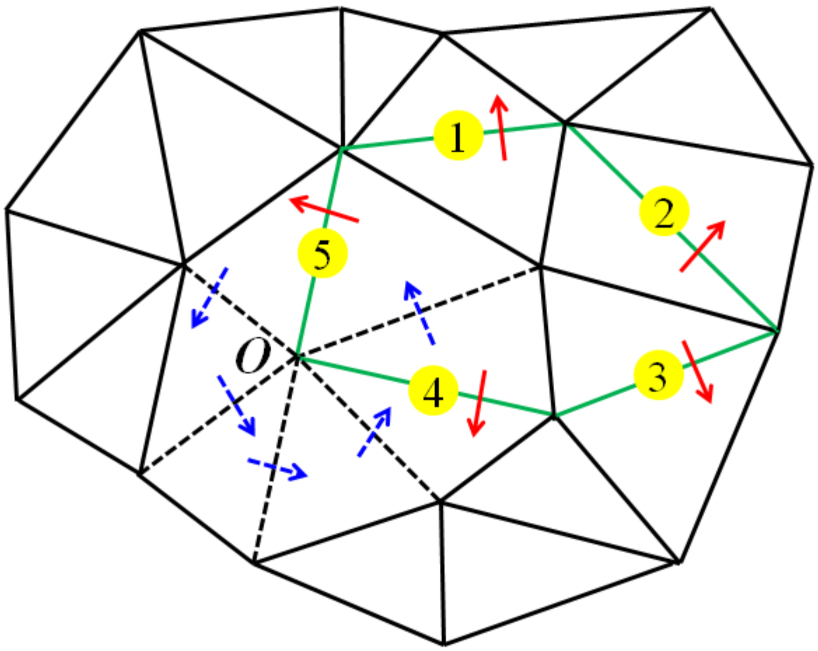

Figure 4.21: The Green lines numbered $1, 2, 3, 4, 5$ form a contractible circle. The dashed edge are used in an LLBF.

Eq. (4.39) dictates that the circle c may not be independent of SBFs. To see that if C is contractible, $\boldsymbol{c}$ is a linear combination of column vectors of $\mathbb{S}$, we observe that if all the SBFs associated with elements inside c have a coefficient 1, then the coefficients of the edges inside c vanishes, and only the boundary edges survive. Alternatively, we can let the coefficients of all SBFs associated with elements outside c to be 1, we get the same result.

4.8.2 Non-Contractible Circles

If C is a non-contractible circle, it cannot divide a surface into two disconnected parts, and it cannot be a linear combination of SBFs or LLBFs. Indeed, the non-contractible circles contain new information other than the SBFs. This can be proved by contradiction. If C is formed by N_C edges, $\boldsymbol{c}$ has N_C nonzero elements, assume that it is expressible as a sum of columns of matrix $\mathbb{S}$, i.e. $\boldsymbol{c} = \mathbb{S}\boldsymbol{a}$, where $\boldsymbol{a} \in \mathbb{R}^{(F-1)\times 1}$ is a nonzero column vector. Since all the other edges have a zero coef-

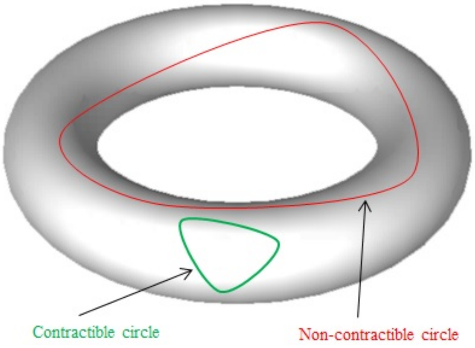

Figure 4.22: Contractible and Non-contractible circles. The Green line denotes a contractible circle, the red line indicates a non-contractible circle.

ficient, as a result, the SBFs on two sides of C have identical coefficients. Moreover, since all elements are connected, it follows that all SBFs in the mesh have identical coefficients, which can be 1. However, if this is true, the edges representing the non-contractible circles should also have zero coefficients, i.e. $\boldsymbol{c}$ is a zero vector, which is in a contradiction to our assumption. Therefore, $\boldsymbol{c}$ is not in the column span of $\mathbb{S}$. There are many kinds of non-contractible loops on a torus. For instance,

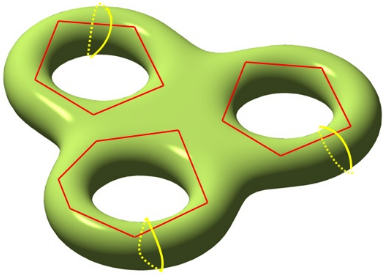

Figure 4.23: Non-contractible circles on the surface of a 3-torus. The red circles are used for poloidal GLBFs and the yellows are for toroidal GLBFs.

$\mathbf{r}(t) = \hat{\mathbf{x}}(R + r\cos(mt))\cos(nt) + \hat{\mathbf{y}}(R + r\cos(mt))\sin(nt) + \hat{\mathbf{z}}r\sin(mt), 0 \leq t < 2\pi$, where m, n are integers.

Ideal GLBFs are both (i) divergence-free and (ii) curl-free. In practice, when a vector field is represented by the curl-conforming v-BFs, they can strictly satisfy (i) but not (ii). Let $\mathbf{f}^{GLBF}$ denote a GLBF. It is a summation of the v-BFs, i.e. $\mathbf{f}^{GLBF}(\mathbf{r}) = \sum_{n=1}^{n=N_E} g_n \mathbf{b}_n(\mathbf{r})$. Here $\boldsymbol{g} = [g_1, g_2, \ldots, g_{N_E}]^T$ is a real-valued column vector containing the coefficients of the v-BFs that form a GLBF. It has two fundamental properties:

$$\mathbb{S}^T \boldsymbol{g} = \mathbf{0}, \mathbb{L}^T \boldsymbol{g} = \mathbf{0}, \tag{4.40}$$

Then $\boldsymbol{g}$ is in the nullspace of $\mathbb{P}$:

$$\mathbb{P} = \mathbb{S}(\mathbb{S}^T\mathbb{S})^{-1}\mathbb{S}^T + \mathbb{L}(\mathbb{L}^T\mathbb{L})^{-1}\mathbb{L}^T. \tag{4.41}$$

Eq. (4.41) points out one way to calculate $\boldsymbol{g}$, but the matrix inversions are not possible because of there prohibitively high cost $\mathcal{O}(N^3)$. We have noticed that the non-contractible circles has new information that is not contained by $\mathbb{S}$ or $\mathbb{L}$. Therefore, it is instrumental in determining the GLBFs. Here $\mathbb{P}$ is a dense and real-valued matrix. It is quite different from the matrices $\mathbb{S}$ and $\mathbb{L}$, which are are sparse and integer valued.

4.8.3 Algorithm

There are $2g$ independent non-contractible circles, which are denoted by an integer matrix $\mathbb{K} \in \mathcal{N}^{E\times 2g}$. The nonzeros of $\mathbb{K}$ are only ±1. The equation that determines a GLBF is:

$$\begin{pmatrix} \mathbb{L}^T \\ \mathbb{S}^T \\ \mathbb{K}^T \end{pmatrix} \boldsymbol{g} = \begin{pmatrix} \mathbf{0}_{\mathbb{L}} \\ \mathbf{0}_{\mathbb{S}} \\ \boldsymbol{e}_{\mathbb{K}} \end{pmatrix}, \tag{4.42}$$

where $\mathbf{0}_{\mathbb{L}}$ and $\mathbf{0}_{\mathbb{S}}$ are zero column vectors of length $V-1$ and $F-1$, $\boldsymbol{e}_{\mathbb{K}}$ is a column vector of length $2g$ with only 1 nonzero element. Let $\boldsymbol{g} = [\mathbb{L}, \mathbb{S}, \mathbb{K}]\,\boldsymbol{x}$. Here $\boldsymbol{x} = [\boldsymbol{x}_{\mathbb{L}}^T, \boldsymbol{x}_{\mathbb{S}}^T, \boldsymbol{x}_{\mathbb{K}}^T]$. $\boldsymbol{x}_{\mathbb{L}}, \boldsymbol{x}_{\mathbb{S}}, \boldsymbol{x}_{\mathbb{K}}$ are column vectors of length $V-1, P-1, 2g$, respectively. it follows

$$\begin{pmatrix} \mathbb{L}^T\mathbb{L} & \mathbb{O} & \mathbb{O} \\ \mathbb{O} & \mathbb{S}^T\mathbb{S} & \mathbb{S}^T\mathbb{K} \\ \mathbb{O} & \mathbb{K}^T\mathbb{S} & \mathbb{K}^T\mathbb{K} \end{pmatrix} \boldsymbol{x} = \begin{pmatrix} \mathbf{0}_{\mathbb{L}} \\ \mathbf{0}_{\mathbb{S}} \\ \mathbf{e}_{\mathbb{K}} \end{pmatrix}. \tag{4.43}$$

In Eq. (4.43), the off-diagonal blocks in the first row and column are zero, and the first block in the RHS is also zero. As a result, $\boldsymbol{x}_{\mathbb{L}} = \mathbf{0}$. It can be removed from the equation to get Eq. (4.44), which also indicates that the GLBFs only depends on the SBFs and the non-contractible circles.

$$\begin{pmatrix} \mathbb{S}^T\mathbb{S} & \mathbb{S}^T\mathbb{K} \\ \mathbb{K}^T\mathbb{S} & \mathbb{K}^T\mathbb{K} \end{pmatrix} \begin{pmatrix} \boldsymbol{x}_{\mathbb{S}} \\ \boldsymbol{x}_{\mathbb{K}} \end{pmatrix} \begin{pmatrix} \mathbf{0}_{\mathbb{S}} \\ \mathbf{e}_{\mathbb{K}} \end{pmatrix}. \tag{4.44}$$

Let $\mathbb{G} = \mathbb{K}^T\mathbb{K} - \mathbb{K}^T\mathbb{S}\left(\mathbb{D}_{\mathbb{S}}\right)^{-1}\mathbb{S}^T\mathbb{K}$. Eq. (4.44) can be solved and the results are $\boldsymbol{x}_{\mathbb{K}} = \mathbb{G}^{-1}\mathbf{e}_{\mathbb{K}}$, $\boldsymbol{x}_{\mathbb{S}} = -\left(\mathbb{D}_{\mathbb{S}}\right)^{-1}\mathbb{S}^T\mathbb{K}\cdot\boldsymbol{x}_{\mathbb{K}}$. Finally, one has

$$\boldsymbol{g} = \mathbb{S}\cdot\boldsymbol{x}_{\mathbb{S}} + \mathbb{K}\cdot\boldsymbol{x}_{\mathbb{K}}. \tag{4.45}$$

The matrix $\mathbb{G}$ is a $2g \times 2g$ matrix. When the number of genera is small, this matrix can be directly computed by $2g$ times solving graph Laplacian equations. Since the cost of each Laplacian equation is on the order of $\mathcal{O}(N_E)$, as a result, the total complexity of the solution is $\mathcal{O}(g^2 N_E)$. Furthermore, this matrix can be stored in $\mathcal{O}(g^2)$ and inverted with an $\mathcal{O}(g^3)$ complexity. In the cases where $g \ll E$, the overall complexity is $\mathcal{O}(g^2 E)$.

4.8.4 Some examples of GLBFs on torus

Fig. 4.24 shows a square torus with a single genus. The torus is discretized by 32 vertices, 32 square quadrilaterals, and 64 quadrilateral BFs. In this case, there are two GLBFs present. The first GLBF models a current mode that flows perpendicularly to the axis of the torus. The second GLBF represents a current that is approximately parallel to the axis.

There are 6 independent GLBFs on the triple torus shown in Fig. 4.25. There are 64 vertices, 68 square quadrilaterals and 136 quadrilateral BFs. For convenience, only two of them are shown. It is clearly seen from Fig. 4.25 that the toroidal GLBF is related to one of the genera of the torus.

4.9 Conclusion

A framework for solving surface integral equation on quadrilateral, triangular, and mixed quadrilateral-triangular meshes was presented. The key presented

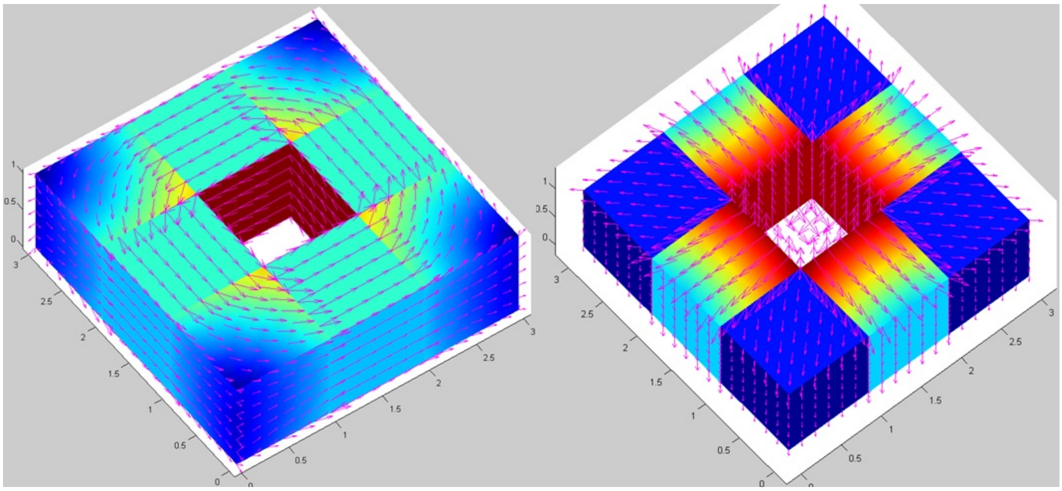

Figure 4.24: GLBFs on a square torus.

ideas are listed next: (i) The initial mesh was partitioned into a QBM, which was obtained from the initial triangles or quadrilaterals by partitioning a triangle into three quadrilaterals or a quadrilateral into four quadrilaterals, (ii) bQBFs residing on QBMs were defined and they served as a building block in constructing a set of PBF and DBFs, (iii) PBFs were constructed as a linear combination of bQBFs, which are well suited for representing surface currents on quadrilaterals, triangular, and mixed meshes as well as more generally-shaped polygons, (iv) DBFs were defined using bQBFs, which are suitable for CMPs on different mesh types, (v) based on the introduced PBFs and DBFs, CMPs were constructed, which allow eliminating the dense-mesh breakdown of EFIE for different mesh types.

The seamless handling of the mixed meshes was allowed by the construction of QBMs. bQBFs rendered a redefinition of divergence-conforming vector basis function on quadrilaterals as a linear combination of bQBFs. For triangular meshes, bQBFs led to PBFs similar to RWG-BFs. The QBMs and bQBFs allowed merging quadrilaterals and triangles in terms of PBF construction. Moreover, the quadrilateral-partitioning approach can be naturally extended to more general polygons, allowing for a seamless handling of arbitrary polygonal meshes.

Based on QBMs and bQBFs, a general definition of DBFs was given for quadrilateral meshes and the same approach was extended to triangular and mixed

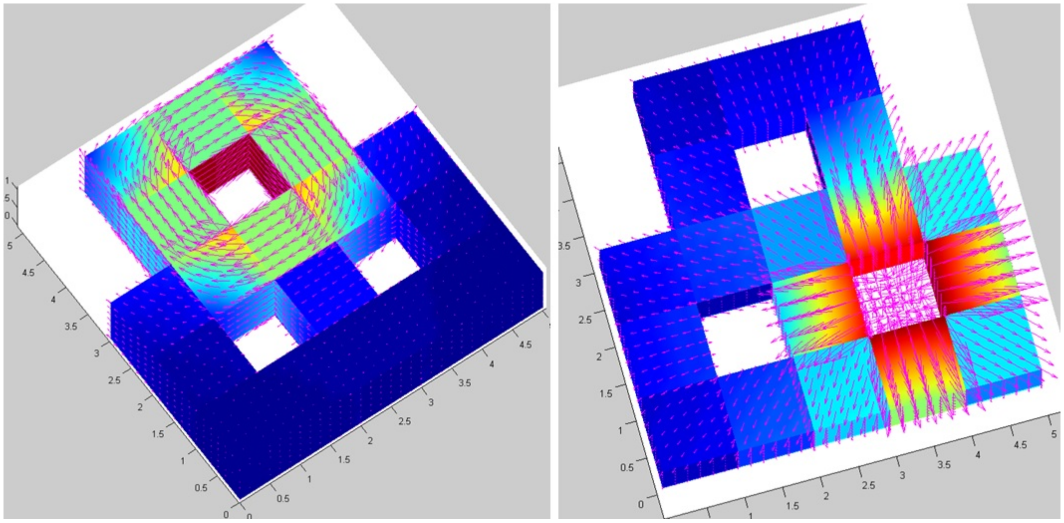

Figure 4.25: GLBFs on a square triple torus.

meshes, without any modification. The introduced DBFs have a number of important properties, which were used for constructing CMPs on various types of meshes. The DBFs are defined on the secondary mesh formed by polygons per each initial mesh node [119, 120]. In this view, the DBFs can be seen as ordinary BFs but defined on a dual mesh. Historically, the idea of using subdivided triangles to generate a dual mesh dates back to 1967 [119]. Moreover, barycentric triangles also pervade in computer visualization of vector fields or interpolation methods on surfaces.

Importantly, the presented PBFs, DBFs, and CMP resulted in a substantially reduced number of unknowns, memory storage for sparse matrices, and quadrature points, which can be translated into an increased speed and reduced memory requirements. Numerical examples were shown verifying the effectiveness of the proposed PBFs and DBFs. The presented framework can be used for solving EFIE and other types of surface integral equations on complex structures meshed into elements of different types.

Chapter 5

Applications of quadrilateral basis functions

This chapter is devoted the applications of the proposed v-BFs, which are important theoretically and practically.

5.1 Working mechanisms of the Calderón preconditioner

It has been pointed out that the crux of the Calderón preconditioner is to ensure the vanishing of $\mathcal{T}_h^2$ after discretization. According to the Helmholtz decomposition, the current has three components: $\boldsymbol{I} = [\boldsymbol{I}^{SBF}; \boldsymbol{I}^{LLBF}; \boldsymbol{I}^{GLBF}]$. Here $\boldsymbol{I}^{SBF}, \boldsymbol{I}^{LLBF}, \boldsymbol{I}^{GLBF}$ are column vectors of length $F-1, V-1$, and $2g$ respectively. The current $\mathbf{J}$ is written as:

$$\mathbf{J}(\mathbf{r}) \approx \sum_{n=1}^{n=F-1} I_n^{SBF} \mathbf{f}_n^{SBF}(\mathbf{r}) + \sum_{n=1}^{n=V-1} I_n^{LLBF} \mathbf{f}_n^{LLBF}(\mathbf{r}) + \sum_{n=1}^{n=2g} I_n^{GLBF} \mathbf{f}_n^{GLBF}(\mathbf{r}). \quad (5.1)$$

The range of the operator $\mathcal{T}_h$ is approximately orthogonal to its domain. The range is expressed in terms of the DBFs[1]. Let $\tilde{\boldsymbol{I}}^{LLBF} = [\tilde{I}_1^{LLBF}, \ldots, \tilde{I}_{F-1}^{LLBF}]^T$,

---

[1] Here we do not specify the kind of DBFs. The DBFs in this chapter are an excellent choice, but there can be other options

$\tilde{\boldsymbol{I}}^{SBF} = [\tilde{I}_1^{SBF}, \dots, \tilde{I}_{V-1}^{SBF}]^T$, $\tilde{\boldsymbol{I}}^{GLBF} = [\tilde{I}_1^{GLBF}, \dots, \tilde{I}_{2g}^{GLBF}]^T$.

$$[\mathcal{T}(\mathbf{J})](\mathbf{r}) \approx \sum_{n=1}^{n=F-1} \tilde{I}_n^{LLBF} \tilde{\mathbf{f}}_n^{LLBF}(\mathbf{r}) + \sum_{n=1}^{n=V-1} \tilde{I}_n^{SBF} \tilde{\mathbf{f}}_n^{SBF}(\mathbf{r}) + \sum_{n=1}^{n=2g} \tilde{I}_n^{GLBF} \tilde{\mathbf{f}}_n^{GLBF}(\mathbf{r}). \tag{5.2}$$

To ge the coefficients in Eq. (5.2), the test functions are used:

$$\begin{pmatrix} \mathbb{Z}^{SS} & \mathbb{Z}^{SL} & \mathbb{Z}^{SG} \\ \mathbb{Z}^{LS} & \mathbb{Z}^{LL} & \mathbb{Z}^{LG} \\ \mathbb{Z}^{GS} & \mathbb{Z}^{GL} & \mathbb{Z}^{GG} \end{pmatrix} \begin{pmatrix} \boldsymbol{I}^{SBF} \\ \boldsymbol{I}^{LLBF} \\ \boldsymbol{I}^{GLBF} \end{pmatrix} = \begin{pmatrix} \mathbb{G}^{nSL} & \mathbb{G}^{nSS} & \mathbb{G}^{nSG} \\ \mathbb{G}^{nLL} & \mathbb{G}^{nLS} & \mathbb{G}^{nLG} \\ \mathbb{G}^{nGL} & \mathbb{G}^{nGS} & \mathbb{G}^{nGG} \end{pmatrix} \begin{pmatrix} \tilde{\boldsymbol{I}}^{LLBF} \\ \tilde{\boldsymbol{I}}^{SBF} \\ \tilde{\boldsymbol{I}}^{GLBF} \end{pmatrix}. \tag{5.3}$$

The superscripts “S”, “L”, “G” are shorted for SBF, LLBF and GLBF respectively. An element in the hypersingular part of the impedance $\mathbb{Z}_h$ is

$$(\mathbb{Z}_h^{xy})_{mn} = \oiint_\Gamma d\mathbf{r} \nabla_S \cdot \mathbf{f}_m^x(\mathbf{r}) \oiint_\Gamma d\mathbf{r}' \nabla_S' \cdot \mathbf{f}_n^y(\mathbf{r}') \frac{e^{-ik|\mathbf{r}-\mathbf{r}'|}}{4\pi|\mathbf{r}-\mathbf{r}'|}. \tag{5.4}$$

where x, y can be any of “S”, “L” or “G”. Since $\nabla_S \cdot \mathbf{f}_n^{LLBF}(\mathbf{r}) = 0$, $\nabla_S \cdot \mathbf{f}_n^{GLBF}(\mathbf{r}) = 0$, only when both x, y are the SBFs, $(\mathbb{Z}_h^{xy})_{mn} \neq 0$. The hypersingular part of the impedance matrix is:

$$\mathbb{Z}_h = \begin{pmatrix} \mathbb{Z}_h^{SS} & \mathbb{Z}_h^{SL} & \mathbb{Z}_h^{SG} \\ \mathbb{Z}_h^{LS} & \mathbb{Z}_h^{LL} & \mathbb{Z}_h^{LG} \\ \mathbb{Z}_h^{GS} & \mathbb{Z}_h^{GL} & \mathbb{Z}_h^{GG} \end{pmatrix} = \begin{pmatrix} \mathbb{Z}_h^{SS} & \mathbb{O} & \mathbb{O} \\ \mathbb{O} & \mathbb{O} & \mathbb{O} \\ \mathbb{O} & \mathbb{O} & \mathbb{O} \end{pmatrix}. \tag{5.5}$$

It can be seen that only the first block in the matrix $\mathbb{Z}_h$ is nonzero, all other parts vanish. The second matrix in Eq. (5.3) is termed Gram matirx, which is sparse and has some interesting properties, which are listed here:

- The first diagonal term $\mathbb{G}^{nSL}$ is a $(F-1) \times (F-1)$ matrix. $(\mathbb{G}^{nSL})_{mn} = \iint_\Gamma \hat{\mathbf{n}} \times \mathbf{f}_m^{SBF}(\mathbf{r}) \cdot \tilde{\mathbf{f}}_n^{LLBF}(\mathbf{r}) dS$. It is similar to a Graph Laplacian. It is invertible but ill-conditioned.The second diagonal term $\mathbb{G}^{nLS}$ is a $(V-1) \times (V-1)$ matrix. $(\mathbb{G}^{nLS})_{mn} = \iint_\Gamma \hat{\mathbf{n}} \times \mathbf{f}_m^{LLBF}(\mathbf{r}) \cdot \tilde{\mathbf{f}}_n^{SBF}(\mathbf{r}) dS$. Its properties are close to $\mathbb{G}^{nSL}$. The third diagonal term is $\mathbb{G}^{nGG}$. It is a square matrix. Since the GLBFs have many equivalent forms, the conditioning of $\mathbb{G}^{nGG}$ is indefinite.

- $\mathbb{G}_{nSL}$ is a $(F-1) \times (V-1)$ non-square matrix. $(\mathbb{G}^{nSS})_{mn} = \iint_\Gamma \hat{\mathbf{n}} \times \mathbf{f}_m^{SBF}(\mathbf{r}) \cdot \tilde{\mathbf{f}}_n^{SBF}(\mathbf{r}) dS$. Similarly, $\mathbb{G}_{nSG}$ is a $(F-1) \times 2g$ non-square matrix. $(\mathbb{G}^{nSG})_{mn} = \iint_\Gamma \hat{\mathbf{n}} \times \mathbf{f}_m^{SBF}(\mathbf{r}) \cdot \tilde{\mathbf{f}}_n^{GLBF}(\mathbf{r}) dS$.

- $\mathbb{G}_{nLL}$ is a $(V-1)\times(F-1)$ non-square matrix. Surprisingly, it is zero. $(\mathbb{G}^{nLL})_{mn} = \iint_\Gamma \hat{\mathbf{n}}\times\mathbf{f}_m^{LLBF}(\mathbf{r})\cdot\tilde{\mathbf{f}}_n^{LLBF}(\mathbf{r})dS$. This is because any LLBF can be written as $\mathbf{f}_m^{LLBF}(\mathbf{r}) = \hat{\mathbf{n}}\times\nabla\phi$, here ϕ is a continuous scalar function. So the above integral becomes $-\iint_\Gamma \nabla\phi\cdot\tilde{\mathbf{f}}_n^{LLBF}(\mathbf{r})dS = \iint_\Gamma \phi\nabla\cdot\tilde{\mathbf{f}}_n^{LLBF}(\mathbf{r})dS - \iint_\Gamma \nabla\cdot\left[\phi\tilde{\mathbf{f}}_n^{LLBF}(\mathbf{r})\right]dS$. The first term in the right side is zero, since $\nabla\cdot\tilde{\mathbf{f}}_n^{LLBF}(\mathbf{r}) = 0$; the second term is also zero since the function $\tilde{\mathbf{f}}_m^{LLBF}(\mathbf{r})$ has zero normal component along its support.

- The terms $\mathbb{G}^{nLG}, \mathbb{G}^{nGL}$ are zero matrices. The reason is similar to that for $\mathbb{G}^{nLL}$.

To use $\mathcal{T}$ as a preconditioner, its range is tested again, but with the DBFs $\tilde{\mathbf{f}}_m^{SBF}, \tilde{\mathbf{f}}_m^{LLBF}, \tilde{\mathbf{f}}_m^{GLBF}$. Then the discretized form of $\mathcal{T}_h$ becomes:

$$\tilde{\mathbb{Z}}_h = \begin{pmatrix} \tilde{\mathbb{Z}}_h^{LL} & \tilde{\mathbb{Z}}_h^{LS} & \tilde{\mathbb{Z}}_h^{LG} \\ \tilde{\mathbb{Z}}_h^{SL} & \tilde{\mathbb{Z}}_h^{SS} & \tilde{\mathbb{Z}}_h^{SG} \\ \tilde{\mathbb{Z}}_h^{GL} & \tilde{\mathbb{Z}}_h^{GS} & \tilde{\mathbb{Z}}_h^{GG} \end{pmatrix} \tag{5.6}$$

Again, because $\nabla\cdot\tilde{f}_m^{LLBF} = 0, \nabla\cdot\tilde{f}_m^{GLBF} = 0$, only $\tilde{\mathbb{Z}}_h^{SS}$ is nonzero in Eq. (5.6). The discretization of $\mathcal{T}_h^2$ is:

$$(\mathbb{Z}_h^2)_{dis} = \begin{pmatrix} \mathbb{O} & \mathbb{O} & \mathbb{O} \\ \mathbb{O} & \tilde{\mathbb{Z}}_h^{SS} & \mathbb{O} \\ \mathbb{O} & \mathbb{O} & \mathbb{O} \end{pmatrix} \begin{pmatrix} \mathbb{G}^{nSL} & \mathbb{G}^{nSS} & \mathbb{G}^{nSG} \\ \mathbb{O} & \mathbb{G}^{nLS} & \mathbb{O} \\ \mathbb{O} & \mathbb{G}^{nGS} & \mathbb{G}^{nGG} \end{pmatrix}^{-1} \begin{pmatrix} \mathbb{Z}_h^{SS} & \mathbb{O} & \mathbb{O} \\ \mathbb{O} & \mathbb{O} & \mathbb{O} \\ \mathbb{O} & \mathbb{O} & \mathbb{O} \end{pmatrix}. \tag{5.7}$$

It can be verified that the inverse of the Gram matrix is:

$$\begin{pmatrix} (\mathbb{G}^{nSL})^{-1} & \mathbb{G}_{12} & -(\mathbb{G}^{nSL})^{-1}\mathbb{G}^{nSG}(\mathbb{G}^{nGG})^{-1} \\ \mathbb{O} & (\mathbb{G}^{nLS})^{-1} & \mathbb{O} \\ \mathbb{O} & -(\mathbb{G}^{nGG})^{-1}\mathbb{G}^{nGS}(\mathbb{G}^{nLS})^{-1} & (\mathbb{G}^{nGG})^{-1} \end{pmatrix} \tag{5.8}$$

where $\mathbb{G}_{12} = -(\mathbb{G}^{nSL})^{-1}\mathbb{G}^{nSS}(\mathbb{G}^{nLS})^{-1} + (\mathbb{G}^{nSL})^{-1}(\mathbb{G}^{nSG})(\mathbb{G}^{nGG})^{-1}\mathbb{G}^{nGS}(\mathbb{G}^{nLS})^{-1}$. The inverse of the Gram matrix has the same structure as itself. Inserting Eq. (5.8) into Eq. (5.7), one can verify that $(\mathcal{T}_h^2)_{dis} = \mathbb{O}$. All these inversions are used only for theoretical analysis, they are not intended for practical implementation. As was pointed out in [95], for a simply connected and closed mesh, the vanishing requirement translates into:

$$dim\text{PBF}^{sol} + dim\text{DBF}^{sol} = E - 2g. \tag{5.9}$$

where $dim\text{PBF}^{sol}$ and $dim\text{DBF}^{sol}$ are the dimension of the solenoidal subspace of PBF and DBF, respectively. RWG-like BFs cannot be used here for two reasons. First, the resulting Gram matrix is singular. Second, if RWG-BFs are used for both PBF and DBF sets, then $dim\text{PBF}^{sol} = dim\text{DBF}^{sol} = V - 1$, where V is the number of vertices. However, in general $2(V-1) \neq E - 2g$, violating the condition (5.9). Some would suggest $\hat{\mathbf{n}} \times$ RWG be used as a DBF, however, it results in a fictitious line charge and it cannot ensure cancellation condition either.

5.2 Calderón multiplicative preconditioner

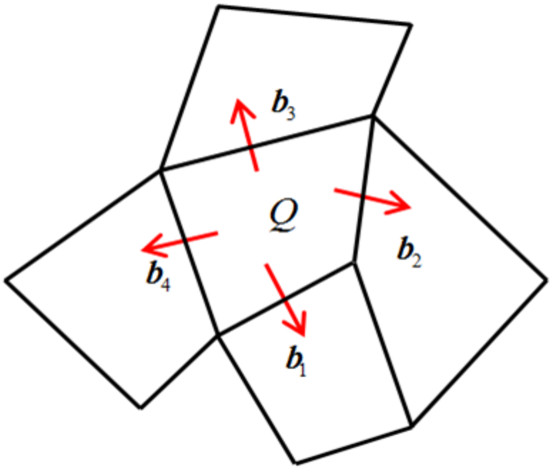

Figure 5.1: Four bQBFs that share a common quadrilateral. Since $\mathbf{b}_1 \parallel \mathbf{b}_3$, $\iint_\Gamma \hat{\mathbf{n}} \times \mathbf{b}_1 \cdot \mathbf{b}_3 dS = 0$. On the other hand, $\iint_\Gamma \hat{\mathbf{n}} \times \mathbf{b}_1 \cdot \mathbf{b}_2 dS = -4$. These results are independent of the size or shape of the mesh, so they are topologically invariant.

The development of PBFs and DBFs in the preceding sections allows developing a CMP for quadrilateral, triangular, and mixed meshes. For a CMP one needs to create the Gram matrix linking the PBFs and DBFs on triangular, quadrilateral or mixed meshes. This matrix is $\mathbb{G}_m^{PD} \in \mathbb{R}^{N_E \times N_E}$, $\left(\mathbb{G}_m^{PD}\right)_{mn} =$

$\left\langle \hat{\mathbf{n}} \times \mathbf{f}_m^{PBF}, \mathbf{f}_n^{DBF} \right\rangle$. $\mathbb{G}_m^{PD}$ is sparse and its entries are, where $\mathbf{f}_m^{PBF}$ is the m-th PBF and $\mathbf{f}_n^{DBF}$ is the n-th DBF. Employing the projection matrices, one has $\mathbb{G}_m^{PD} = {\mathbb{P}_1}^T \mathbb{G}_m^{bQBF} \mathbb{P}_2$, where $\mathbb{G}_m^{bQBF}$ is a real-valued $N_b \times N_b$ matrix, $(\mathbb{G}_m^{bQBF})_{mn} = \langle \hat{\mathbf{n}} \times \mathbf{b}_m, \mathbf{b}_n \rangle$, with $\mathbf{b}_m$ and $\mathbf{b}_n$ being the QBFs. The four bQBFs sharing a quadrilateral Q are displayed in Fig. 5.2. They can be expressed as $\left(\mathbb{G}_m^{PD}\right)_{mn}$.

Since $(\mathbb{G}_m^{bQBF})_{nm} = \langle \hat{\mathbf{n}} \times \mathbf{b}_n, \mathbf{b}_m \rangle = -\langle \hat{\mathbf{n}} \times \mathbf{b}_m, \mathbf{b}_n \rangle$, $\mathbb{G}_m^{bQBF}$ is an anti-symmetric matrix. On the quadrilateral, the expressions for the four v-BFs are:

$$\mathbf{b}_1 = \frac{(u+1)\mathbf{r}_u}{\det \mathbf{J}}, \mathbf{b}_2 = \frac{(v+1)\mathbf{r}_v}{\det(\mathbf{J})}, \mathbf{b}_3 = \frac{(u-1)\mathbf{r}_u}{\det \mathbf{J}}, \mathbf{b}_4 = \frac{(v-1)\mathbf{r}_v}{\det(\mathbf{J})}. \tag{5.10}$$

It follows that $\mathbf{b}_1$ and $\mathbf{b}_3$ are parallel to each other, so are the pair $\mathbf{b}_2$ and $\mathbf{b}_4$. As a result, $\langle \hat{\mathbf{n}} \times \mathbf{b}_1, \mathbf{b}_3 \rangle = \langle \hat{\mathbf{n}} \times \mathbf{b}_2, \mathbf{b}_4 \rangle = 0$. The result of $\langle \hat{\mathbf{n}} \times \mathbf{b}_1, \mathbf{b}_2 \rangle$ is not obvious. We substitute the formulas in Eq. (5.10) into it. It follows:

$$\begin{aligned} \langle \hat{\mathbf{n}} \times \mathbf{b}_1, \mathbf{b}_2 \rangle &= \left\langle \hat{\mathbf{n}} \times \frac{(u+1)\mathbf{r}_u}{\det \mathbf{J}}, \frac{(v+1)\mathbf{r}_v}{\det \mathbf{J}} \right\rangle \\ = \iint_Q \hat{\mathbf{n}} \times \frac{(u+1)\mathbf{r}_u}{\det(\mathbf{J})} \cdot \frac{(v+1)\mathbf{r}_v}{\det(\mathbf{J})} dS &= \iint_Q (u+1)(v+1) \frac{\hat{\mathbf{n}} \times \mathbf{r}_u \cdot \mathbf{r}_v}{[\det(\mathbf{J})]^2} dS. \end{aligned} \tag{5.11}$$

Since $dS = \det(\mathbf{J}) du dv$, $\hat{\mathbf{n}} \times \mathbf{r}_u \cdot \mathbf{r}_v = \det(\mathbf{J})$, the above integral becomes $\langle \hat{\mathbf{n}} \times \mathbf{b}_1, \mathbf{b}_2 \rangle = \int_{-1}^{1} (1+u) du \int_{-1}^{1} (1+v) dv = 4$. This result demonstrates that the Gram matrix is an intrinsic property of the connectivity of the mesh elements, it does not depend on the positions of the vertices. Therefore, it is topologically invariant. The matrix $\mathbb{G}_m^{bQBF}$ is highly sparse, each row or column has only two non-zero entries, whose values are ±4.

5.3 Numeric results

This section presents a set of numerical examples demonstrating the performance of the introduced framework of PBFs, DBFs, and associated CMP. The results are given for a problem of the electromagnetic field scattering from structures excited by an incident plane wave $\mathbf{E}^{\text{inc}} = \hat{\mathbf{x}} e^{-\frac{i2\pi z}{\lambda}}$, where λ is the wavelength. A GMRES [46] solver with a restart of 80 was used. The solver was implemented on graphics processing units (GPUs) to lead to a fast performance [50, 121]. In all the results, denoted by delta and epsilon are the discretized mesh element size and residual error, respectively.

5.3.1 Sphere

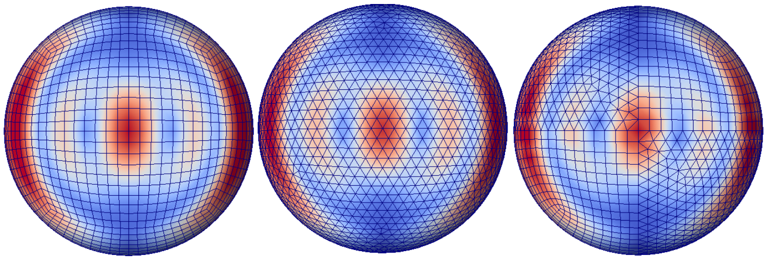

Figure 5.2: A sphere meshed into quadrilateral, triangular, and mixed elements. The color represents the the magnitude of the surface current distribution.

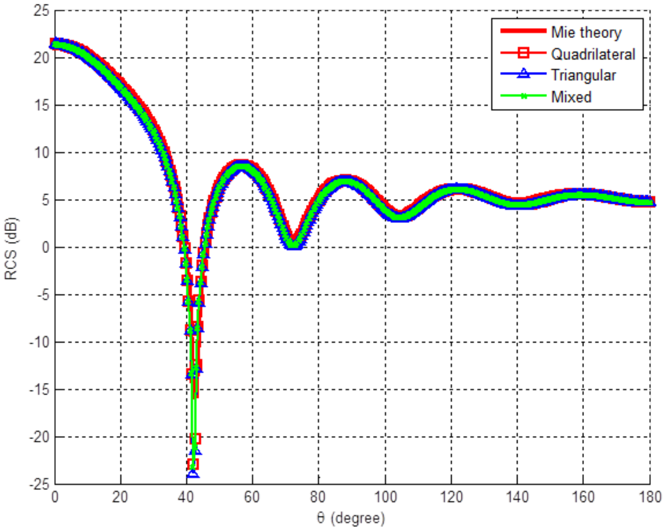

Figure 5.3: Analysis of scattering from PEC spheres ($\delta = 0.08\lambda$) discretized into quadrilateral, triangular or mixed elements. Comparisons in RCS verify the effectiveness of the proposed PBFs and DBFs.

Next we show scattering from a larger sphere, whose radius is four wavelengths. In this example, the CMP solver reduced the error to $\epsilon = 10^{-4}$ in 20

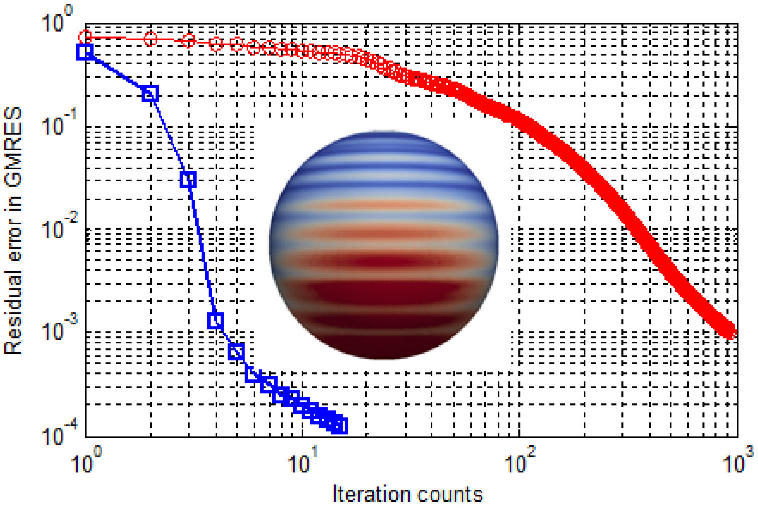

Figure 5.4: Iteration counts vs. residual errors for a sphere with a radius of 4λ.

Table 5.1: Number of edges in different meshes

Mesh Types	0.08	0.06	0.04	0.02
Quadrilateral	4800	8122	17022	65998
Triangular	6957	12633	28779	116085
Mixed	5880	10056	22756	92264

iterations, whereas the unpreconditioned system can only reach 10^{-3} in 1000 iterations.

In this example, a PEC sphere with a radius of 1λ is considered. The sphere is meshed with three mesh types: quadrilateral, triangular, and mixed, as shown in Fig. 5.2. The number of edges for different δ for quadrilateral, triangular, and mixed meshes is given in Table 5.1. Fig. 5.4 verifies the accuracy of the solvers for the three meshes by comparing the radar cross section (RCS) versus angle with the Mie series solution. The same-accuracy result was obtained for the cases with and without CMP. This example demonstrates that the introduced PBFs lead to a proper representation of the surface currents and that the new DBFs are applicable to CMPs. Fig. 5.2 shows the iteration counts versus residual errors for the solver with and without the CMP. It is found that without CMP, the convergence becomes very slow as the mesh density increases. With CMP, the convergence is much faster and the number of iterations is nearly independent of the number of edges for all mesh types, which confirms the effectiveness of the introduced DBFs and resulting CMP.

5.3.2 Plate

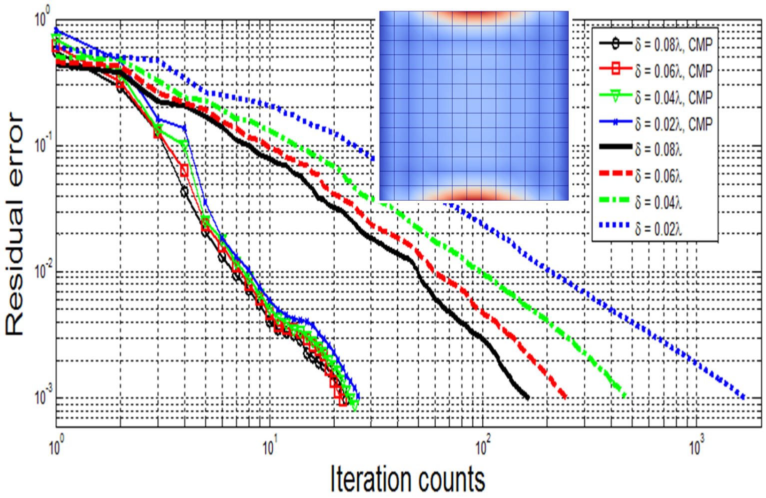

Figure 5.5: Iteration counts vs. residual errors for a $1\lambda 1\lambda$ square plate.

The next example considers a $1\lambda \times 1\lambda$ square plate placed at $z = 0$, discretized into quadrilaterals (Fig. 5.5). The numbers of edges for meshes with $\delta = 0.08\lambda, 0.06\lambda, 0.04\lambda$ and 0.02λ were $312, 544, 1200$ and 4900, respectively. The number of iterations was around 25 for all CMP solvers. On the other hand, for the unpreconditioned EFIE solvers, the iteration number grew dramatically with increased mesh density.

Again we can see that the CMP solver is much faster. This example also shows that the DBFs can solve the open structures with minor modifications.

5.3.3 Magnetic recording head

This example presents a complex magnetic recording head with large aspect ratios (Fig. 5.6). This problem is related to the emerging heat assisted magnetic

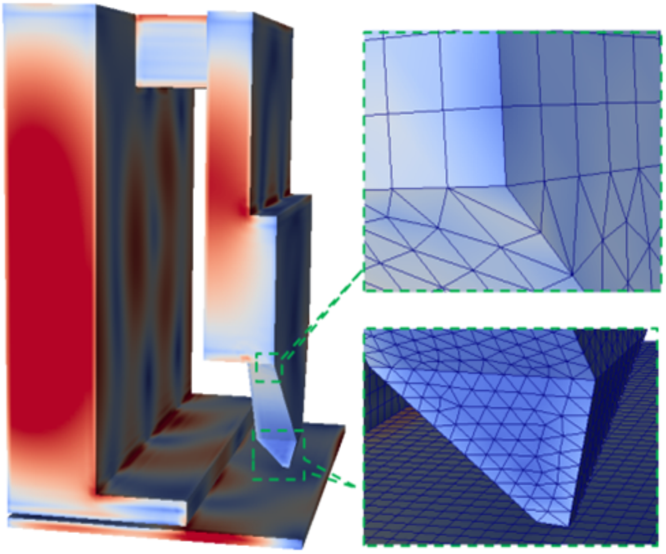

Figure 5.6: Current distribution on a magnetic recording head.

recording technology as well as the operation of hard drives in certain integrated systems. The head was illuminated by a plane wave. Its height and width were 1.7λ and 1.1λ, respectively. The bulk of the head and its underlayer were flat, meshed into (54341, mostly rectangular) quadrilaterals, while the more complex area around the sharp tapered tip was meshed into 5218 triangles. The total number of edges was $N_E = 116509$. With CMP, the iteration count was 170 for $\epsilon = 3 \times 10^{-3}$. The solver could not converge in a reasonable time without CMP.

5.4 Conclusion

This chapter shows the applications of the proposed PBF and DBF. Especially, they are used into the scattering problems that is modeled by the EFIE. The PBF is used to expand the unknown current, whereas the DBF is used the preconditioner. The numerical result has shown that the speed of the preconditioned EFIE system achieved a much faster speed since the impedance matrix is well-conditioned.

The DBFs can also be used to improve the accuracy of the MFIE. The

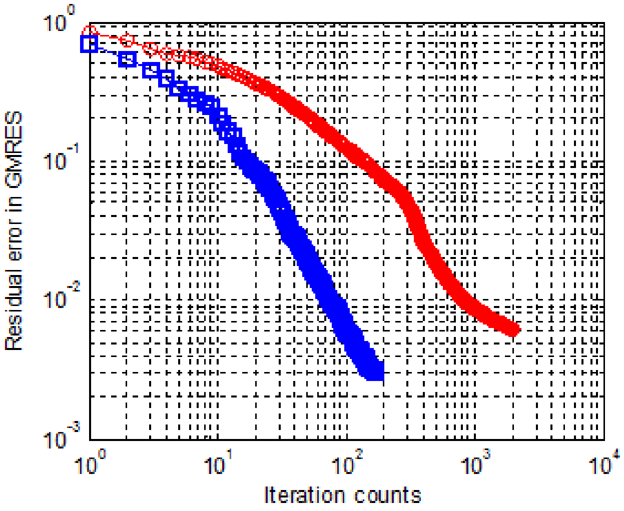

Figure 5.7: Iteration counts for a magnetic recording head.

traditional method tested the MFIE using Galerkin methods, where the testing functions and the expansion functions are in the same set. This method suffers from poor accuracy. On the other hand, when the current is expanded by the PBFs and the testing functions are the DBFs, the accuracy could be improved by a magnitude.

Acknowledgements: Chapter 5, in part, is based on the journal article: R. Chang, V. Lomakin, "Quadrilateral Barycentric Basis Functions for Surface Integral Equations," IEEE Trans. Antennas Propag., vol. 61, no. 12, Dec. 2013. The dissertation author was the contributing author to this article.

Chapter 6

Implementation of volume integral equations

The surface integral equations (SIEs) are well-suited for homogeneous structures. However, it is quite difficult to solve very complex structures. A general solution is to use volume integral equation (VIE), which is based on volume equivalence principles. The VIEs employ some fictitious currents as the unknown sources, which are obtained by solving a linear equation. Compared to FEM, the VIEs yield better-conditioned matrices, leading to a smaller number of iterations [122, 123].

In this chapter, we further explore the potential-based volume integral equation (PVIE). While the field quantities have discontinuities along the boundaries, the potentials are continuous throughout the whole space.

6.1 Volume equivalence principle

The Maxwell equation in the frequency domain reads:

$$\begin{aligned} \nabla \times \mathbf{E} &= -i\omega\mu_0\mu_r\mathbf{H}, \\ \nabla \times \mathbf{H} &= i\omega\epsilon_0\epsilon_r\mathbf{E}. \end{aligned} \tag{6.1}$$

In a scattering problem, the material properties μ_r and ϵ_r are not a constant, but can be a function of $\mathbf{r}$. There is no impressed current in the volume Ω. To make the problem Eq. (6.1) look like a free space problem, we define equivalent electric and magnetic currents [87, 89]:

$$\mathbf{J}_{\text{eq}} = i\omega\mu_0(\mu_r - 1)\mathbf{E}, \mathbf{M}_{\text{eq}} = i\omega\epsilon_0(\epsilon_r - 1)\mathbf{H}. \tag{6.2}$$

The equivalent currents $\mathbf{J}_{\text{eq}}$ and $\mathbf{M}_{\text{eq}}$ exist only inside the material region Ω. The Maxwell equations are reformulated as

$$\begin{aligned} \nabla \times \mathbf{E} &= -i\omega\mu_0\mathbf{H} - \mathbf{M}_{\text{eq}}, \\ \nabla \times \mathbf{H} &= i\omega\epsilon_0\mathbf{E} + \mathbf{J}_{\text{eq}}. \end{aligned} \tag{6.3}$$

The electric and magnetic fields, scattered from an obstacle, have vector potentials [49]:

$$\begin{aligned} \mathbf{A}^{\text{sc}}(\mathbf{r}) &= \iiint_{\Omega} \frac{\exp(-ik|\mathbf{r}-\mathbf{r}'|)}{4\pi|\mathbf{r}-\mathbf{r}'|}\mathbf{M}_{\text{eq}}(\mathbf{r}')d\mathbf{r}', \\ \mathbf{F}^{\text{sc}}(\mathbf{r}) &= \iiint_{\Omega} \frac{\exp(-ik|\mathbf{r}-\mathbf{r}'|)}{4\pi|\mathbf{r}-\mathbf{r}'|}\mathbf{J}_{\text{eq}}(\mathbf{r}')d\mathbf{r}'. \end{aligned} \tag{6.4}$$

The scattered electric and magnetic fields are due to the vector potentials. The summation of the scattered and the incident field is the total field.

6.2 Field based volume integral equations

The scattered fields are related to the potentials:

$$\begin{aligned} \mathbf{E}^{\text{sca}} &= i\eta_0\frac{\nabla\nabla\cdot+k^2}{k}\mathbf{A} - \nabla\times\mathbf{F}, \\ \mathbf{H}^{\text{sca}} &= i\frac{\nabla\nabla\cdot+k^2}{\eta_0 k}\mathbf{F} + \nabla\times\mathbf{A}. \end{aligned} \tag{6.5}$$

The total fields are the summation of incident and scattered fields:

$$\begin{aligned} \mathbf{E}^{\text{inc}} + i\eta_0\frac{\nabla\nabla\cdot+k^2}{k}\mathbf{A} - \nabla\times\mathbf{F} &= \mathbf{E}, \\ \mathbf{H}^{\text{inc}} + i\frac{\nabla\nabla\cdot+k^2}{\eta_0 k}\mathbf{F} + \nabla\times\mathbf{A} &= \mathbf{H}. \end{aligned} \tag{6.6}$$

The EFIE and MFIE for volume problems are:

$$\begin{aligned}
&\frac{\mathbf{D}}{\epsilon_r} - (\nabla\nabla\cdot + k^2) \iiint_\Omega k_e \mathbf{D}(\mathbf{r}') \frac{\exp(-ik|\mathbf{r}-\mathbf{r}'|)}{4\pi|\mathbf{r}-\mathbf{r}'|} d\mathbf{r}' \\
&+\frac{ik}{\eta_0}\nabla\times \iiint_\Omega k_e \mathbf{B}(\mathbf{r}') \frac{\exp(-ik|\mathbf{r}-\mathbf{r}'|)}{4\pi|\mathbf{r}-\mathbf{r}'|} d\mathbf{r}' = \epsilon_0 \mathbf{E}^{\text{inc}}, \\
&\frac{\mathbf{B}}{\mu_r} - (\nabla\nabla\cdot + k^2) \iiint_\Omega k_m \mathbf{B}(\mathbf{r}') \frac{\exp(-ik|\mathbf{r}-\mathbf{r}'|)}{4\pi|\mathbf{r}-\mathbf{r}'|} d\mathbf{r}' \\
&-ik\eta_0\nabla\times \iiint_\Omega k_e \mathbf{D}(\mathbf{r}') \frac{\exp(-ik|\mathbf{r}-\mathbf{r}'|)}{4\pi|\mathbf{r}-\mathbf{r}'|} d\mathbf{r}' = \mu_0 \mathbf{H}^{\text{inc}}.
\end{aligned} \tag{6.7}$$

where $k_e = 1 - \frac{1}{\epsilon_r}, k_m = 1 - \frac{1}{\mu_r}$. k_e and k_m are also called contrast ratios. In these two equations, the unknown quantities are the flux densities $\mathbf{D}$ and $\mathbf{B}$. These two are preferred because the normal components are continuous across different media. Since most materials react weakly to the external magnetic field, i.e. $\mu_r \approx 1$. The above equation becomes:

$$\frac{\mathbf{D}}{\epsilon_r} - (\nabla\nabla\cdot + k^2) \iiint_\Omega \frac{\exp(-ik|\mathbf{r}-\mathbf{r}'|)}{4\pi|\mathbf{r}-\mathbf{r}'|} k_e \mathbf{D}(\mathbf{r}') d\mathbf{r}' = \epsilon_0 \mathbf{E}^{\text{inc}}. \tag{6.8}$$

6.2.1 Basis functions for the volume integral equations

Since the field quantities are vectors, the v-BFs should be used. The most widely used v-BFs are the so called Schaubert-Wilton-Glisson (SWG) BFs [124, 125, 32, 126]. The SWG is very similar to RWG [127]. It ensures the normal continuity across different media. An SWG is show in Fig. 6.1, its definition is:

$$\mathbf{f}_m(\mathbf{r}) = \begin{cases} \frac{\mathbf{r}_m^+}{3V_m^+}, & \mathbf{r} \in T_m^+, \\ \frac{\mathbf{r}_m^-}{3V_m^-}, & \mathbf{r} \in T_m^-. \end{cases} \tag{6.9}$$

The divergence of the SWG-BF is:

$$\nabla\cdot\mathbf{f}_m(\mathbf{r}) = \begin{cases} \frac{1}{V_m^+}, & \mathbf{r} \in T_m^+, \\ -\frac{1}{V_m^-}, & \mathbf{r} \in T_m^-. \end{cases} \tag{6.10}$$

Hexahedrons can also be used in VIEs [128]. They result in a smaller number of elements and unknowns. The v-BFs on hexahedrons are a generalization of the QBFs on quadrilaterals. The number of SWG-BFs, denoted by N_{SWG} is the number of triangles in the mesh. Let $\boldsymbol{I}^{SWG} = [I_1^{SWG}, I_2^{SWG}, \ldots, I_{N_{SWG}}^{SWG}]^T$ be

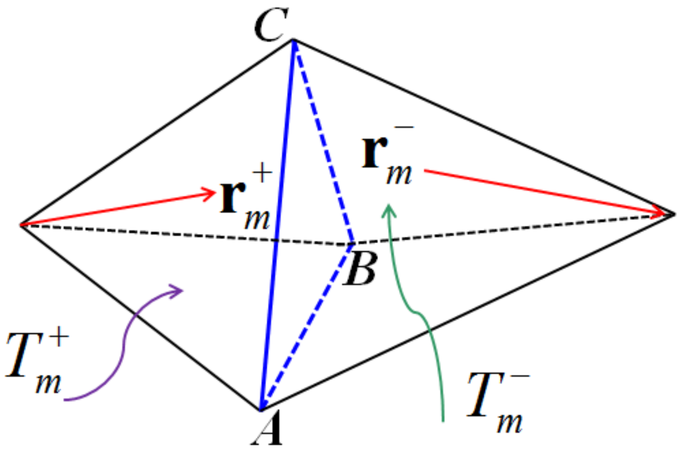

Figure 6.1: Defintion of an SWG basis. The SWG is associated with the triangle formed by the blue lines. T_m^+ is the tetrahedrons with positive charge, T_m^- is the tetrahedron with negative charge.

a column vector. When the divergence-conforming v-BFs are used, the electric current is expanded as:

$$\mathbf{D}(\mathbf{r}) \approx \sum_{n=1}^{n=N_{SWG}} I_n^{SWG} \mathbf{f}_n^{SWG}(\mathbf{r}). \tag{6.11}$$

The impedance matrix is written as:

$$\begin{aligned}\mathbb{Z}_{mn} = &\iiint_{\Omega_m \cup \Omega_n} \frac{\mathbf{f}_m(\mathbf{r}) \cdot \mathbf{f}_n(\mathbf{r})}{\epsilon_r} d\mathbf{r} - k^2 \iiint_{\Omega_m} d\mathbf{r} \mathbf{f}_m(\mathbf{r}) \cdot \iiint_{\Omega_n} d\mathbf{r}' \frac{e^{-ik|\mathbf{r}-\mathbf{r}'|}}{4\pi|\mathbf{r}-\mathbf{r}'|} k_e \mathbf{f}_n(\mathbf{r}') \\ &+ \iiint_{\Omega_m} d\mathbf{r} \nabla \cdot \mathbf{f}_m(\mathbf{r}) \iiint_{\Omega_n} d\mathbf{r}' \frac{e^{-ik|\mathbf{r}-\mathbf{r}'|}}{4\pi|\mathbf{r}-\mathbf{r}'|} \nabla' \cdot k_e \mathbf{f}_n(\mathbf{r}'). \end{aligned} \tag{6.12}$$

In Eq. (6.12), ∇ appears twice. To reduce the singularity of the Green function, one of the gradient operators is moved to $\mathbf{f}_m(\mathbf{r})$, the other is transferred to $\mathbf{f}_n(\mathbf{r})$. If ϵ_r is a constant, the matrix $\mathbb{Z}$ is symmetric.

6.2.2 Near field corrections for the potentials

There are two kinds of integrals.

$$\phi(\mathbf{r}) = \iiint_T \frac{\exp(-ik|\mathbf{r}-\mathbf{r}'|)}{|\mathbf{r}-\mathbf{r}'|} d\mathbf{r}' \tag{6.13}$$

To solve Eq. (6.13), we want to find a function $f(R)$ such that:

$$\nabla \cdot [f(R)(\mathbf{r}-\mathbf{r}')] = \frac{\exp(-ik|\mathbf{r}-\mathbf{r}'|)}{|\mathbf{r}-\mathbf{r}'|}. \tag{6.14}$$

Eq. (6.14) is equivalent to an ODE:

$$\frac{df}{dR} + \frac{3f(R)}{R} = \frac{\exp(-ikR)}{R^2}. \tag{6.15}$$

The solution is $q(R) = \frac{(1+ikR)e^{-ikR}-1}{k^2R^3}$. So, we have reduced the three dimensional volume integral into a two dimensional surface integral, which is much easier. Furthermore, we can transform the surface integral into line integrals [129]. Define a vector function $\mathbf{f} = (\boldsymbol{\rho}-\boldsymbol{\rho}')g(R)$. Its divergence is $\nabla_S \cdot \mathbf{f} = 2g(R) + \frac{dg}{dR}\frac{R^2-h^2}{R} = q(R)$.

$$2g(R) + \frac{dg}{dR}\frac{R^2-h^2}{R} = \frac{(1+ikR)e^{-ikR}-1}{k^2R^3}. \tag{6.16}$$

Solution to Eq. (6.16) is very simple: $g(R) = \frac{1-e^{-ikR}}{(R^2-h^2)Rk^2}$, therefore, the only integral we need to do is $\int_{x_1}^{x_2} \frac{e^{-ik\sqrt{x^2+a^2}}}{\sqrt{x^2+a^2}}dx$

$$\mathbf{A}(\mathbf{r}) = \iiint_T \frac{\exp(-ik|\mathbf{r}-\mathbf{r}'|)}{|\mathbf{r}-\mathbf{r}'|}(\mathbf{r}'-\mathbf{r})d\mathbf{r}' \tag{6.17}$$

The vector potential can be rewritten as:

$$\mathbf{A}(\mathbf{r}) = \frac{i}{k}\iiint_T \nabla' \exp(-ik|\mathbf{r}-\mathbf{r}'|)d\mathbf{r}' = \frac{i}{k}\oint\!\!\oint_{\partial T} \hat{\mathbf{n}}' \exp(-ik|\mathbf{r}-\mathbf{r}'|)d\mathbf{r}' \tag{6.18}$$

The integrand $\exp(-ik|\mathbf{r}-\mathbf{r}'|)$ is a smooth function, so one can do the integral directly by using a quadrature rule for triangles. One can also reduce it to a line integral, where the accuracy of the quadratures is more controllable. So the problem is to find a function $F(R)$ such that $\nabla_S \cdot [F(R)(\boldsymbol{\rho}-\boldsymbol{\rho}')] = \exp(-ikR)$. Then one needs to solve an ODE:

$$\frac{dF}{dR}\frac{R^2-h^2}{R} + 2F(R) = \exp(-ik_0R). \tag{6.19}$$

A solution to the above equation is $F(R) = \frac{(1+ikR)e^{-ikR}}{k^2(R^2-h^2)}$. So the integrals take a form: $\int_{x_1}^{x_2} \frac{(1+ik_0\sqrt{x^2+a^2})e^{-ik\sqrt{x^2+a^2}}}{k^2(x^2+b^2)}dx$, which can be handled by numeric quadratures.

6.3 Potential based volume integral equations

In all the previous integral equations appearing in this work, the unknown quantities are either field or current [130]. These quantities are not continuous in the normal or tangential component across different media. The potentials, on the other hand, are smoother. It is interesting to see that the potential, although non-physical, can play a central role. The potentials can be divided as a summation of the incident and the scattered potentials:

$$\mathbf{A} = \mathbf{A}^{\mathrm{sc}} + \mathbf{A}^{\mathrm{inc}}, \mathbf{F} = \mathbf{F}^{\mathrm{sc}} + \mathbf{F}^{\mathrm{inc}}. \tag{6.20}$$

Since the scattered potential $\mathbf{A}^{\mathrm{sc}}, \mathbf{F}^{\mathrm{sc}}$ are related to the sources $\mathbf{J}_{\mathrm{eq}}, \mathbf{M}_{\mathrm{eq}}$, the potential-based volume integral equation reads:

$$\begin{aligned}
\mathbf{A} - k^2 \iiint_\Omega \frac{\exp(-ik|\mathbf{r}-\mathbf{r}'|)}{4\pi|\mathbf{r}-\mathbf{r}'|}(\epsilon_r - 1)\left(\mathbf{A} + \frac{\nabla'\nabla' \cdot A}{k^2} - \frac{i}{k}\nabla' \times \mathbf{F}\right) d\mathbf{r}' = \mathbf{A}^{\mathrm{inc}}, \\
\mathbf{F} - k^2 \iiint_\Omega \frac{\exp(-ik|\mathbf{r}-\mathbf{r}'|)}{4\pi|\mathbf{r}-\mathbf{r}'|}(\mu_r - 1)\left(\mathbf{F} + \frac{\nabla'\nabla' \cdot F}{k^2} + \frac{i}{k}\nabla' \times \mathbf{A}\right) d\mathbf{r}' = \mathbf{F}^{\mathrm{inc}}.
\end{aligned} \tag{6.21}$$

The equations (6.22) are quite similar to that in (6.7). They share the same Green function as the kernel. However, there are also noticeable difference. For instance, in Eq. (6.22), the differential operators are inside the integral operators.

Since it is inconvenient to take double differential operator inside the integral, we use the scalar potential $\nabla \cdot \mathbf{A} = k\phi_e, \nabla \cdot \mathbf{F} = k\phi_m$. Moreover, in the absence of magnetic materials, the PVIE is reduced to:

$$\begin{aligned}
&\mathbf{A} - k^2 \iiint_\Omega \frac{\exp(-ik|\mathbf{r}-\mathbf{r}'|)}{4\pi|\mathbf{r}-\mathbf{r}'|}(\epsilon_r - 1)\left(\mathbf{A} + \frac{\nabla'\phi_e}{k}\right) d\mathbf{r}' = \mathbf{A}^{\mathrm{inc}}, \\
&\nabla \cdot \mathbf{A} = k\phi_e.
\end{aligned} \tag{6.22}$$

The quantities $\mathbf{A}, \phi_e$ are continuous across boundaries between different media. Therefore, s-BFs can be used in the discretization. In a tetrahedral mesh, the s-BFs, which have been used in solving the LLGE, are adopted here. The usage of s-BFs have the following advantages: (1) They can reduce the number of unknowns. The number of s-BFs is only $\frac{1}{3}$ times the number of SWG-BFs. (2) The matrices from the s-BF method is smaller than that from the SWG-BFs, making the iterative solution faster. (3) The formulation is free from surface integrals, and it is easy for the implementation of inhomogeneous and anisotropic media.

6.4 Numerical results

In this section, a few examples are presented to validate the proposed method.

6.4.1 Scattering from a layered sphere

A three layered sphere, is composed of three materials, is shown in Fig. 6.2. In this simulation, there were 1.6 million tetrahedrons, 275 thousand vertices. It took a GMRES solver 63 iterations to reach an error of 10^{-3}. The preprocessing time was only 9 seconds, and the total simulation time was 3.8 minutes. We can see the good agreement between the Mie series and the PVIE.

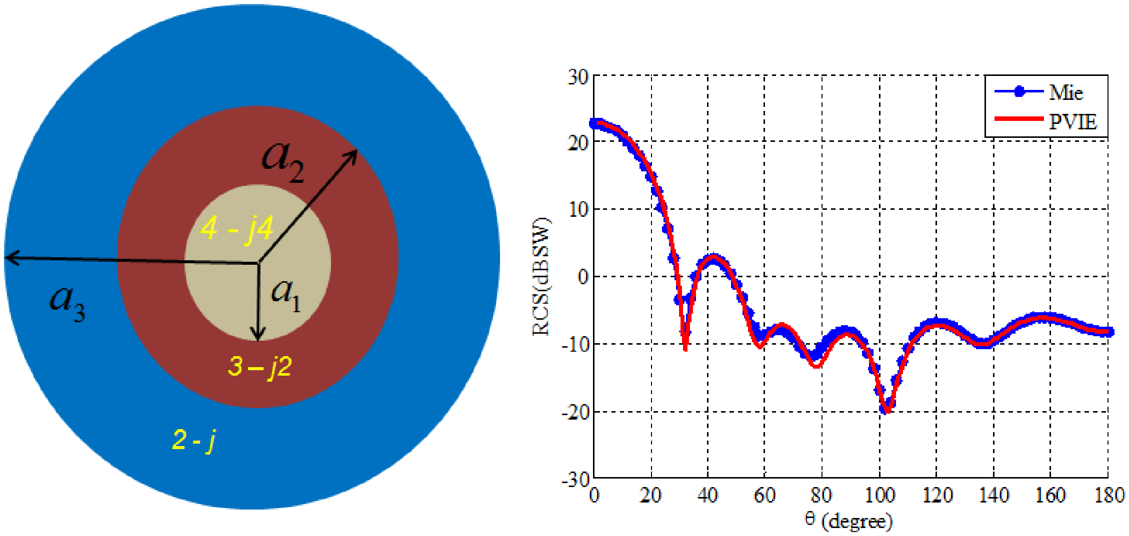

Figure 6.2: Analysis of scattering from a three layered sphere. $a_1 = 0.3\lambda_0, a_2 = 0.7\lambda_0, a_3 = \lambda_0$.

6.4.2 Reflection coefficients of a doubly periodic structure

Periodic structures are used widely in microwave and photonic devices [36, 131, 132, 133]. The integral equations can be used for these structures. In this case, the Green's function is more complex:

$$G_p(\mathbf{r},\mathbf{r}') := \sum_{m=-\infty}^{m=+\infty}\sum_{n=-\infty}^{n=+\infty}\frac{e^{-ik|\mathbf{r}-\mathbf{r}'+m\hat{\mathbf{x}}L_x+n\hat{\mathbf{y}}L_y|}}{4\pi|\mathbf{r}-\mathbf{r}'+m\hat{\mathbf{x}}L_x+n\hat{\mathbf{y}}L_y|}e^{-i(mk_{x0}L_x+nk_{y0}L_y)}, \qquad (6.23)$$

where k_{x0} and k_{y0} are phases shifted in the $x-$ and $y-$ directions. The incident field is $\mathbf{E} = \hat{\mathbf{x}}\exp(-ikx)$. The structure is a cube of 1cm × 1cm × 1cm, and the spacing between the elements is $L_x = L_y = 2.5$cm. The PVIE was applied to calculate the induced equivalent electric current $\mathbf{J}$ inside the element. $\mathbf{J}$ was applied to compute the reflection coefficient. The wavelength is swept, and the reflection coefficient is calculated. Rigorous coupled wave analysis (RCWA) was used as an analytic apparatus to verify the accuracy of PVIE. The PVIE has a good agreement with the RCWA.

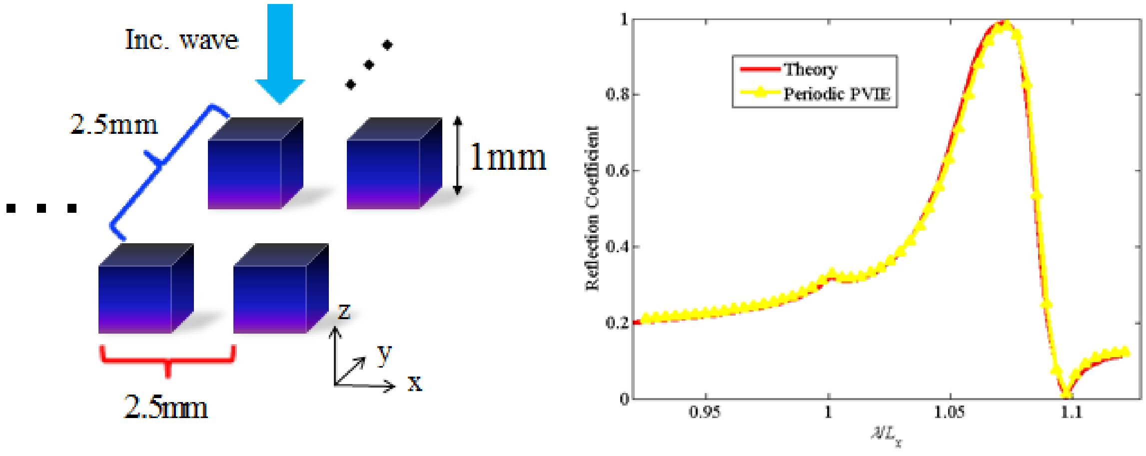

Figure 6.3: Analysis of reflection coefficient from a doubly periodic structure.

Acknowledgements: Chapter 6, in part, is based on the journal article: S. Li, R. Chang, A. Boag, V. Lomakin, "Fast electromagnetic integral equation solvers on graphics processing units," IEEE Antennas Propag. Mag., vol. 54, no. 5, Oct.2012. The dissertation author was the contributing author to this article.

Bibliography

[1] J. Jackson, *Classical electrodynamics.* New York: Wiley, 1999.

[2] L. Landau and E. Lifshitz, *Electrodynamics of continuous media.* Oxford, England: Butterworth-Heinemann, 1995.

[3] T. L. Gilbert, “A phenomenological theory of damping in ferromagnetic materials,” *Magnetics, IEEE Transactions on*, vol. 40, no. 6, pp. 3443–3449, 2004.

[4] D. Pissoort, E. Michielssen, F. Olyslager, and D. D. Zutter, “Fast analysis of 2-D electromagnetic crystal devices using a periodic green function approach,” *IEEE Journal of lightwave technology*, vol. 23, no. 7, p. 2294, 2005.

[5] D. Pissoort, E. Michielssen, and A. Grbic, “An electromagnetic crystal green function multiple scattering technique for arbitrary polarizations, lattices, and defects,” *IEEE Journal of lightwave technology*, vol. 25, no. 2, pp. 571–583, 2007.

[6] A. E. Yilmaz, J.-M. Jin, and E. Michielssen, “A parallel FFT accelerated transient field-circuit simulator,” *IEEE Transactions on Microwave Theory and Techniques*, vol. 53, no. 9, pp. 2851–2865, 2005.

[7] R. Wang and J.-M. Jin, “A symmetric electromagnetic-circuit simulator based on the extended time-domain finite element method,” *IEEE Transactions on Microwave Theory and Techniques*, vol. 56, no. 12, pp. 2875–2884, 2008.

[8] A. Taflove, *Computational Electrodynamics The Finite-Difference Time-Domain Method.* Norwood, MA, USA: Artech House, 1995.

[9] K. Yee, “Numerical solution of initial boundary value problems involving Maxwell’s equations in isotropic media,” *IEEE Transactions on Antennas and Propagation*, vol. 14, no. 3, pp. 302–309, 1966.

[10] A. Taflove, “Application of the finite-difference time-domain method to sinusoidal steady-state electromagnetic-penetration problems,” *IEEE Transactions on Electromagnetic Compatibility*, no. 3, pp. 191–202, 1980.

[11] R. Courant, Friedrichs, and H. K., Lewy, "Über die partiellen differenzengleichungen der mathematischen physik," *Mathematische Annalen*, vol. 100, no. 1, pp. 32–74, 1928.

[12] E. Teixeira, "Time-domain finite-difference and finite-element methods for Maxwell equations in complex media," *IEEE Transactions on Antennas and Propagation*, vol. 56, no. 8, pp. 2150–2166, 2008.

[13] Y. Huang, X. Li, F. Cu, and S.-T. Ho, "Simulation, optimization, and fabrication of optical microresonator based lasers and filters, and coupling to radial or tangential waveguides," *Trends in Nano-and Micro-Cavities*, p. 267, 2011.

[14] X. Li, F. Ou, Y. Huang, and S.-T. Ho, "Micro-resonator loss computation using conformal transformation and active-lasing FDTD approach and applications to tangential/radial output waveguide optimization II: FDTD approach," *Optics Communications*, vol. 291, pp. 447–454, 2013.

[15] S.-T. Ho, K. Ravi, Y. Huang, Q. Wang, B. Bhola, X. Chen, and X. Li, "Spatial temporal simulation of active optoelectronic and plasmonic devices using a multi-level multi-electron FDTD model," in *Advances in Optoelectronics and Micro/Nano-Optics (AOM), 2010 OSA-IEEE-COS*. IEEE, 2010, pp. 1–4.

[16] Z. Hou, X. Li, Y. Huang, and S. Ho, "Physics of elliptical reflectors at large reflection and divergence angles I: Their design for nano-photonic integrated circuits and application to low-loss low-crosstalk waveguide crossing," *Optics Communications*, vol. 287, pp. 96–105, 2013.

[17] X. Zhang, A. Hosseini, H. Subbaraman, S. Wang, Q. Zhan, J. Luo, A. Jen, and R. Chen, "Integrated photonic electromagnetic field sensor based on broadband bowtie antenna coupled silicon organic hybrid modulator," vol. 32, no. 10, pp. 3774 – 3784, 2014.

[18] B. Engquist and A. Majda, "Absorbing boundary conditions for the numerical simulation of waves," *Mathematics of Computation*, vol. 31, pp. 629–651, 1977.

[19] J. Berenger, "A perfectly matched layer for the absorption of electromagnetic waves," *Journal of Computational Physics*, vol. 114, pp. 185–200, 1994.

[20] X. Li, F. Ou, Y. Huang, and S.-T. Ho, "Micro-resonator loss computation using conformal transformation and active-lasing FDTD approach and applications to tangential/radial output waveguide optimization i: Analytical approach," *Optics Communications*, vol. 291, pp. 435–446, 2013.

[21] J. Jin, *The Finite Element Method in Electromagnetics.* John Wiley & Sons, 1993.

[22] K. K. Gupta and J. L. Meek, "A brief history of the beginning of the finite element method," *Internal Journal for Numerical Methods in Engineering*, vol. 39, pp. 3761–3774, 1996.

[23] G. Strang and G. J. Fix, *An analysis of the finite element method.* Englewood Cliffs, NJ: Prentice-Hall, 1973.

[24] K.-J. Bathe and E. L. Wilson, *Numerical methods in finite element analysis.* Englewood Cliffs, NJ: Prentice-Hall, 1976.

[25] R. Graglia, D. Wilton, and A. Peterson, "Higher order interpolatory vector bases for computational electromagnetics," *IEEE Transactions on Antennas and Propagation*, vol. 45, no. 3, pp. 329–342, 1997.

[26] M. Djordjević and B. Notaroš, "Double higher order method of moments for surface integral equation modeling of metallic and dielectric antennas and scatterers," *IEEE Transactions on Antennas and Propagation*, vol. 52, no. 8, pp. 2118–2129, 2004.

[27] E. Jørgensen, J. Volakis, P. Meincke, and O. Breinbjerg, "Higher order hierarchical legendre basis functions for electromagnetic modeling," *IEEE Transactions on Antennas and Propagation*, vol. 52, no. 11, pp. 2985–2995, 2004.

[28] J. Nédélec, "A new family of mixed finite elements in $\mathbb{R}^3$," *Numerische Mathematik*, vol. 50, pp. 57–81, 1986.

[29] X. Li, F. Ou, Z. Hou, Y. Huang, and S.-T. Ho, "Experimental demonstration and simulation of lossless metal-free integrated elliptical reflectors for waveguide turnings and crossings," in *CLEO: Applications and Technology*, 2011, p. JTuI26.

[30] X. Li, F. Ou, Y. Huang, and S.-T. Ho, "Extraction of light from microdisk lasers by radial direction coupling waveguide," in *Frontiers in Optics*, 2010, p. FThQ8.

[31] P. Silvester, "Curvilinear finite elements for two-dimensional saturable magnetic fields," *IEEE Transactions on Power Apparatus and Systems*, vol. 93, no. 11, pp. 1861–1870, 1974.

[32] B. Notaroš, "Higher order frequency-domain computational electromagnetics," *IEEE Transactions on Antennas and Propagation*, vol. 56, no. 8, pp. 2251–2276, 2008.

[33] Z.-Q. Lü, X. An, and W. Hong, "A fast domain decomposition method for solving three-dimensional large-scale electromagnetic problems," *IEEE Transactions on Antennas and Propagation*, vol. 56, no. 8, pp. 2200–2210, 2008.

[34] G. Hsiao and W. Wendland, *Boundary Integral Equations.* Springer, 2008.

[35] R. Kress, *Linear Integral Equations.* Springer, 2014.

[36] D. Van Orden and V. Lomakin, "Rapidly convergent representations for 2D and 3D greens functions for a linear periodic array of dipole sources," *IEEE Transactions on Antennas and Propagation*, vol. 57, no. 7, pp. 1973–1984, 2009.

[37] J. Aronsson, K. Butt, I. Jeffrey, and V. I. Okhmatovski, "The Barnes-Hut hierarchical center-of-charge approximation for fast capacitance extraction in multilayered media," *IEEE Transactions on Microwave Theory and Techniques*, vol. 58, no. 5, pp. 1175–1188, 2010.

[38] K. Yang and A. E. Yilmaz, "A three-dimensional adaptive integral method for scattering from structures embedded in layered media," *IEEE Transactions on Geoscience and Remote Sensing*, vol. 50, no. 4, pp. 1130–1139, 2012.

[39] S. Rao, D. Wilton, and G. Glisson, "Electromagnetic scattering by surfaces of arbitrary shape," *IEEE Transactions on Antennas and Propagation*, vol. 30, no. 3, pp. 409–418, 1982.

[40] L. Greengard and V. Rokhlin, "A fast algorithm for particle simulations," *Journal of Computational Physics*, vol. 135, pp. 280–292, 1997.

[41] S. Li, B. Livshitz, and V. Lomakin, "Fast evaluation of helmholtz potential on graphics processing units (GPUs)," *Journal of Computational Physics*, vol. 229, pp. 8430–8444, 2010.

[42] A. E. Yilmaz, J.-M. Jin, and E. Michielssen, "Time domain adaptive integral method for surface integral equations," *IEEE Transactions on Antennas and Propagation*, vol. 52, no. 10, pp. 2692–2708, 2004.

[43] A. E. Yilmaz and F. Wei, "A more scalable and efficient parallelization of the adaptive integral method part i: algorithm," *IEEE Transactions on Antennas and Propagation*, vol. 62, no. 2, pp. 714–726, 2014.

[44] N. Morita, *Integral equation methods for electromagnetics.* Boston, MA, USA: Artech House, 1990.

[45] Y. Saad, *Iterative methods for sparse linear systems.* Philadelphia, PA: Society for Industrial and Applied Mathematics, 2003.

[46] Y. Saad and M. Schultz, "GMRES: a generalized minimal residual algorithm for solving nonsymmetric linear systems," *SIAM Journal on Scientific and Statistical Computing*, vol. 7, no. 3, pp. 856–869, 1986.

[47] R. Freund, "A transpose-free quasi-minimal residual algorithm for non-hermitian linear systems," *SIAM Journal on Scientific Computing*, vol. 14, no. 2, pp. 470–482, 1993.

[48] H. van der Vorst, "Bi-CGSTAB: A fast and smoothly converging variant of Bi-CG for the solution of nonsymmetric linear systems," *SIAM Journal on Scientific and Statistical Computing*, vol. 13, no. 2, pp. 631–644, 1992.

[49] X. Nie, L. Li, N. Yuan, T. Yeo, and Y. Gan, "Precorrected-FFT solution of the volume integral equation for 3-D inhomogeneous dielectric objects," *IEEE Transactions on Antennas and Propagation*, vol. 53, no. 1, pp. 313–320, 2005.

[50] R. Chang, S. Li, M. Lubarda, B. Livshitz, and V. Lomakin, "Fastmag: Fast micromagnetic simulator for complex magnetic structures (invited)," *Journal of Applied Physics*, vol. 109, no. 7, pp. 8979–8985, 2011.

[51] W. Ewe, L. Li, and M. Leong, "Fast solution of mixed dielectric/conducting scattering problem using volume-surface adaptive integral method," *IEEE Transactions on Antennas and Propagation*, vol. 52, no. 11, pp. 3071–3077, 2004.

[52] A. Polimeridis and J. Mosig, "Evaluation of weakly singular integrals via generalized cartesian product rules based on the double exponential formula," *IEEE Transactions on Antennas and Propagation*, vol. 58, no. 6, pp. 1980–1988, 2010.

[53] A. Polimeridis and T. Yioultsis, "On the direct evaluation of weakly singular integrals in galerkin mixed potential integral equation formulations," *IEEE Transactions on Antennas and Propagation*, vol. 56, no. 9, pp. 3011–3019, 2008.

[54] M. Khayat and D. Wilton, "Numerical evaluation of singular and near-singular potential integrals," *IEEE Transactions on Antennas and Propagation*, vol. 53, no. 10, pp. 3180–3190, 2005.

[55] V. Lomakin, B. Livshitz, and H. Bertram, "Magnetization reversal in patterned media," *IEEE Transactions on Magnetics*, vol. 43, no. 6, pp. 2154–2156, 2007.

[56] O. Bottauscio, M. Chiampi, and A. Manzin, "A finite element procedure for dynamic micromagnetic computations," *IEEE Transactions on Magnetics*, vol. 44, no. 11, pp. 3149–3153, 2008.

[57] T. Koehler and D. Fredkin, "Hybrid method for computing demagnetizing fields," *IEEE Transactions on Magnetics*, vol. 26, no. 2, pp. 415–417, 1990.

[58] ——, "Finite element methods for micromagnetics," *IEEE Transactions on Magnetics*, vol. 28, no. 2, pp. 1239–1244, 1992.

[59] W. Chen, T. Koehler, and D. Fredkin, "A new finite element method in micromagnetics," *IEEE Transactions on Magnetics*, vol. 29, no. 3, pp. 2124–2128, 1993.

[60] B. Yang and D. Fredkin, "Dynamical micromagnetics by the finite element method," *IEEE Transactions on Magnetics*, vol. 34, no. 6, pp. 3842–3852, 1998.

[61] M. Reis, *Fundamentals of magnetism.* Amsterdam: Academic Press, 2013.

[62] M. Getzlaff, *Fundamentals of magnetism.* New York: Springer, 2008.

[63] J. Coey, *Magnetism and magnetic materials.* Cambridge: Cambridge University Press, 2010.

[64] F. Mabbs, *Magnetism and transition metal complexes.* Mineola, NY: Dover Publications, 2008.

[65] M. A. Ruderman and C. Kittel, "Indirect exchange coupling of nuclear magnetic moments by conduction electrons," *Physical Review*, vol. 96, no. 1, p. 99, 1954.

[66] D. Ralph and M. Stiles, "Spin transfer torques," *Journal of Magnetism and Magnetic Materials*, vol. 320, pp. 1190–1216, 2008.

[67] X. Wang, C. Garciá-Cervera, and E. Weinan, "A Gauss-Seidel projection method for micromagnetics simulations," *Journal of Computational Physics*, vol. 171, pp. 357–372, 2001.

[68] O. Bottauscio, M. Chiampi, and A. Manzin, "Multiscale finite element solution of the exchange term in micromagnetic analysis of large bodies," *IEEE Transactions on Magnetics*, vol. 45, no. 11, pp. 5200–5203, 2009.

[69] B. Van de Wiele, A. Manzin, L. Dupré, F. Olyslager, O. Bottauscio, and M. Chiampi, "Multiscale finite element solution of the exchange term in micromagnetic analysis of large bodies," *IEEE Transactions on Magnetics*, vol. 45, no. 3, pp. 1614–1617, 2009.

[70] M. dAquino, C. Serpico, and G. Miano, “Geometrical integration of Landau-Lifshitz-Gilbert equation based on the midpoint rule,” *Journal of Computational Physics*, vol. 209, pp. 730–753, 2005.

[71] J. Fidler and T. Schrefl, “Micromagnetic modelling-the current state of the art,” *Journal of Physics D: Applied Physics*, vol. 33, no. 15, p. R135, 2000.

[72] D. Dunavant, “High degree efficient symmetrical gaussian quadrature rules for the triangle,” *International Journal for Numerical Methods in Engineering*, vol. 21, pp. 1129–1148, 1985.

[73] M. Gellert and R. Harbord, “Moderate degree cubature formulas for 3-D tetrahedral finite element approximations,” *Communications in Applied Numerical Methods*, vol. 7, pp. 487–495, 1991.

[74] W. Scholz, J. Fidler, T. Schrefl, D. Suess, R. Dittrich, H. Forster, and V. T-siantos, “Scalable parallel micromagnetic solvers for magnetic nanostructures,” *Computational Materials Science*, vol. 28, no. 2, pp. 366–383, 2003.

[75] M. Li and W. Chew, “Applying divergence-free condition in solving the volume integral equation,” *Progress In Electromagnetics Research*, vol. 57, pp. 311–333, 2006.

[76] S. Li, B. Livshitz, and V. Lomakin, “Graphics processing unit accelerated $\mathcal{O}(n)$ micromagnetic solver,” *IEEE Transactions on Magnetics*, vol. 46, no. 6, pp. 2373–2375, 2010.

[77] N. A. Gumerov and R. Duraiswami, “Fast multipole methods on graphics processors,” *Journal of Computational Physics*, vol. 227, no. 18, pp. 8290–8313, 2008.

[78] X. Sheng, J.-M. Jin, J. Song, W. C. Chew, and C.-C. Lu, “Solution of combined-field integral equation using multilevel fast multipole algorithm for scattering by homogeneous bodies,” *IEEE Transactions on Antennas and Propagation*, vol. 46, no. 11, pp. 1718–1726, 1998.

[79] B. Streibl, T. Schrefl, and J. Fidler, “Dynamic fe simulation of μmag standard problem no. 2,” *Journal of applied physics*, vol. 85, no. 8, pp. 5819–5821, 1999.

[80] M. Escobar, M. V. Lubarda, S. Li, R. Chang, B. Livshitz, and V. Lomakin, “Advanced micromagnetic analysis of write head dynamics using fastmag,” *IEEE Transactions on Magnetics*, vol. 48, no. 5, pp. 1731–1737, 2012.

[81] A. Jeffrey and D. Zwillinger, *Table of integrals, series, and products.* Academic Press, 2007.

[82] D. Knoll and D. Keyes, "Jacobian-free Newton-Krylov methods: a survey of approaches and applications," *Journal of Computational Physics*, vol. 193, pp. 357–397, 2004.

[83] G. Henkelman, B. Uberuaga, and Jónsson, "A climbing image nudged elastic band method for finding saddle points and minimum energy paths," *Journal of Chemical Physics*, vol. 113, no. 22, pp. 9901–9904, 2000.

[84] S. Zhang and Z. Li, "Roles of nonequilibrium conduction electrons on the magnetization dynamics of ferromagnets," *Physical Review Letters*, vol. 93, no. 12, p. 127204, 2004.

[85] W. Chew, M. Tong, and B. Hu, *Integral Equation Methods for Electromagnetic and Elastic Waves.* USA: Morgan & Claypool, 2009.

[86] R. Chang and V. Lomakin, "Quadrilateral barycentric basis functions for surface integral equations," *IEEE Transactions on Antennas and Propagation*, vol. 61, no. 12, pp. 6039–6050, 2013.

[87] A. Peterson, S. Ray, and R. Mittra, *Computational Methods for Electromagnetics.* IEEE Press, 1998.

[88] R. Mittra, *Computational electromagnetics : recent advances and engineering applications.* New York: Springer, 2013.

[89] X. Sheng and W. Song, *Essentials of computational electromagnetics.* Singapore: John Wiley & Sons, 2012.

[90] T. Rylander, P. Ingelström, and A. Bondeson, *Computational Electromagnetics.* New York: Springer, 2013.

[91] G. Hsiao and R. Kleinman, "Mathematical foundations for error estimation in numerical solutions of integral equations in electromagnetics," *IEEE Transactions on Antennas and Propagation*, vol. 45, no. 3, pp. 316–328, 1997.

[92] A. Bourdonnaye, "Some formulations coupling finite element and integral equation methods for Helmholtz equation and electromagnetism," *Journal Numerische Mathematik*, vol. 69, no. 3, pp. 257–268, 1995.

[93] H. Contopanagos, B. Dembart, M. Epton, J. Ottusch, V. Rokhlin, J. Visher, and S. Wandzura, "Well-conditioned boundary integral equations for three-dimensional electromagnetic scattering," *IEEE Transactions on Antennas and Propagation*, vol. 50, no. 12, pp. 1824–1830, 2002.

[94] S. Borel, D. Levadoux, and F. Alouges, "A new well-conditioned integral formulation for Maxwell equations in three dimensions," *IEEE Transactions on Antennas and Propagation*, vol. 53, no. 9, pp. 2995–3004, 2005.

[95] F. Andriulli, K. Cools, H. Băgci, F. Olyslager, A. Buffa, S. Christiansen, and E. Michielssen, “A multiplicative Calderón preconditioner for the electric field integral equation,” *IEEE Transactions on Antennas and Propagation*, vol. 56, no. 8, pp. 2398–2412, 2008.

[96] A. Pressley, *Elementary Differential Geometry.* Springer, 2012.

[97] J. Song and W. Chew, “Moment method solutions using parametric geometry,” *Journal of Electromagnetic Waves and Applications*, vol. 9, no. 8, pp. 71–83, 1995.

[98] J. Rius, E. Úbeda, and J. Parrón, “On the testing of the magnetic field integral equation with RWG basis functions in method of moments,” *IEEE Transactions on Antennas and Propagation*, vol. 49, no. 11, pp. 1550–1553, 2001.

[99] K. Cools, F. Andriulli, F. Olyslager, and E. Michielssen, “Nullspaces of MFIE and Calderón preconditioned EFIE operators applied to toroidal surfaces,” *IEEE Transactions on Antennas and Propagation*, vol. 57, no. 10, pp. 3205–3215, 2009.

[100] O. Ergül and L. Gürel, “The use of curl-conforming basis functions for the magnetic-field integral equation,” *IEEE Transactions on Antennas and Propagation*, vol. 54, no. 7, pp. 1917–1926, 2006.

[101] S. Yan, J. Jin, and Z. Nie, “Improving the accuracy of the second kind fredholm integral equations by using the Buffa-Christiansen functions,” *IEEE Transactions on Antennas and Propagation*, vol. 59, no. 4, pp. 1299–1310, 2011.

[102] M. Tong, W. Chew, B. Rubin, J. Morsey, and L. Jiang, “On the dual basis for solving electromagnetic surface integral equations,” *IEEE Transactions on Antennas and Propagation*, vol. 57, no. 10, pp. 3136–3146, 2009.

[103] M. Tong, “Efficient electromagnetic analysis for interconnect and packaging structures using dual basis function in the method of moments,” *IEEE Transactoins on Components, Packaging and Manufacturing Technology*, vol. 1, no. 7, pp. 1089–1097, 2011.

[104] P. Ylä-Oijala, S. Kiminki, F. Andriulli, and S. Järvenpää, “Stable discretization of combined source integral equation for scattering by dielectric objects,” *IEEE Transactions on Antennas and Propagation*, vol. 60, no. 5, pp. 2575–2578, 2012.

[105] Q. Chen and D. Wilton, "Electromagnetic scattering by three-dimensional arbitrary complex material/conducting bodies," in *Antennas and Propagation Society International Symposium, 1990. AP-S. Merging Technologies for the 90's. Digest.*, 1990, pp. 590–593.

[106] S. Christiansen and J. Nédélec, "A preconditioner for the electric field integral equation based on Calderón formulas," *IEEE Transactions on Antennas and Propagation*, vol. 40, no. 3, pp. 1100–1135, 2002.

[107] F. Andriulli, K. Cools, I. Bogaert, and E. Michielssen, "On a well-conditioned electric field integral operator for multiply connected geometries," *IEEE Transactions on Antennas and Propagation*, vol. 61, no. 4, pp. 2077–2087, 2013.

[108] M. Stephanson and J. Lee, "Preconditioned electric field integral equation using Calderón identities and dual loop/star basis functions," *IEEE Transactions on Antennas and Propagation*, vol. 57, no. 4, pp. 1274–1279, 2009.

[109] F. Valdés, F. Andriulli, K. Cools, and E. Michielssen, "High-order div- and quasi curl-conforming basis functions for calderón multiplicative preconditioning of the EFIE," *IEEE Transactions on Antennas and Propagation*, vol. 59, no. 4, pp. 1321–1337, 2011.

[110] K. Cools, F. Andriulli, D. Zutter, and E. Michielssen, "Accurate and conforming mixed discretization of the MFIE," *IEEE Antennas Wireless Propagation Letters*, vol. 10, pp. 528–531, 2011.

[111] S. Yan, J. Jin, and Z. Nie, "Accuracy improvement of the second-kind integral equations for generally shaped objects," *IEEE Transactions on Antennas and Propagation*, vol. 61, no. 2, pp. 788–797, 2013.

[112] P. Ylä-Oijala, S. Kiminki, K. Cools, F. Andriulli, and S. Järvenpää, "Mixed discretization schemes for electromagnetic surface integral equations," *International Journal of Numeric Modelling: Electronic Networks, Devices and Fields*, vol. 25, no. 5-6, pp. 525–540, 2012.

[113] Y. Su, J. Jin, and Z. Nie, "EFIE analysis of low-frequency problems with loop-star decomposition and Calderón multiplicative preconditioner," *IEEE Transactions on Antennas and Propagation*, vol. 58, no. 3, pp. 857–867, 2010.

[114] J. Zhao and W. Chew, "Integral equation solution of Maxwell's equations from zero frequency to microwave frequencies," *IEEE Transactions on Antennas and Propagation*, vol. 48, no. 10, pp. 1635–1645, 2000.

[115] F. Andriulli, "Loop-star and loop-tree decompositions: Analysis and efficient algorithms," *IEEE Transactions on Antennas and Propagation*, vol. 60, no. 5, pp. 2347–2356, 2012.

[116] J. Lee, R. Lee, and R. Burkholder, “Loop star basis functions and a robust preconditioner for EFIE scattering problems,” *IEEE Transactions on Antennas and Propagation*, vol. 51, no. 8, pp. 1855–1863, 2003.

[117] F. Andriulli, K. Cools, I. Bogaert, and E. Michielssen, “On a well-conditioned electric field integral operator for multiply connected geometries,” *IEEE Transactions on Antennas and Propagation*, vol. 61, no. 4, pp. 2077–2087, 2013.

[118] F. Andriulli, A. Tabacco, and G. Vecchi, “Solving the EFIE at low-frequencies with a conditioning that grows only logarithmically with the number of unknowns,” *IEEE Transactions on Antennas and Propagation*, vol. 58, no. 5, pp. 1614–1624, 2010.

[119] A. Winslow, “Numerical solution of the quasilinear Poisson equation in a nonuniform triangle mesh,” *Journal of Computational Physics*, vol. 1, no. 2, pp. 149–172, 1967.

[120] A. Bossavot, “How weak is the “weak solution” in finite element methods?” *IEEE Transactions on Magnetics*, vol. 34, no. 5, pp. 2429–2432, 1998.

[121] S. Li, R. Chang, A. Boag, and V. Lomakin, “Fast electromagnetic integral-equation solvers on graphics processing units,” *IEEE Transactions on Antennas and Propagation*, vol. 54, no. 5, pp. 71–87, 2012.

[122] F. Wei and A. Yilmaz, “A more scalable and efficient parallelization of the adaptive integral methodpart i: Algorithm,” *IEEE Transactions on Antennas and Propagation*, vol. 62, no. 2, pp. 714–726, 2014.

[123] W. Ewe, E. Li, H. Chu, and L. Li, “Aim analysis of electromagnetic scattering by arbitrarily shaped magnetodielectric object,” *IEEE Transactions on Antennas and Propagation*, vol. 55, no. 7, pp. 2073–2079, 2007.

[124] D. Schaubert, D. Wilton, and A. Glisson, “A tetrahedral modeling method for electromagnetic scattering by arbitrarily shaped inhomogeneous dielectric bodie,” *IEEE Transactions on Antennas and Propagation*, vol. 32, no. 1, pp. 77–85, 1984.

[125] D. Wilton, S. Rao, A. Glisson, and D. Schaubert, “Potential integrals for uniform and linear source distributions on polygonal and polyhedral domains,” *IEEE Transactions on Antennas and Propagation*, vol. 32, no. 3, pp. 276–281, 1984.

[126] D. Ding, R. Chen, Z. Fan, and P. Rui, “A novel hierarchical two-level spectral preconditioning technique for electromagnetic wave scattering,” *IEEE Transactions on Antennas and Propagation*, vol. 56, no. 4, pp. 1122–1132, 2004.

[127] S. Balasubramanian, S. Lalgudi, and B. Shanker, “Fast-integral-equation scheme for computing magnetostatic fields in nonlinear media,” *IEEE Transactions on Magnetics*, vol. 38, no. 5, pp. 3426–3432, 2002.

[128] E. Klopf, N. Šekeljić, M. Ilić, and B. Notaroš, “Optimal modeling parameters for higher order MoM-SIE and FEM-MoM electromagnetic simulations,” *IEEE Transactions on Antennas and Propagation*, vol. 60, no. 6, pp. 2790–2811, 2012.

[129] R. Graglia, “On the numerical integration of the linear shape functions times the 3-d green’s function or its gradient on a plane triangle,” *Antennas and Propagation, IEEE Transactions on*, vol. 41, no. 10, pp. 1448–1455, 1993.

[130] P. De Doncker, “A potential integral equations method for electromagnetic scattering by penetrable bodies,” *IEEE Transactions on Antennas and Propagation*, vol. 49, no. 7, pp. 1037–1042, 2001.

[131] D. Van Orden and V. Lomakin, “Rapidly convergent representations for periodic greens functions of a linear array in layered media,” *IEEE Transactions on Antennas and Propagation*, vol. 60, no. 2, pp. 870–879, 2012.

[132] S. Li, D. Van Orden, and V. Lomakin, “Fast periodic interpolation method for periodic unit cell problems,” *IEEE Transactions on Antennas and Propagation*, vol. 58, no. 12, pp. 4005–4014, 2010.

[133] A. Fructos, R. Boix, and F. Mesa, “Application of Kummer’s transformation to the efficient computation of the 3-D Greens function with 1-D periodicity,” *IEEE Transactions on Antennas and Propagation*, vol. 58, no. 1, pp. 95–116, 2010.